

# Thèse de Doctorat

présentée par

**György Hantal**

pour obtenir le grade de  
Docteur de l'Université de Franche-Comté en Physique  
et celui de  
Docteur de l'Université Eötvös Loránd de Budapest en Sciences Chimiques

Modélisation de l'adsorption sur des  
particules solides dans l'atmosphère

Thèse en co-tutelle internationale dirigée par  
Sylvain Picaud et Pál Jedlovszky

soutenue le 26 novembre 2010

## Jury :

Président :	Ernö Keszei	Professeur - ELTE University of Budapest
Rapporteurs :	Roland J.-M. Pellenq	Directeur de Recherche CNRS - Marseille et Professeur au MIT, Cambridge, US
Examineurs :	Gergely Tóth	Associate Professor - ELTE University of Budapest
	Daniel Ferry	HDR - Chargé de recherche CNRS, Marseille,
	Jean-Claude Rayez	Professeur Emérite - Université de Bordeaux 1
	Sylvain Picaud	Directeur de Recherche CNRS, Besançon
	Pál Jedlovszky	Professeur - ELTE University of Budapest
	Imre Salma	Professeur - ELTE University of Budapest



# Modelling of adsorption on atmospheric solid particles

PhD Thesis

György Hantal

Supervisors:

Dr Pál Jedlovszky, PhD, DSc

and

Dr Sylvain Picaud, PhD, HDR

Chemistry Doctoral School (Head: Prof. György Inzelt)  
Theoretical and Physical Chemistry, Structural Chemistry  
Doctoral Programme (Head: Prof. Péter Surján)  
Institute of Chemistry, Eötvös Loránd University  
Faculty of Science

Louis Pasteur Doctoral School (Head: Prof. Mironel Enescu)  
Institute UTINAM, University of Franche-Comté  
UFR Sciences et Techniques

Budapest (Hungary) – Besançon (France)

2010



# Modélisation de l'adsorption sur des particules solides dans l'atmosphère

Thèse

György Hantal

Directeurs de thèse :

Dr Sylvain Picaud, PhD, HDR

et

Dr Pál Jedlovszky, PhD, DSc

École doctorale Louis Pasteur (Directeur : Prof. Mironel  
Enescu)

Institut UTINAM, Université de Franche-Comté  
UFR Sciences et Techniques

École doctorale de chimie (Directeur : Prof. György Inzelt)  
Programme doctoral de chimie théorique, physico-chimie et  
chimie structurale (Directeur : Prof. Péter Surján)

Institut de chimie, Université Eötvös Loránd  
Faculté des sciences

Besançon (France) – Budapest (Hongrie)

2010



# Acknowledgements

First of all, I thank my supervisors, Pál Jedlovszky and Sylvain Picaud (listed in alphabetical order) for teaching me and their professional and personal guidance that has been indispensable in carrying out my research. I thank them for letting me work more or less individually thus offering a large scope for my conception and ideas. I am thankful to them also for the friendly and warm ambience we have been working in.

I owe my deepest gratitude to Jean-Claude Rayez for helping and teaching me almost as a third supervisor.

I am particularly grateful to Paul Hoang for his helpful pieces of advice and for his initial efforts without which my PhD studies would not have been possible.

Special thanks to Lívía Bartók-Pártay for encouragements and inspiring discussions in the beginning of my PhD studies.

Carl Williams is also greatly acknowledged whose comments, as a native reader, have been essential in eliminating the most of the grammatical errors.

I am thankful to the French Government for the financial support of my shared PhD studies.

I would also like to thank Dóri for her patience and the unflagging and tender support.

And last but not least I thank everybody not mentioned above who supported me in any respect during the completion of my thesis from the initial to the final level.

# Contents

<b>1</b>	<b>Introduction</b>	<b>1</b>
<b>2</b>	<b>Atmospheric aspects of my work</b>	<b>3</b>
2.1	The OH radical . . . . .	5
2.2	VOCs in the atmosphere . . . . .	8
2.2.1	Formic acid, acetone and benzaldehyde . . . . .	10
2.3	PAH molecules in the atmosphere . . . . .	11
2.4	Solid particles in the atmosphere . . . . .	12
2.4.1	Ice particles . . . . .	12
2.4.2	Atmospheric aerosols and soot particles . . . . .	13
<b>3</b>	<b>Computational methods</b>	<b>17</b>
3.1	Computer simulation methods . . . . .	17
3.1.1	Monte Carlo method . . . . .	19
3.1.1.1	Grand canonical Monte Carlo method . . . . .	21
3.1.2	Molecular dynamics . . . . .	24
3.1.3	Potential models used . . . . .	25
3.1.3.1	Non-reactive potentials . . . . .	26
3.1.3.2	Reactive potentials . . . . .	28
3.1.4	Technical details of simulations . . . . .	32
3.2	Electronic structure calculations . . . . .	34
3.2.1	The AM1 semi-empirical method . . . . .	36

<b>4</b>	<b>Adsorption of VOCs on ice</b>	<b>40</b>
4.1	Introduction . . . . .	40
4.1.1	Common points in the numerical studies . . . . .	41
4.1.1.1	Common computational details . . . . .	41
4.1.1.2	Adsorption isotherms . . . . .	42
4.1.1.3	Density profiles . . . . .	44
4.1.1.4	Interaction energy distribution . . . . .	44
4.1.1.5	Orientational analysis . . . . .	44
4.2	Adsorption of acetone . . . . .	44
4.2.1	Computational details of the simulations . . . . .	45
4.2.2	Results . . . . .	46
4.2.2.1	Adsorption isotherm . . . . .	46
4.2.2.2	Characterisation of the adsorption layers . . . . .	49
4.3	Adsorption of formic acid . . . . .	59
4.3.1	Computational details of the simulations . . . . .	59
4.3.2	Results . . . . .	60
4.3.2.1	Adsorption isotherm . . . . .	60
4.3.2.2	Characterisation of the adsorption layers . . . . .	65
4.4	Adsorption of benzaldehyde . . . . .	72
4.4.1	Computational details of the simulations . . . . .	72
4.4.2	Results . . . . .	72
4.4.2.1	Adsorption isotherm . . . . .	72
4.4.2.2	Characterisation of the adsorption layers . . . . .	74
4.5	Conclusions . . . . .	81
<b>5</b>	<b>Water adsorption on soot</b>	<b>83</b>
5.1	Introduction . . . . .	83
5.2	Computational details . . . . .	84
5.2.1	Soot models . . . . .	84
5.2.2	Grand canonical Monte Carlo simulations . . . . .	87

5.3	Results . . . . .	89
5.3.1	Adsorption isotherms . . . . .	89
5.3.2	Position of the first adsorbed molecules . . . . .	91
5.3.3	Analysis of the pore morphology . . . . .	93
5.3.4	Energetics of the adsorption . . . . .	97
5.4	Conclusions . . . . .	101
<b>6</b>	<b>Reactivity of soot particles</b>	<b>103</b>
6.1	Introduction . . . . .	103
6.2	The SE-D method . . . . .	105
6.3	The elements of our new method . . . . .	108
6.3.1	Kinetic model . . . . .	108
6.3.2	Statistical model . . . . .	110
6.4	Results . . . . .	113
6.5	Conclusions . . . . .	118
<b>7</b>	<b>Conclusions and perspectives</b>	<b>120</b>
	<b>Appendices</b>	<b>124</b>
	Appendix A	
	Biased grand canonical MC techniques . . . . .	124
	Appendix B	
	Long-range corrections used in computer simulations . . . . .	126
	Appendix C	
	Equations of state in describing phase coexistence . . . . .	130
	<b>Bibliography</b>	<b>132</b>

# Chapter 1

## Introduction

During the last decades growing attention has been paid to the atmosphere and atmospheric science. In the early '70s work of Molina, Rowland, Crutzen and many others drew people's attention to environment related problems. They pointed out that human activities can have disastrous consequences on the growth of the ozone hole, and therefore on our environment. It was evidenced that a change in the human attitude to the Earth is inevitable to maintain the balance of the biosphere. The first great success of the endeavours for the protection of the atmosphere was the approval of the Montreal Protocol, which was the first international environmental treaty that banned the production of industrial chemicals reducing the ozone layer. In 1995 it was the first time the Nobel Committee recognised research into man-made impacts on the environment: The Nobel Prize of Crutzen, Molina and Rowland in chemistry showed clearly that atmospheric science should have accentuated importance in the 21st century.

Atmospheric chemistry is mainly an experimental science that generally aims at understanding the basic mechanisms in the atmosphere. Atmospheric processes, however, are difficult to study experimentally. Our possibilities are quite limited because the experiments should be performed under *controlled* atmospheric conditions and the measurement of different chemical species should be carried out at the same time. Theoretical methods and particularly simulation techniques can complement and support our experimental understanding. Numerical methods have already been used successfully in numerous cases to reduce extremely complicated reaction mechanisms by finding the key processes and species. Theoretical methods enable us to create models by identifying the major features and elements of the process studied. Successful predictions made by the model can support its validity. With computer simulation techniques one can go farther because it is possible to make experiments

on the theoretical model that can reveal a lot of details that are hidden from the experimentalists. Atomistic simulations allow one to observe the microscopic details of the process studied and, which is at least as much or more important, make it possible to compute ensemble averages on the model system without any approximation. The fact that many of the largest supercomputers in the world are dedicated to atomistic simulations in connection with drug development and protein research is a proof of the strategic importance of this area.

In my work, I used theoretical methods to study phenomena related to two of the most abundant atmospheric solid particles, namely ice and soot. Ice particles can have two main impacts on atmospheric chemistry: A direct effect arises by providing an enormous surface for heterogeneous reactions. An indirect effect comes from the modification of the composition of the atmosphere by adsorbing molecules from the gas phase. These molecules can then get directly to the Earth by precipitation. The effects of soot particles are similar to those of ice but soot has presumably a much more enhanced chemical activity depending on its size, shape and composition. Moreover, specific radiative properties can be attributed to these particles thus affecting the Earth's albedo and therefore the warming of its surface.

A microscopic approach is desirable to the profound understanding of the effects of these two kinds of solid particles. My research was dedicated to three main topics in connection with soot and ice. The first topic concerns the adsorption of three different volatile organic compounds (VOCs), such as acetone, formic acid and benzaldehyde on the ice surface. The VOC molecules are released into the atmosphere mainly from anthropogenic sources, and are suspected to have a significant role in the chemistry of the atmosphere either through the products of their photo-degradation, or by the production of contaminant and harmful tropospheric ozone. My second research topic concentrates on the water uptake at the soot surface. Soot particles emitted in particular by aircrafts have an undeniable role in the nucleation of ice particles in the oversaturated atmosphere. However, the mechanism of the nucleation and the key factors in this procedure are not known. My third subject deals with the chemical activity of soot particles. I investigate how the soot surface influences the oxidation of polycyclic aromatic hydrocarbons (PAHs) by the OH radical which is the most abundant oxidising agent in the atmosphere.

My thesis is organised as follows. The next chapter reviews the atmospheric aspects and backgrounds of my work. In Chapter 3 the theoretical methods used are outlined. Chapter 4, 5 and 6 give my results on the adsorption of VOCs on ice, the water uptake on soot particles, and the reactivity of soot, respectively. Before the bibliography, the main conclusions and perspectives are summarised.

## Chapter 2

# Atmospheric aspects of my work

The interesting regions of the atmosphere from a chemical point of view are the troposphere and the stratosphere: The first and second region above the Earth, respectively[1, 2, 3]. These two regions account for 99% of the total atmospheric mass, within which 85% is located in the troposphere. Indeed, pressure diminishes roughly exponentially going farther from the surface of Earth according to the well-known barometric law:

$$p(z) = p(0) \exp\left(\frac{-M_a g z}{RT}\right),$$

where  $p(z)$  is the pressure at altitude  $z$ ,  $p(0)$  is the pressure at  $z = 0$  (i.e. the ground level),  $M_a$  is the molar mass of air,  $g$  is the gravitational acceleration,  $R$  is the ideal gas constant and  $T$  is the absolute temperature. However, this expression can be considered as valid only in relatively narrow ranges. If the temperature variation is large in the studied region, an average temperature value might be used to get reasonable estimates for the pressure change. Figure 2.1[2] illustrates the variation of pressure and temperature in function of altitude.

Earth's surface is warmed by absorbing solar radiation mainly in the infrared (IR) range. The warm surface heats the lower region of the troposphere by convection. Above the surface, the temperature decreases nearly linearly by increasing altitude. The tendency changes at the altitude of about 15 km. This region is the boundary of the stratosphere and the troposphere and is called tropopause. Above this region the stratosphere is heated by exothermic photochemical reactions. Strong UV photons of a wavelength smaller than 240 nm are mainly absorbed by oxygen molecules producing atomic oxygen:

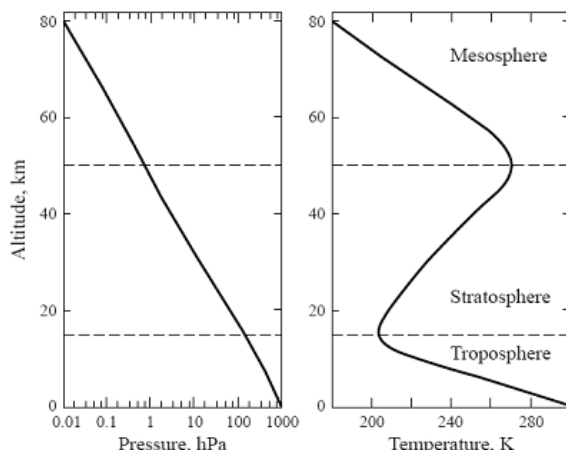


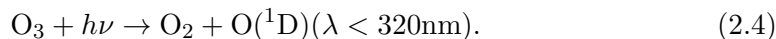
Figure 2.1: The variation of pressure and temperature on altitude in the atmosphere.



O atoms are in their ground-level triplet state and are highly reactive. They combine rapidly with oxygen molecules to form ozone:



M is a third body and acts as a stabiliser of the excited ozone molecule. These two reactions describe the formation of the stratospheric ozone layer. Ozone molecules filter the solar radiation protecting the organic life on the Earth by absorbing softer UV photons:



In the higher wavelength region where the ground-state atomic oxygen might be formed the ozone molecule is not an efficient absorber. If the ozone concentration is low, in other words the ozone layer is not ‘thick’ enough, referring to the conventional Dobson unit of ozone concentration, the ozone layer cannot prevent the biosphere from harmful UV radiation. In this case the so called ‘ozone hole’ occurs.

Different temperature, pressure and concentration of diverse species result in different kinds of chemistry at various altitudes. The atmospheric chemistry and,

more generally, the climate system have lots of components, as is schematised in Figure 2.2. Most atmospheric reactions take place in the gas phase but there are some reactions passing off in the aqueous phase or on a surface. In this thesis we are principally interested in heterogeneous processes and, therefore, the following subsections of this chapter will deal with the species involved in these processes. The reader will thus learn some details on the chemistry of OH radical, that of volatile organic compounds (VOCs) and polycyclic aromatic hydrocarbons (PAHs), and, at the end of this chapter, solid atmospheric particles, basically ice and soot, will be presented.

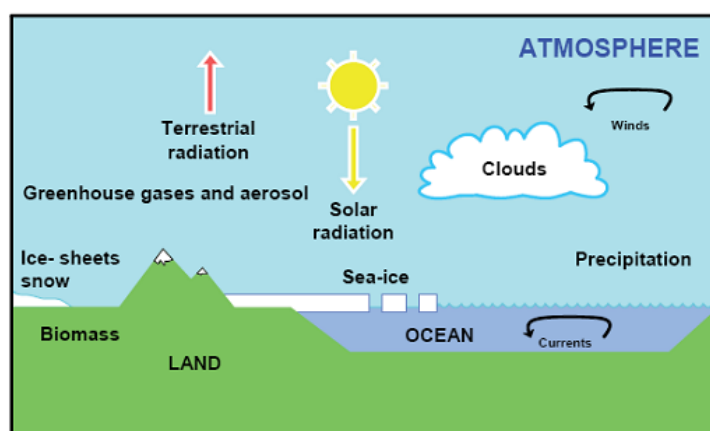


Figure 2.2: Schematic illustration of the climate system.

## 2.1 The OH radical

It has long been evidenced that the atmosphere is an oxidising medium[1, 2, 3]. Many environmentally important trace gases are removed from the atmosphere by oxidation. The most abundant oxidants in the Earth's atmosphere are  $O_2$  and  $O_3$ . These oxidants have large bond energies and are hence relatively unreactive except toward radicals. With a few exceptions, oxidation of non-radical atmospheric species by  $O_2$  and  $O_3$  is negligibly slow. Work in the 1950's first identified the OH radical as a strong atmospheric oxidant. OH reacts rapidly with most reduced non-radical species, and is particularly reactive toward H-containing molecules due to H-abstraction reactions converting OH to  $H_2O$ . OH is produced mainly by reaction of water vapour with  $O(^1D)$  formed in Eq 2.4:



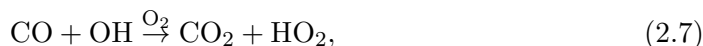
Critical to the generation of OH is the tropospheric production of excited  $\text{O}(^1\text{D})$  atoms in Eq 2.4, which is considerably slower than in the stratosphere. To complete the mechanism one should take into account the deactivation of the excited O atom by a neutral molecule, which leads to the loss of  $\text{O}(^1\text{D})$  slowing down Eq 2.5:



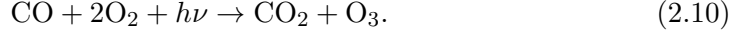
The slow formation and the deactivation of the excited O atom are compensated by the large  $\text{H}_2\text{O}$  mixing ratio compared to the stratosphere. Accurate estimation of the mean OH concentration established  $1.2 \times 10^6$  molecules  $\text{cm}^{-3}$ [2], and supported its importance as an oxidant in the troposphere. The mean lifetime of a given compound can be estimated in terms of the dominant reactions consuming it. CO turned out to be the principal sink of OH in most of the troposphere and  $\text{CH}_4$  is next in importance. These two gases therefore play a critical role in controlling OH concentration and more generally in driving radical chemistry in the troposphere. The resulting lifetime of OH is of the order of one second. Due to this short atmospheric lifetime, concentrations of OH are highly variable; they respond rapidly to changes in sources and sinks.

Atmospheric chemists suspected for a long while that there should be another substantial source of OH in the troposphere apart from Eq 2.5 and the stratospheric ozone supply because they seemed to be insufficient to prevent CO,  $\text{CH}_4$  and other greenhouse gases from accumulating to very high levels in the troposphere, with catastrophic environmental implications.

A key factor in this prevention is the presence of trace levels of  $\text{NO}_x$  ( $= \text{NO} + \text{NO}_2$ ) originating from combustion, lightning and soils. This key factor allows the regeneration of OH consumed in the oxidation of CO and hydrocarbons, and concurrently provides a major source of  $\text{O}_3$  in the troposphere. The main steps of this chain mechanism can be summarised in the following reactions:



The resulting net reaction is:



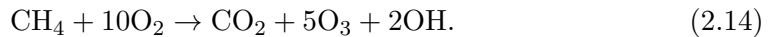
The net result is the production of ozone where the oxidation of CO by O<sub>2</sub> is catalysed by the HO<sub>x</sub> chemical family (HO<sub>x</sub> = H + HO + HO<sub>2</sub>), whereas the OH regeneration is catalysed by NO<sub>x</sub>. The resulting O<sub>3</sub> can generate additional OH.

In contrast, a considerably different behaviour can be observed in the stratosphere where HO<sub>x</sub> family catalyses ozone loss procedures. The hydroxyl radical produced in Eq 2.5 can react with ozone producing the hydroperoxy radical that reacts with another ozone molecule:



Recent work has shown that this HO<sub>x</sub>-catalysed mechanism represents, in fact, the dominant sink of ozone in the lowest stratosphere[3]. The basically different behaviour between the troposphere and the stratosphere arises from the fact that O<sub>3</sub> and O concentrations are much lower in the troposphere thus ozone destruction processes are a couple of orders of magnitude slower.

In the case of CH<sub>4</sub> the mechanism is much more complicated and is conducted through formaldehyde, organic peroxides and peroxide radicals. If we consider an atmosphere rich in NO<sub>x</sub> one can yield the following net reaction for the conversion of CH<sub>4</sub> to CO<sub>2</sub>:



The assumption of the high NO<sub>x</sub> concentration (high-NO<sub>x</sub> regime) results in five ozone molecules and two OHs per methane molecule. In contrast, if we examine an atmosphere deficient in NO<sub>x</sub> the resulting net reaction can be written as



This mechanism diminishes the oxidising power of the atmosphere. These two mechanisms emphasize the critical role of  $\text{NO}_x$  for maintaining  $\text{O}_3$  and OH concentrations in the troposphere.

Larger hydrocarbon molecules are less important than methane because their sources are minor compared to that of methane. They can, however, have a significant role in rapid production of ozone in polluted regions. Their oxidation and the oxidation of other VOCs are similar to the oxidation of methane. Complications emerge over the diverse issues of the organic oxy (RO) and peroxy ( $\text{RO}_2$ ) radicals and also over the structure and fate of oxygenated organic compounds.

## 2.2 VOCs in the atmosphere

VOCs are emitted into the atmosphere both from anthropogenic and biogenic sources. The most abundant VOCs released from these sources are methane and isoprene, respectively. The former gets to the atmosphere by fuel production and distribution, whereas the latter principally by biomass burning. Methane also has a large biogenic source. VOC may have effects on human health, plants and animals and also on the climate of the Earth. The direct negative effects on human health from VOC are local, mainly of concern close to the emission sources and in working environments, since it is only in these places that high concentrations of VOC are reached. Chlorinated VOC may bioaccumulate and survive long enough to reach the stratosphere where they may contribute to the ozone depletion. VOC also influences tropospheric ozone chemistry if  $\text{NO}_x$  concentration is high enough. As we have seen, ozone is crucial in the stratosphere to filter solar radiation; in the remote regions of the troposphere ozone is a non-negligible source of OH radical that prevents green house gases (GHGs) from catastrophic accumulation. Contrary to this, ozone in surface air is a harmful secondary pollutant and GHG. Production of  $\text{O}_3$  in polluted air follows the same chain mechanism as described above. The chain is initiated by production of OH and propagated by reaction of OH with VOCs. This reaction gives organic peroxy radical with the use of an oxygen molecule:

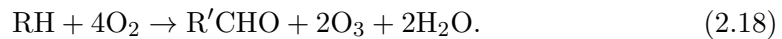


The importance of different VOCs in atmospheric chemistry depends on their abundance and their reactivity with OH. Increasing chain or unsaturated bonds increases the reactivity.

The  $\text{RO}_2$  radical reacts rapidly with  $\text{NO}$  to produce  $\text{NO}_2$  and an organic oxy radical:



The  $\text{RO}$  radical has several possible fates while  $\text{NO}_2$  goes on to photolyse and produce  $\text{O}_3$ . Typically, carbonyl compounds (usually aldehydes) and  $\text{HO}_2$  radical are produced in the reaction of  $\text{RO}$  and  $\text{O}_2$ . The carbonyl compound may either photolyse to produce  $\text{HO}_x$  or react with  $\text{OH}$  to propagate the reaction chain farther. The net reaction is



$\text{HO}$  is regenerated then from  $\text{HO}_2$  by  $\text{NO}$  similarly to Eq 2.8. The chain is terminated by the loss of the catalytic  $\text{HO}_x$  radicals. This loss takes place usually by the joint recombination of two peroxy radicals producing hydrogen peroxide:



The fate of the different VOCs is eventually the same: they are oxidised forming  $\text{CO}_2$  and  $\text{H}_2\text{O}$  which are the strongest green house gases. Some VOCs are themselves GHGs too. In the course of their oxidation they influence the formation of ozone to a different extent: Photochemical ozone creation potential (POCP) quantifies the impact of different VOCs on the ozone formation. This parameter aids environmentalists to develop different environmental policies for different VOCs. The determination of POCP values requires the analysis of the time evolution of the local concentration of different species by solving coupled balance equations (usually in computer modelling studies). A useful tool for that is ‘Master chemical mechanism’[5, 6], which contains the most important atmospheric processes and the related rate constants. POCP is defined relative to ethane (POCP of ethane is 100 by definition) and describes how efficiently the VOC generates ozone compared with ethane[7].

Besides the POCP value the lifetime of VOCs is also an important atmospheric feature in connection with their atmospheric impact. This refers both to how long they can influence the atmosphere as a GHG and the distance that VOCs are transported to. The atmospheric lifetime is defined in terms of the concentration of  $\text{OH}$  as being the major sink for VOCs:

VOC	POCP	Lifetime
HCOOH	1.5 <sup>a</sup>	20 days <sup>c</sup>
CH <sub>3</sub> COCH <sub>3</sub>	7.5 <sup>a</sup>	60 days <sup>c</sup>
Benzaldehyde	-10.4 <sup>b</sup>	18 hours <sup>c</sup>

Table 2.1: The lifetime and POCP values of the the VOCs studied here. <sup>a</sup> value taken from Ref. [5], <sup>b</sup> value taken from Ref. [6], <sup>c</sup> calculated on the basis of data found on MCM webpage [8]. The precision in an individual POCP value is estimated to be  $\pm 2$  POCP units.

$$\tau = \frac{1}{k[\text{OH}]},$$

where  $k$  is the rate constant of the oxidation reaction against the OH radical, and  $[\text{OH}]$  is the concentration of OH. In the next section we will focus on the three VOCs studied in my work.

### 2.2.1 Formic acid, acetone and benzaldehyde

The mean atmospheric lifetimes and POCP values of formic acid, acetone and benzaldehyde, the three volatile organic compounds which this thesis deals with are collected in Table 2.1.

As is seen in Table 2.1 these three VOCs are weak ozone-producing compounds. Benzaldehyde exceptionally decreases ozone production because one of its decomposition products makes a stable complex with NO<sub>2</sub> decreasing NO<sub>x</sub> in the atmosphere and slowing down the regeneration of OH. Benzaldehyde is a short-lived compound, thus it cannot be widely transported in the atmosphere, it affects atmosphere rather locally, at the place where it is released. Formic acid lives longer in the atmosphere: It can be transported vertically but its lifetime is not long enough to penetrate the stratosphere. Acetone is a long-lived compound, it can be widely spread and eventually participate in the stratospheric ozone depletion.

These three VOCs can be emitted from anthropogenic sources, but they can also be formed in the atmosphere. Benzaldehyde might be issued from the oxidation of styrene, whereas formic acid (that is known to be the most abundant organic acid in the atmosphere contributing thus to acidity in precipitation) might be the oxidation product of alkanes and alkenes. Acetone, which is one the most abundant VOC

originating from anthropogenic sources as being a fuel additive, might also issue from the oxidation of butane.

Their fate is similar: First they form peroxy radical in the course of their oxidation by OH radical. Then formic acid gives  $\text{CO}_2$  and  $\text{HO}_2$ . Benzaldehyde transforms to, among others, benzoic acid. The depletion of acetone is very complex. It gives methylglyoxal or decarboxylated products such as acetic acid or eventually formaldehyde.

## 2.3 PAH molecules in the atmosphere

Polycyclic aromatic hydrocarbons consist of fused aromatic rings and do not contain hetero atoms or substituents. Conventionally, benzene is not considered to be a PAH as having only one aromatic ring but one can use it as a model of PAH molecules. They are principally produced as by-products of incomplete fuel burning (either fossil fuel or biomass). As a pollutant, they are of concern because some compounds have been identified as carcinogenic, mutagenic and teratogenic. They are also found in the interstellar medium, in comets and in meteorites, and as a candidate molecule, act as a basis for earliest forms of life. In graphene the PAH motif is extended to large 2D sheets. Due to their low volatility they are found primarily in soil, sediment and they are also a component of concern in fine particles suspended in air (i.e. in aerosols). PAHs are among the most widespread pollutants. Their toxicity is very structurally dependent, varying from being non toxic to being extremely toxic.

It has been understood that the reactive fate of small and volatile PAHs is governed by gas-phase reactions with OH. However, due to their low vapour pressure and aromaticity, heavier PAHs are mostly adsorbed on fine carbonaceous particles[9], where they are subjected to a wide range of heterogeneous reactions which depend upon the particle composition[10, 11]. This heterogeneous reactivity may thus be more important than the corresponding gas phase reactions as sinks of these compounds. Moreover, heterogeneous reactions of particle-bound PAHs may change the microphysical properties of the particle by making it more hygroscopic and hence modifying its cloud nucleation properties[12]. These heterogeneous reactions can also influence the atmospheric residence times of the carbonaceous particles and consequently their direct and indirect effects on climate[4, 13]. During the incomplete combustion of fossil fuels, PAHs are formed concurrently with soot particles and play a significant role in soot formation and subsequent particle growth[14]. Because

PAHs have a high affinity for carbonaceous materials, adsorption of PAHs on soot may be an important mechanism affecting both the gas-particle partitioning of PAHs and also their reactivity.

## 2.4 Solid particles in the atmosphere

### 2.4.1 Ice particles

Water in the atmosphere is usually in a metastable supercooled state, which can be maintained in the absence of ice forming nuclei, providing that the temperature is higher than 231 K. In clouds containing some ice particles, water vapour can condensate directly onto ice according to the Bergeron process (homogeneous nucleation). Ice particles being large enough would be more likely to reach the surface by precipitation without evaporating. Note that homogeneous nucleation of ice particles directly from water vapour can also occur at very low temperature, typically less than 190 K, i.e., in the stratosphere above polar regions. This homogeneous freezing of ice particles participates in the occurrence of Polar Stratospheric Clouds (PSCs) that are involved in the ozone depletion mechanisms.

Clouds play a significant role in regulating the radiation balance of the Earth-atmosphere system, and are, hence, important components of the Earth's climate system. Clouds can absorb and re-radiate outgoing terrestrial radiation, and thereby act as a greenhouse gas. At the same time they can reflect incoming solar radiation back to space thus, in other words, they change the albedo (the reflective properties against the solar radiation) of the atmosphere. Which process dominates, and, hence, the arithmetic sign of the net radiative forcing of clouds appears to be very sensitive to the cloud microphysical and macrophysical properties[15]. Clouds can also alter the chemical composition by uptake of different species while heterogeneous reactions, for example of halogen species on the surface of cloud particles, can affect the atmospheric ozone budget[16].

In the case of heterogeneous condensation, water condensates onto so called 'cloud condensation nuclei' of which number and type can affect the amount, lifetimes and radiative properties of clouds and hence have an indirect influence on climate change; the details of this mechanism are still not well understood but are the subject of intensive research. Mineral dust, soot, sea salt and organic materials can act as cloud condensation nuclei. The effects of these tiny airborne particles called aerosols on cloud formation have been some of the most difficult aspects of weather and climate for scientists to understand.

### 2.4.2 Atmospheric aerosols and soot particles

Atmospheric aerosols consist of solid bodies suspended in air. These solid bodies have a radius changing from a few nanometres to hundreds of micrometres. Soot particles are of the major representatives of fine atmospheric aerosols that are considered to have a radius less than  $1\ \mu\text{m}$ . Fine aerosols originate almost exclusively from condensation of precursor gases. Besides soot particles, organic carbon and  $\text{H}_2\text{SO}_4 \cdot \text{H}_2\text{O}$  particles are also important components. The main effects of aerosols manifest basically in scattering solar radiation, which causes the reduction of visibility. The other main impact is the perturbation of climate, which arises by changing the albedo of the atmosphere. The impacts arising from scattering solar radiation are usually reflected in the so called ‘radiative forcing’ effect. Radiative forcing is defined as the change in the net radiation balance at the tropopause caused by a particular external factor. These forcing mechanisms are caused mainly by change in the atmospheric concentration of greenhouse gases (such as  $\text{CO}_2$ ,  $\text{CH}_4$  and  $\text{N}_2\text{O}$ ), but the change in the albedo of the climate system and atmospheric aerosols are not negligible sources either.

The size, concentration and chemical composition of atmospheric aerosols are quite diverse. Some aerosols are emitted directly into the atmosphere while others are formed in the air. Although the radiative forcing effect of aerosols can be changing, they are considered in average to have a negative effect (i.e. they decrease the temperature). Their direct radiative forcing effect comes from (elastic and inelastic) light scattering, which results finally in a decrease of solar radiation reaching the Earth’s surface. The indirect effect arises from the mechanisms by which aerosols modify the microphysical properties of clouds. These properties are related to the efficiency of aerosols for serving as nuclei in the condensation processes of water vapour. The nucleating properties depend on the size, the chemical composition of aerosols, and on the surrounding.

During the last few years, numerous studies have reported the radiative forcing effect of atmospheric soot particles. However, a couple of uncertainties arose concerning the direct and indirect effects of soot due to its optical, compositional and morphological diversity. To the best of our knowledge, the principal impact of soot on the atmosphere comes from the formation of contrails that evolve into artificial clouds. The formation of contrails is influenced by the altitude of flight, the properties and quantity of the emitted particles and propulsion mode of the aircraft etc[17, 18, 19]. The radiative effect induced by aviation is estimated to be about  $0.1\ \text{W m}^{-2}$ [20, 21]. In this estimation, uncertainties arise, which originate

from our defective knowledge of the climatic effects of contrails. Crude estimations provisioned an augmentation of a factor of 5 in the radiative forcing effects of the emission of air traffic in 2050[20]. The surface of sky covered by contrails is estimated to be 8% of that covered by natural clouds in the main air lanes[22, 23].

As we have said, soot can serve as nuclei in the formation of ice particles. Principally, two types of nucleation can be distinguished: homogeneous and heterogeneous nucleation. For the latter the presence of a solid particle is needed, whereas the former takes place without an initiator. Both of these two procedures depend strongly on temperature and relative humidity. Analyses have shown that particles participating in the formation of contrails consist mainly of carbon, which suggests the key role of soot particles in the nucleation[24, 25].

It has been evidenced that an activation of the soot surface is necessary to serve as a condensation nucleus[24, 25]. It means that there should be some hydrophilic sites at the soot surface, as was supported in 1987 by FTIR studies showing the presence of carboxyl groups at the surface of soot particles resulted from the oxidation of n-hexane by ozone[26, 27]. Earlier, an activation of the soot surface by sulphuric or nitric acid was considered to be necessary[24, 28, 29]. More recent studies evidenced that soot particles, issued from the combustion of decane, can adsorb water in the absence of oxidising acids[30]. These results suggest the presence of hydrophilic sites (structural defects, pores[31] or chemical groups) on or in the soot particles that are able themselves to attract water molecules.

From a structural point of view, three types of pores can be distinguished in soot: Macropores have a radius greater than 50 nm. Strong interaction between the adsorbent and adsorbate is needed for the adsorption at these sites (similarly to planar surfaces). Mesopores are considered to have a radius between 2 and 50 nm. In these pores capillary condensation may occur. Micropores are smaller than 2 nm; confinement effects are most pronounced here.

Adsorption isotherms of water on soot can support the hydrophilic character of soot as was done by comparing the adsorption isotherm of soot originated from the combustion of kerosene[31] and that of pure graphite[32]. The two isotherms can be seen in Figure 2.3. This graph suggests that the absence of defects on pure graphite results in very low affinity for water molecules. In contrast, the isotherm of the kerosene soot indicates the filling up of the smallest micropores and the adsorption of water molecules at the surface sites in the low pressure regime. The second part (relative humidity being between 0.1 and 0.7) corresponds to the adsorption of further water molecules around water molecules adsorbed previously serving as ‘secondary sites’; on the other hand, condensation in larger micropores takes also

place. Adsorption studies on active carbon showed that the shape of the isotherm depends strongly on the size distribution of the pores[33]. These results clearly show that the understanding of the adsorption mechanism of water on soot needs to quantify the influence of the porosity and chemical composition of soots.

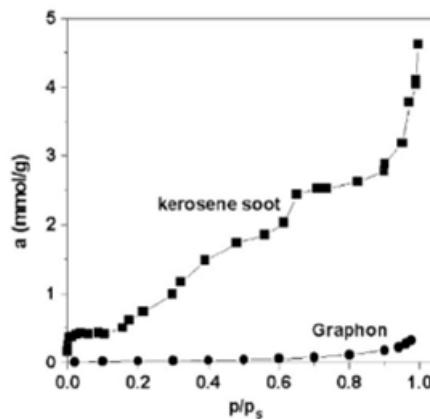


Figure 2.3: Comparison of the adsorption isotherms obtained on kerosene soot at 295 K (rectangles) and on pure graphite at 291 K (circles)[31].

**Composition of soot particles.** The composition of soot has been determined by X-ray spectroscopy[34]. This study shows that soot is composed principally of carbon (85–98%) but sometimes a large oxygen content can also be identified, being between 2 and 13%. Some traces of sulphur and iron can be observed occasionally too. A complementary Raman spectroscopic analysis showed the presence of C=O and OH functional groups in soot, but, depending on the way the soot was formed, C=O groups are sometimes dominant and OH cannot be observed at all.

**Formation of soot particles.** It has been evidenced that soot formation processes depend on the conditions of combustion, the type of fuel and the combustion chamber of the engine. Generally, one can distinguish the following steps of soot formation: First, the formation of basic nuclei, mostly polyenes (being described by the chemical formula  $C_{2n}H_2$ ,  $n=1..8$ ) and PAHs[35] takes place. Secondly, the size of these nuclei increases by heterogeneous reaction on their surface resulting in ‘primary particles’ that have a diameter of about 1.5 nm[33, 35, 36]. Unfortunately, the details of these reactions are not entirely clarified yet. The last step is the formation of large agglomerations and coagulations of soot being visible by transmission electron microscope and having a size of 50 nm[35, 37, 38].

**Structural and compositional study of soot.** In situ laboratory analysis of soot particles originating from aircrafts is nearly impossible, thus researchers are

restrained to study soot produced in laboratory. Usually, for laboratory purposes kerosene is too expensive. Furthermore, instead of aircraft engine combustion chambers or burners are used. These facts lead to a great variety of results, which are sometimes even contradictory. To facilitate the research concerning soot, some experimental protocols for soot generation have been used over the last few years. In despite of the great diversity of soot, the following structural fractions can be distinguished: on one hand, a great fraction consisting of amorphous soot and, on the other hand, more organised structures such as multiwall nanotubes and onion-like particles[34, 39, 40]. Detailed analysis of these onion-like particles revealed that they consist of 2–4 graphite sheets having a diameter of 2–3 nm and being separated by the same (or sometimes slightly larger) distance as the inter-planar distance in graphite i.e. 3.4 Å[40]. Onion-like particles are illustrated in Figure 2.4.

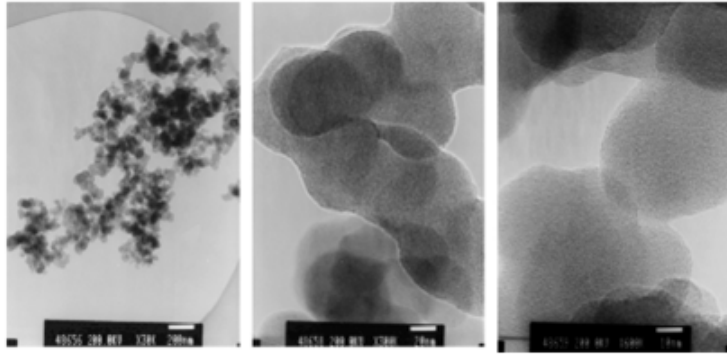


Figure 2.4: TEM images of kerosene soot on different scales (200, 20 and 10 nm).

## Chapter 3

# Computational methods

### 3.1 Computer simulation methods

Statistical physics aims at describing the *macroscopic* properties of a system on the basis of the *microscopic* characteristics of every particle constituting the system. This objective requires, however, unimaginably great amounts of information about the system. One would have to entirely know the position and momentum of each particle at each moment of time. The knowledge of this amount of information is clearly impossible. But even if one knew all information a second problem, rather of a mathematical nature, would arise: the integration of nearly infinite microscopic properties seems to be unachievable. Statistical physics, however, proved to be a useful tool for the description of reality. Reasonable approximations for the *average behaviour* of particles constituting the system made it applicable in numerous cases.

Computer simulation techniques are obvious tools for the application of the equations of statistical physics because no approximation has to be used to gain the average properties of the system. It is possible to determine them by observation of the motion of the particles during the simulation. This is why computer simulations are often called *numerical experiments*. Limitations come from the restricted number of particles observed in the simulation and also from the limited time available for the simulation. Nevertheless, there are properties that can be quite accurately calculated in a finite system during a finite simulation time.

There are two principal ways to determine the average properties of the system. One may calculate them as a mean value integrated either in time or over the ensemble of microstates of the entire phase space. The former needs almost infinitely long simulation to guarantee the system passes through all microstates of the phase

space (i.e. the system fulfills the requirement of ergodicity), whereas the latter necessitates the knowledge of the probability of being in each microstate of the phase space. The ergodic hypothesis states the equality of the time average gained by the first approach and the ensemble average yielded by the second:

$$\langle A \rangle_t = \lim_{\tau \rightarrow \infty} \frac{1}{\tau} \int_0^\tau dt A(\mathbf{q}(t), \mathbf{p}(t)) = \int d\mathbf{q}d\mathbf{p} A(\mathbf{q}, \mathbf{p}) f(\mathbf{q}, \mathbf{p}) = \langle A \rangle_\Gamma, \quad (3.1)$$

where  $\mathbf{p}$  and  $\mathbf{q}$  denote the momenta and the spatial coordinates of all particles respectively;  $A(\mathbf{q}, \mathbf{p})$  represents the value of quantity  $A$  at the  $\Gamma \equiv \{\mathbf{q}, \mathbf{p}\}$  point (i.e. a microstate) of the phase space,  $\langle A \rangle$  is the mean (i.e. macroscopic) value of  $A$ ;  $f(\mathbf{q}, \mathbf{p})$  is the probability density function over the microstates,  $t$  is the time while  $\tau$  is the duration of observation. In the above equation the left hand side gives the principle of molecular dynamics, while the right hand side gives that of Monte Carlo method.

Both techniques need the generation of microstates of the system being described by the same macroscopic state functions. In molecular dynamics (MD)[41] methods the generation of microstates is done by the numerical integration of the equations of motion of each particle of the system for a short time step (usually in the order of a femtosecond). The integration gives the new molecular positions of the particles. Here, the atomic configurations generated step by step have time correlation and they depend on the previous configurations. This feature makes the molecular dynamics methods capable of calculating dynamical, time-dependent properties besides time-independent ones. During the simulation, the system visits the microstates of the phase space available as frequently as is dictated by the probability density function (if the simulation is long enough). One can also simulate non-equilibrium processes with this method. The drawback is that the calculation of forces and the numerical integration are quite time consuming.

On the contrary, Monte Carlo (MC)[41] methods are considered to be stochastic methods. Here, the generation of a new configuration is accomplished by a random change in the current configuration of the system. Then the generated configuration will be accepted or rejected according to the acceptance criterion. Because the generation of the new configuration needs only the knowledge of the current one (and not of the previous ones), the set of the configurations has no memory. It is therefore impossible to simulate non-equilibrium processes with MC methods. Due to the lack of explicit appearance of time in the equations of the MC method, it is also impossible to obtain time-dependent quantities with MC methods. The great

advantage of MC methods in contrast with MD is rapidity: the time needed for an MC step is 1–2 orders of magnitude smaller than that of MD.

### 3.1.1 Monte Carlo method

MC methods are widely used in science where random sampling from a given ensemble may yield the approximate solution to a problem. In physics usually one has to sample from the phase space according to the probability density function, which can be given as

$$f(\mathbf{q}, \mathbf{p}) = \frac{\exp(-\beta\mathcal{F}(\mathbf{q}, \mathbf{p}))}{\int d\mathbf{q}d\mathbf{p} \exp(-\beta\mathcal{F}(\mathbf{q}, \mathbf{p}))} = \frac{1}{N!h^{3N}} \frac{\exp(-\beta\mathcal{F}(\mathbf{q}, \mathbf{p}))}{Q}, \quad (3.2)$$

where  $\beta = \frac{1}{k_B T}$ ,  $k_B$  denotes the Boltzmann constant,  $T$  is the absolute temperature and  $\mathcal{F}(\mathbf{q}, \mathbf{p})$  is an energy-like potential function depending on the boundary conditions of the thermodynamical ensemble of the system.  $Q$  is the normalising factor of the density function and is often called partition function:

$$Q = \frac{1}{N!h^{3N}} \int d\mathbf{q}d\mathbf{p} \exp(-\beta\mathcal{F}(\mathbf{q}, \mathbf{p})). \quad (3.3)$$

In the above equations the division by  $N!$  is needed to take into account that the permutation of  $N$  particles constituting the system does not increase the number of microstates, whereas the factor  $h^{3N}$  ( $h$  being the Planck constant) accounts for the fact that within a unit volume of this size in the phase space the quantum states are already indistinguishable, thus the number of microstates must be reduced by this factor.

Because only position-dependent quantities can be obtained the sampling narrows only to the position-dependent part of the phase space (which is often called configurational space), and the momentum-dependent parts can be separated and integrated out of the density function. The mean value of  $A$  takes the following form:

$$\langle A \rangle = \frac{\int d\mathbf{p} \exp(-\beta\mathcal{F}_p(\mathbf{p})) \int d\mathbf{q} A(\mathbf{q}) \exp(-\beta\mathcal{F}_q(\mathbf{q}))}{\int d\mathbf{p} \exp(-\beta\mathcal{F}_p(\mathbf{p})) \int d\mathbf{q} \exp(-\beta\mathcal{F}_q(\mathbf{q}))} = \frac{\int d\mathbf{q} A(\mathbf{q}) \exp(-\beta\mathcal{F}_q(\mathbf{q}))}{\int d\mathbf{q} \exp(-\beta\mathcal{F}_q(\mathbf{q}))}, \quad (3.4)$$

where  $\mathcal{F}_p(\mathbf{p})$  is the momentum-dependent, while  $\mathcal{F}_q(\mathbf{q})$  is the position-dependent part of the potential function, fulfilling  $\mathcal{F}(\mathbf{q}, \mathbf{p}) \equiv \mathcal{F}_p(\mathbf{p})\mathcal{F}_q(\mathbf{q})$ . The denominator here is often called configurational integral. Instead of the integration one may

write summation in Eq 3.4 because in practice, one would study only a finite set of configurations:

$$\langle A \rangle \approx \frac{\sum_{i \in \mathcal{S}} A(\mathbf{q}_i) \exp(-\beta \mathcal{F}_q(\mathbf{q}_i))}{\sum_{i \in \mathcal{S}} \exp(-\beta \mathcal{F}_q(\mathbf{q}_i))}, \quad (3.5)$$

where  $i$  runs over all atomic configurations (microstates)  $\mathbf{q}_i$  in set  $\mathcal{S}$ . At this point, further refinement of the method is necessary, otherwise the contributions of the entirely random configurations to the mean value of  $A$  would likely be very small due to the high value of  $\mathcal{F}_q(\mathbf{q}_i)$ . This is related to the likely ‘unphysical’ structures generated randomly, which results in a small statistical factor (that decreases exponentially with  $\mathcal{F}_q$ ), so the convergence of the mean value would be very slow. The trick one has to use here was first described by Metropolis and co-workers[42] and is that configurations with relatively low  $\mathcal{F}_q$  value are more likely to be chosen, which results in distortion of the randomness of the sampling. The distortion can be corrected thus:

$$\langle A \rangle \approx \frac{\sum_{i \in \mathcal{S}} A(\mathbf{q}_i) \frac{\exp(-\beta \mathcal{F}_q(\mathbf{q}_i))}{w_i}}{\sum_{i \in \mathcal{S}} \frac{\exp(-\beta \mathcal{F}_q(\mathbf{q}_i))}{w_i}}, \quad (3.6)$$

where  $w_i$  is the sampling weight factor of the  $i$ th configuration. If this factor equals just  $\exp(-\beta \mathcal{F}_q(\mathbf{q}_i))$  the weighted expectation value of the quantity  $A$  becomes simply the arithmetic mean of the  $A(\mathbf{q}_i)$  values.

One thus gains on one hand, the rapid convergence of the expectation value and, on the other hand, the simplicity of the expression at the expense of the biased Metropolis algorithm. As an example, we will demonstrate how this algorithm is applied in the simplest case, i.e., in the case of the canonical  $(N, V, T)$  ensemble.

Since the energy-like potential function related to the canonical ensemble is the total energy itself, its position-dependent part is simply the potential energy (i.e.,  $\mathcal{F}_q \equiv U$ ), and thus the sampling factor becomes

$$w_i(\mathbf{q}_i) = \exp(-\beta U(\mathbf{q}_i)). \quad (3.7)$$

The procession of the algorithm starts with making a random change in the initial configuration. In the second step, the calculation of the potential energy corresponding to the new atomic configuration is performed. Thirdly, if the potential energy decreases the new configuration is always accepted. Otherwise it is accepted only by a probability of  $\exp(-\beta \Delta U(\mathbf{q}))$ , and is rejected by  $(1 - \exp(-\beta \Delta U(\mathbf{q})))$ , where

$\Delta U(\mathbf{q})$  is the difference in potential energy between the current and previous state of the system (and is positive in this case). In practice, we generate a random number  $\xi$  between 0 and 1. If  $\xi$  is greater than  $\exp(-\beta\Delta U(\mathbf{q}))$  the generated configuration is rejected, otherwise it is accepted. The acceptance probability can be represented thus as

$$P_{\text{acceptance}} = \min(1, \exp(-\beta\Delta U(\mathbf{q}))). \quad (3.8)$$

One can demonstrate that, if the algorithm proceeds in this way, the sampling is indeed done according to the probability density function of the microstates[42]. In the next subsection we will demonstrate how the Metropolis algorithm is applied on the grand canonical ensemble.

### 3.1.1.1 Grand canonical Monte Carlo method

This method was developed independently by Norman and Filinov[43] and also by Adams[44, 45].

Instead of the number of particles, the chemical potential is kept constant here together with the temperature and volume. The condition of being in equilibrium of a system on this ensemble is the minimality of the grand potential defined as

$$\Omega = \mathcal{A} - N\mu = -pV, \quad (3.9)$$

where  $\mathcal{A}$  is the Helmholtz free energy,  $N$  is the number of particles,  $\mu$  is the chemical potential,  $p$  is the pressure, and  $V$  is the volume of the system. The grand canonical partition function is given as

$$\Xi = \sum_{N=1}^{\infty} \frac{1}{N!h^{3N}} \int d\mathbf{q}d\mathbf{p} \exp(\beta(N\mu - E(\mathbf{q}, \mathbf{p}))), \quad (3.10)$$

whereas the expectation value of an arbitrary macroscopic quantity is

$$\langle A \rangle = \frac{\sum_{N=1}^{\infty} \frac{1}{N!h^{3N}} \int d\mathbf{q}d\mathbf{p} A(\mathbf{q}, \mathbf{p}) \exp(\beta(N\mu - E(\mathbf{q}, \mathbf{p})))}{\Xi}, \quad (3.11)$$

where  $E$  is the energy of the system. On the grand canonical ensemble, contrary to the canonical ensemble, one has to sample from phase spaces of different numbers of particles having the same chemical potential. After having integrated out the momentum-dependent part of the density function and that of the partition function,

the resulting coefficient  $\left(\frac{2\pi m}{\beta}\right)^{3N/2}$  ( $m$  denoting the mass of a single particle) does not cancel out due to the changing number of particles. Therefore, one gets

$$\langle A \rangle = \frac{\sum_{N=1}^{\infty} \frac{1}{N!} \left(\frac{2\pi m}{\beta h^2}\right)^{3N/2} \int d\mathbf{q} A(\mathbf{q}) \exp(\beta(N\mu - U(\mathbf{q})))}{\sum_{N=1}^{\infty} \frac{1}{N!} \left(\frac{2\pi m}{\beta h^2}\right)^{3N/2} \int d\mathbf{q} \exp(\beta(N\mu - U(\mathbf{q})))}. \quad (3.12)$$

Conventionally, the following notation can be introduced:

$$\Lambda = \sqrt{\frac{\beta h^2}{2\pi m}}, \quad (3.13)$$

this quantity is often referred to as the thermal de Broglie wavelength. It is convenient to use scaled coordinates instead of spatial ones:

$$s = qV^{1/3}, \quad (3.14)$$

where  $s$  and  $q$  denote only one coordinate of a particle. Using these notations Eq 3.12 takes the following conventional form:

$$\langle A \rangle = \frac{\sum_{N=1}^{\infty} \int d\mathbf{s} A(\mathbf{s}) \frac{V^N}{N! \Lambda^{3N}} \exp(\beta(N\mu - U(\mathbf{s})))}{\sum_{N=1}^{\infty} \int d\mathbf{s} \frac{V^N}{N! \Lambda^{3N}} \exp(\beta(N\mu - U(\mathbf{s})))}. \quad (3.15)$$

The sampling weight factor is thus in this case:

$$\begin{aligned} w_i(\mathbf{s}, N) &= \frac{V^N}{N! \Lambda^{3N}} \exp(\beta(N\mu - U(\mathbf{s}))) = \\ &= \exp \left[ N \ln \left( \frac{V}{\Lambda^3} \right) - \ln(N!) - \beta(U(\mathbf{s}) - N\mu) \right]. \end{aligned} \quad (3.16)$$

In the grand canonical MC technique there are three different types of move: i) a particle is displaced; ii) a particle is destroyed (no record of its position is kept); iii) a particle is created at a random position in the system. Thus the acceptance ratio is:

$$P_{acceptance} = \min \left\{ 1, \exp \left[ \Delta \left( N \ln \left( \frac{V}{\Lambda^3} \right) - \ln(N!) - \beta(U(\mathbf{s}) - N\mu) \right) \right] \right\}. \quad (3.17)$$

which reduces to the normal Metropolis method in the case of particle displacement ( $\Delta N = 0$ ):

$$P_{acceptance} = \min(1, \exp(-\beta\Delta U(\mathbf{s}))). \quad (3.18)$$

The acceptance of the addition or removal of more than one particle proved to be very improbable in dense systems[43], thus in one step, the creation or destruction of only one particle is attempted. The acceptance criterion in these cases becomes

$$P_{acceptance} = \min \left\{ 1, \exp \left[ \ln \left( \frac{V}{\Lambda^3} \right) - \ln(N+1) - \beta(\Delta U(\mathbf{s}) - \mu) \right] \right\}, \quad (3.19)$$

in the case of creation (i.e.  $\Delta N = 1$ ), and

$$P_{acceptance} = \min \left\{ 1, \exp \left[ -\ln \left( \frac{V}{\Lambda^3} \right) + \ln(N) - \beta(\Delta U(\mathbf{s}) + \mu) \right] \right\}, \quad (3.20)$$

in the case of destruction (i.e.  $\Delta N = -1$ ).

The condition of microscopic reversibility can be satisfied by making the probability of an attempted creation equal to the probability of an attempted destruction. Norman and Filinov suggested setting the probability of attempting the three moves equal, because fastest convergence can be achieved in this way.

The great advantage of the GCMC method is that equilibria in highly inhomogeneous systems, such as adsorption processes or membranes are easy to simulate. It should be noted that the Monte Carlo method is dominant as opposed to the molecular dynamics on the grand canonical ensemble because the destruction and creation of particles sets serious technical problems in dynamical simulations.

It should also be noted that with increasing density the probability of successful creation or destruction steps becomes small. Creation attempts fail because of the high risk of overlap. Destruction in the vicinity of a surface may be also infrequent and this somewhat offsets the advantage of GCMC in the simulation of adsorption. To address these problems, Mezei[46, 47] extended the basic method to search for cavities in the system which are of an appropriate size to support the creation. Once these cavities are located, creation attempts are only made inside the cavities. This method is referred to as the cavity-biased GCMC method. Further details on the biased insertion techniques can be found in Appendix A.

It should be noted that a reformalisation of the GCMC method suggested by Adams for the chemical potential can be used, which splits it into the ideal gas and excess part:

$$\mu = \mu^{ex} + \mu^{id} = \mu^{ex} + kT \left[ \ln \langle N \rangle_{\mu, V, T} + \ln \left( \frac{\Lambda^3}{V} \right) \right] = kTB + kT \ln \left( \frac{\Lambda^3}{V} \right), \quad (3.21)$$

where  $B$  accounts for the terms that are not known usually at the beginning of the simulation such as the excess chemical potential and the average number of a given molecule type:

$$B \equiv \frac{\mu^{ex}}{kT} + \ln \langle N \rangle_{\mu, V, T}, \quad (3.22)$$

and, on the other hand, as a consequence of Eq 3.21:

$$B = \frac{\mu}{kT} - \ln \left( \frac{\Lambda^3}{V} \right). \quad (3.23)$$

Adams performed grand canonical Monte Carlo simulations at constant  $B$ ,  $T$  and  $V$  where  $B$  is defined in the above equations. It is obvious that this technique is completely equivalent to the method at constant  $\mu$ ,  $T$  and  $V$ .

### 3.1.2 Molecular dynamics

In molecular dynamics simulations, the next configuration is generated by solving the equations of motion of each particle in the system. First, one has to define the Hamiltonian that exists for all mechanical systems. The Hamiltonian  $H$  is the total energy, namely it is the sum of the kinetic energy  $K$  and potential energy  $U$ , thus, in classical mechanics:

$$H(\mathbf{q}, \mathbf{p}) \equiv K(\mathbf{p}) + U(\mathbf{q}). \quad (3.24)$$

The equations of motion in the Hamiltonian formalism are

$$\dot{\mathbf{q}}^i = \frac{\partial H(\mathbf{q}, \mathbf{p})}{\partial \mathbf{p}^i} = \frac{\mathbf{p}^i}{m_i}, \quad (3.25)$$

$$\dot{\mathbf{p}}^i = -\frac{\partial H(\mathbf{q}, \mathbf{p})}{\partial \mathbf{q}^i} = -\frac{\partial U(\mathbf{q})}{\partial \mathbf{q}^i} \equiv F_i, \quad (3.26)$$

where  $\mathbf{q}^i$ ,  $\mathbf{p}^i$  and  $m_i$  are the location, the momentum and the mass of the  $i$ th particle respectively. Eq 3.25 and Eq 3.26 describe a system of  $6N$  first order differential

equations. The analytical solution of this system of equations is impossible, therefore numerical methods should be applied.

Many methods were introduced to solve these equations, in all of which the simulation proceeds by alternately calculating forces and solving the equations of motion based on the accelerations obtained from the new forces. For example, in the Verlet-Störmer algorithm, Eq 3.26 is solved directly[48]. First, writing the Taylor expansion of the coordinate vector at  $t_0 + \Delta t$  and  $t_0 - \Delta t$  around time  $t_0$

$$\mathbf{q}^i(t_0 + \Delta t) = \sum_{n=0}^{\infty} (\Delta t)^n \frac{1}{n!} \frac{\partial^n \mathbf{q}^i}{\partial t^n}(t_0), \quad (3.27)$$

$$\mathbf{q}^i(t_0 - \Delta t) = \sum_{n=0}^{\infty} (-1)^n (\Delta t)^n \frac{1}{n!} \frac{\partial^n \mathbf{q}^i}{\partial t^n}(t_0), \quad (3.28)$$

and, adding them up, only the even-order terms remain:

$$\mathbf{q}^i(t_0 + \Delta t) = 2\mathbf{q}^i(t_0) - \mathbf{q}^i(t_0 - \Delta t) + (\Delta t)^2 \ddot{\mathbf{q}}^i(t_0) + \mathcal{O}\left((\Delta t)^4\right). \quad (3.29)$$

According to this algorithm, to calculate the position of atom  $i$  at the next time step, one has to use the current and previous position and the current acceleration coming from the force applied on particle  $i$ . If one does so, the algorithm error occurs only in fourth order. However, this algorithm has a great drawback, namely that the error of the velocity in the next moment is of second order. Therefore, either the more accurate velocity-Verlet method or predictor-corrector algorithms are usually applied to overcome this problem. For the integration it is fundamental to choose an appropriate time step length  $\Delta t$ , which has to be in the same order of magnitude as the time scale of the studied particle motions; in molecular systems the value of  $\Delta t$  is typically around 0.5 – 2 fs.

### 3.1.3 Potential models used

The importance of the potential model in classical simulations is emphasised because it determines the behaviour of not only each single particle but that of the whole system as well, and it eventually also defines the entire structure of the system. The potential has to be differentiable, since forces are calculated as its derivatives and, on the other hand, the calculation of forces and of the potential itself should be quick to ensure the efficiency of the simulation. In classical simulations classical

potentials are used, which may be adjusted to different (usually experimental) properties of the macroscopic system to be simulated. These potentials are thus able to reproduce some properties well and some others less well. Classical potentials may not reproduce properties well that they are not designed for, the potential used therefore always has to be chosen circumspectly.

There are two main groups of potentials: The first, widely used group is that of non-reactive potentials that describe bonded and non-bonded interactions, but cannot change the atomic environment of the particles. The second group incorporates the reactive potentials, which can reproduce bond breaking and forming together with bonded and non-bonded interactions.

### 3.1.3.1 Non-reactive potentials

The potential energy in the whole system can be given as[41]

$$U(\mathbf{q}) = \sum_{i=1}^N u_1(\mathbf{q}^i) + \sum_{i=1}^N \sum_{j>i}^N u_2(\mathbf{q}^i, \mathbf{q}^j) + \sum_{i=1}^N \sum_{j>i}^N \sum_{k>j>i}^N \Delta u_3(\mathbf{q}^i, \mathbf{q}^j, \mathbf{q}^k) + \dots + \Delta u_N(\mathbf{q}^1, \mathbf{q}^2, \dots, \mathbf{q}^N). \quad (3.30)$$

The first summation of the equation describes the effect of an external potential, while the second term sums the pair interactions of all possible particle pairs. The third term ( $\Delta u_3$ ) contains the additional energy of particle triplets compared to isolated pairs. Obviously, the list has to be continued until the final term, which includes the interaction of all the  $N$  particles not included in the previous sums. Although this expression is exact, it cannot be used because the form of the terms in the above equation is unknown.

In practice, the potential is approximated by the sum of, at most, pairwise additive terms:

$$U(\mathbf{q}) \approx \sum_{i=1}^N u_1(\mathbf{q}^i) + \sum_{i=1}^N \sum_{j>i}^N u_2^{eff}(\mathbf{q}^i, \mathbf{q}^j). \quad (3.31)$$

The term  $u_2^{eff}(\mathbf{q}^i, \mathbf{q}^j)$  does not equal  $u_2(\mathbf{q}^i, \mathbf{q}^j)$  in Eq 3.30, and it is often called effective pair potential, and accounts also for the contribution of multi-particle terms to the potential energy in an average way. If there is no external field, the first term can be neglected, while in the case of an isotropic system, the effective pair potential depends only upon the distance between two particles  $r_{ij}$ :

$$U(\mathbf{q}) \approx \sum_{i=1}^N \sum_{j>i}^N u_2^{eff}(r_{ij}). \quad (3.32)$$

There are numerous pair potentials in the literature. The simplest one is the hard sphere potential, which creates no interaction between two particles if they are farther from each other than a distance  $r$ , where an infinite repulsion arises between them. Other common pair potentials exist with a simple attractive part, such as a constant or a linearly changing attraction in a distance range (e.g. square-well or triangle-well potential). Although these potentials are very simple, they are capable of reproducing some basic properties of real systems, such as solid-fluid phase transition[41]. Clearly, to study realistic systems a more sophisticated and continuously changing pair potential function is needed. The Morse potential or more often the Lennard-Jones potential is a suitable choice for this purpose:

$$U^{LJ}(r) = 4\epsilon \left[ \left( \frac{\sigma}{r} \right)^{12} - \left( \frac{\sigma}{r} \right)^6 \right], \quad (3.33)$$

where  $\sigma$  and  $\epsilon$  are parameters, representing the ‘size’ of the particle and the ‘strength’ of the attraction respectively. These simple pair potentials are illustrated in Figure 3.1.

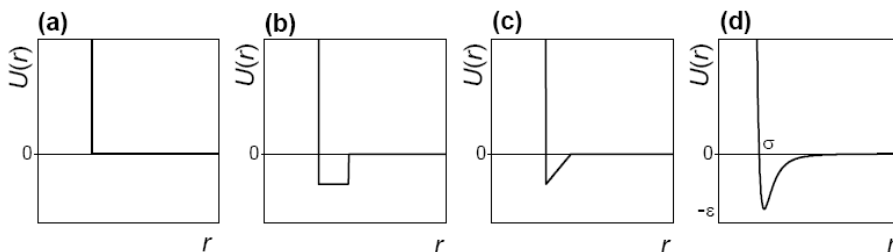


Figure 3.1: Some simple pair potentials: hard sphere potential (a), square-well potential (b), triangle potential (c) and Lennard-Jones potential (d).

Usually, interaction parameters are defined between the same type of interaction sites, thus to calculate those between different sites, the mixing of parameters is needed. The most widely used mixing rule is the Lorentz-Berthelot rule[41]:

$$\epsilon_{AB} = \sqrt{\epsilon_A \epsilon_B} \quad \text{and} \quad \sigma_{AB} = \frac{\sigma_A + \sigma_B}{2}. \quad (3.34)$$

In the case of charged particles the electrostatic part of the interaction also has to be calculated. Although quite sophisticated methods have been developed based

on the distribution of electric multipole moments on different sites of the interacting molecules these last years to calculate the electrostatic interactions between two charged species[49], the simple Coulomb law involving only charge distributions on the interaction sites is still widely used due to its simplicity. The Coulomb equation reads:

$$U^C(r) = \frac{1}{4\pi\epsilon_0} \frac{q_A q_B}{r}, \quad (3.35)$$

where  $\epsilon_0$  is the vacuum permittivity,  $q_A$  and  $q_B$  are the charges of interaction sites  $A$  and  $B$ .

Note finally, that a series of potential models has also been developed to take into account polarisation effects in numerical simulations. However, the introduction of such models in numerical codes is a non trivial task. Furthermore, the corresponding results are not necessarily better than those obtained when using simple pair potentials because an accurate parametrisation of the polarisable potentials is quite difficult to achieve. Of course, these polarisation effects may be of great importance when simulating systems containing a net charge, such as ions.

### 3.1.3.2 Reactive potentials

Reactive potentials are efficient in the classical simulation of chemical reactions by empirical modelling of changes in covalent bonding. The principle of reactive potentials is that they switch on chemical forces at a certain distance where non-bonded interactions are repulsive due to the overlap of particles. One of the most widely used reactive potentials is empirical valence bond (EVB) potential developed by Warshel's group[50]. This potential was successfully used to model proton transfer reactions in aqueous acids. Another example of reactive potentials is RWFF[51] (reactive force field for water) that was developed to reproduce water neutron scattering data accurately. A third one, ReaxFF[52] was fitted to ab initio calculations and empirical bond energies. Calculations with these force fields have been proved to be much faster than ab initio or even semi-empirical calculations. Their accuracy is similar to or sometimes even better than that of semi-empirical methods.

The concept of the reactive bond order (REBO) force field of Brenner[53] is similar: it takes into consideration the local coordination of atoms and the bond order of chemical bonds in the calculation of the total energy of the system. The original goal was to model the chemical vapour deposition of diamond films, because the mechanism of growth of diamond films from the vapour of hydrocarbons was not clear.

Brenner developed an empirical potential energy function (based on empirical bond energies) that captures the key features of chemical bonding in hydrocarbons, and satisfies the following considerations. The potential i) reproduces the intermolecular energetics and bonding in diamond, graphite and various hydrocarbons, ii) yields realistic properties for general structures, iii) allows for bond breaking and forming, and iv) is not computationally intensive.

The base of the method is an Abell-Tersoff potential energy expression that was originally designed by Abell to explain universal tendencies in binding-energy curves, with the sum of neighbour pair interactions moderated by the local atomic environment[54]. Tersoff introduced an analytic potential energy function[55] that realistically describes bonding in silicon for a couple of solid states. Thus the binding energy in the Abell-Tersoff formalism is written as a sum over atomic sites  $i$ :

$$E_b = \frac{1}{2} \sum_i E_i, \quad (3.36)$$

where each contribution  $E_i$  is written as

$$E_i = \sum_{j \neq i} (V_R(r_{ij}) - B_{ij}V_A(r_{ij})). \quad (3.37)$$

In this equation  $j$  goes over the neighbours of atom  $i$ .  $V_R$  and  $V_A$  are pair-additive repulsive and attractive interactions, respectively, and  $B_{ij}$  represents a many-body coupling between the bond  $i - j$  and local environment of atom  $i$ . If  $V_R$  and  $V_A$  are Morse-type functions,  $B_{ij}$  can be considered a normalised bond order[54, 55]. Abell suggested, to a first approximation, that  $B_{ij}$  can be given in function of the local coordination  $Z$ :

$$B_{ij} \propto Z^{-\delta}, \quad (3.38)$$

where  $\delta$  depends on the particular system. Tersoff adjusted the pair terms and an analytic function for  $B_{ij}$ , and obtained quite good accuracy and transferability for silicon, germanium and carbon. In spite of these issues, this potential has a number of deficiencies, e.g., it is unable to properly describe conjugation and radicals.

To correct the deficiencies of the Abell-Tersoff potential Brenner suggested rewriting the above equations while maintaining the fit to diamond and graphite:

$$E_b = \sum_i \sum_{j>i} (V_R(r_{ij}) - \bar{B}_{ij}V_A(r_{ij})), \quad (3.39)$$

where the repulsive and attractive terms have a Morse-like form and are multiplied by a function, which restricts the potential to nearest neighbours by switching off the chemical forces beyond a certain distance. The empirical bond-order function is given by the average of terms associated with each atom in a bond plus a second term taking into account non-local effects:

$$\bar{B}_{ij} = (B_{ij} + B_{ji})/2 + F_{ij}(N_i^{(t)}, N_j^{(t)}, N_{ij}^{(conj)}), \quad (3.40)$$

where  $N_i^{(t)}$  and  $N_j^{(t)}$  are the total number of neighbours (H + C) bonded to atom  $i$  and  $j$ , respectively, while  $N_{ij}^{(conj)}$  depends on whether the bond  $i - j$  (between two carbons) is part of a conjugated system, and can be even a fraction.  $F_{ij}$  is a three-dimensional cubic spline function to make the potential change continuously. The  $B_{ij}$  bond-order term depends on the number of H and C neighbours and also contains an angle dependent part: a variety of chemical effects that affect the strength of the covalent bonding interaction are all accounted for in this term. Then for the fitting procedure, Brenner used solid state parameters of different carbon allotrops, hydrocarbon bond energies, and heats of formation of hydrocarbons.

Despite the efficiency of the REBO potential it turned out, however, that it is not appropriate, in its original form, for studying every hydrocarbon system. Since the potential is exclusively short-ranged, the absence of dispersion and non-bonded repulsion terms makes the potential poorly suited for any system with significant intermolecular interactions. This is the case for many important hydrocarbon systems, including liquids and thin films. Even covalent materials such as diamond can benefit from a treatment including non-bonded interactions. The bulk phase is dominated by covalent interactions, but longer-range forces become quite important when studying interfacial systems. In addition, the REBO potential also lacks a torsional potential for hindered rotation about single bonds.

To overcome these shortcomings, Stuart modified the Brenner potential by introducing non-bonded and torsional interactions through an adaptive treatment[56]. This new potential is referred to as the adaptive intermolecular REBO potential (AIREBO). In various cases, intermolecular interactions such as dispersion and short-range repulsion effects give rise to many of the properties of liquids, polymers and thin-film hydrocarbon materials. In the AIREBO force field the intermolecular interactions are modelled with a Lennard-Jones 12-6 potential (see Eq 3.33).

Because of the steep repulsive wall of the Lennard-Jones potential, however, it should be switched off very subtly at a certain distance depending on the chemical characteristics of the system in order to preserve the reactive nature of the potential.

Three criteria were chosen to determine whether, and at what distance, to switch off the LJ interaction. This decision is made adaptively, depending on: i) the distance separating the pair of atoms considered, ii) the strength of any bonding interaction between them, and iii) the network of bonds connecting them. The three criteria mentioned are represented in the following equation:

$$E_{ij}^{LJ} = S_{ij}^r S_{ij}^b C_{ij} U_{ij}^{LJ} + (1 - S_{ij}^r) C_{ij} U_{ij}^{LJ} \quad (3.41)$$

where the factor  $S_{ij}^r$  represents the distance criterion,  $S_{ij}^b$  accounts for bond order,  $C_{ij}$  reflects the connectivity switch, whereas  $U_{ij}^{LJ}$  is the Lennard-Jones potential defined in Eq 3.33.  $S^r$  and  $S^b$  are cubic spline functions while  $C$  is a cosine based switch function.

Unlike classical non-reactive potential, the reactive AIREBO potential allows the non-bonded interaction to be turned smoothly on or off as bonding configurations change. Usually, interactions between first (1–2), second (1–3) and third (1–4) neighbours are modelled very well, thus LJ interactions are not needed. In the AIREBO potential, however, they can be switched on smoothly through  $C_{ij}$  if the connection is via a series of partially dissociated bonds.

The other new component of the AIREBO potential is a term depending on dihedral angles. The original REBO potential lacked any torsional interactions about single bonds, representing its original focus on network solids, such as diamond and small molecular fragments relevant to the chemical vapour deposition of diamond. Without barrier of the rotation about single bonds the original REBO potential is unable to properly simulate saturated hydrocarbons larger than methane.

In a reactive potential, torsional energies and barriers must change as the molecule undergoes chemical reactions. Therefore, the symmetry of the torsional potential has to arise naturally from the local coordination environment. This is accomplished in AIREBO potential through the use of a torsional potential with a single minimum. This results, for example, in a threefold symmetry of the overall torsional potential when the torsional interactions are summed over the nine dihedral angles in a bond between identically substituted  $sp^3$  carbons.

With the adaptive treatment of dispersion, intermolecular repulsion, and torsional interactions the total energy of the system can be written in the following form:

$$E^{AIREBO} = E^{REBO} + E^{LJ} + E^{tors}. \quad (3.42)$$

This methodology presented above proved to be an efficient tool for treating both chemical reactivity and intermolecular interactions within the same system using a simple, empirical potential.

### 3.1.4 Technical details of simulations

In this section the technical problems concerning computer simulations will be overviewed to characterise them from a more practical point of view.

As a first step, we have to generate a configuration as the initial state of the simulation, i.e.,  $N$  particles have to be placed in the simulation cell. Usually, that means random placement, but it can also be a crystalline structure, or – in order to avoid errors attributed to numerical instabilities due to large initial repulsions – an existing equilibrium structure (at least for the solvent molecules) can be used. In the case of MD simulations, the initial velocities are set randomly according to the Maxwell-Boltzmann distribution.

In the first part of the simulation, different properties change rapidly, and the energy decreases. This transient part is called the equilibration period. After performing a simulation for a sufficient length of time, different state functions, such as the energy, start to fluctuate around a given value indicating that the system has reached the equilibrium. The following part of the simulation is called the production part, where the collection of configurations and calculation of properties are carried out.

Unfortunately, the capacity of computers does not allow us to use an arbitrary number of particles. Even nowadays with more powerful computers, although several millions of atoms can be simulated, it is still a problem that too many particles appear at the boundary of the simulation box, strongly influencing the simulation results with boundary effects because they experience a quite different environment from particles in the bulk phase. To highlight this problem, let us imagine 20000 atoms being in a cubic simulation cell: Even in this case nearly 20% of the atoms are at the faces of the box. To overcome this problem, periodic boundary conditions are used. This means that the simulation cell is replicated and shifted by its edge length in each direction of space, thus, it is surrounded by its own images producing an infinite lattice.

Although this technique introduces an artificial periodicity to the system, it eliminates boundary errors. For this purpose, the shape of the simulation box has to be capable of filling the space without overlaps or gaps. The most standard

shape is the cubic, rectangular or rhombic prism, but for specific purposes, rhombic dodecahedron or a truncated octahedron can also be used. The usage of the periodic boundary conditions is the same in every case, thus the calculations will be here demonstrated only in the simplest case of cubic simulation box.

The basis of the method is that the particles move the same way in the image boxes as in the central one, thus if one of the particles leaves the simulation box at one side, it enters the neighbour image box, and, at the same time, the image of this particle enters the central cell on the opposite side. This effect is visualised in Figure 3.2 in a two dimensional case.

To calculate the potential energy contribution of the shaded particle, only those particles (or images) are considered which are within the simulation box (or, due to technical reasons, within a sphere of a given radius  $R_{\text{cut}}$  inside the box) centred on this particle. This approximation, when just the nearest images of the particles are taken into account during the calculation, is called the minimum image convention.

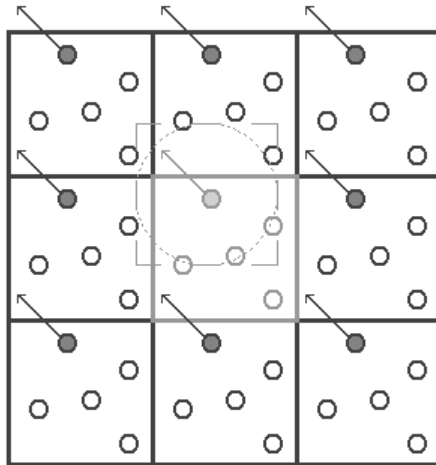


Figure 3.2: Central simulation cell, marked by gray and its images, drawn in black. The arrows show the movement of the shaded particle, leaving the central simulation cell. The circle demonstrates the interaction region of this particle.

In terms of the minimum image convention, all interactions are calculated within a finite region. Although the largest contribution to potential and forces comes from the neighbours close to the particle of interest, disregarding the long-range part of the interactions may cause an error. In the case of the Lennard-Jones interaction, this error is not important (although it can easily be corrected), as the function goes to zero fast, but in the case of Coulomb potential the interaction is significant even at long distances. Thus, ignoring the electrostatic interactions beyond the cut-off

value causes a substantial error. In order to avoid this, several correction methods were developed, from which the reaction field correction[57, 58] and the Ewald summations[59, 60] are the most commonly used. In the reaction field correction, it is assumed that any given molecule is surrounded by a spherical shell of finite radius ( $R_{\text{cut}}$ ), within which the electrostatic interactions are calculated explicitly. Outside the spherical shell the system is treated as a dielectric continuum. The Ewald summation methodology splits the calculation of the potential into a real space and a Fourier space summation. The advantage of this method is that it is able to take into account all particles and all their periodic images. This may, however, imply an artificial periodicity in the system (making the infinite system similar to a crystalline). The details of these long-range correction methods can be found in Appendix B.

## 3.2 Electronic structure calculations

If we are interested in the electronic structure of a system, or we want just to perform a more sophisticated calculation that does not disregard the electronic structure, the tools of quantum mechanics should be used. In quantum mechanics all systems consisting of elementary particles can be described by the Schrödinger equation. This equation takes the following form in the case of chemical systems, i.e., that consists only of electrons and nuclei:

$$\hat{H}(\mathbf{r}, \mathbf{R})\psi(\mathbf{r}, \mathbf{R}) = E(\mathbf{r}, \mathbf{R})\psi(\mathbf{r}, \mathbf{R}), \quad (3.43)$$

where  $\mathbf{r}$  is the coordinates of all electrons, while  $\mathbf{R}$  denotes those of all nuclei. The above equation is an eigenvalue equation: only those states of the system are possible that are the eigenstates (or eigenfunctions)  $\psi(\mathbf{r}, \mathbf{R})$  of the Hamiltonian operator  $\hat{H}$ . The eigenvalue  $E(\mathbf{r}, \mathbf{R})$  is just the total energy of the system corresponding to the given eigenstate. The Hamiltonian accounts for the description of the system: it contains the kinetic energy operator of the particles as well as all operators related to the interactions that the particles participate in.

Normally, all motions in the system are coupled to each other thus the motion of electrons cannot be separated from that of nuclei. In some cases, however, it is reasonable to do this separation by supposing that electronic motions do not affect nuclear motions. In this case the Hamiltonian takes the form of the sum of a purely electronic and nuclear part, while the wavefunction becomes the product of an electronic and nuclear wavefunction. This separation enables us to handle the electronic and nuclear problem separately. The electronic structure can be evaluated at any

given nuclear configuration. This approximation is the so-called Born-Oppenheimer approximation.

To solve the electronic Schrödinger equation, one has to look for the electronic wavefunction in an assumed form. In the simplest case, the correlation between the electrons is neglected, each electron is treated separately. This can be reflected in the Hartree product:

$$\psi^{Hartree} = \prod_{i=1}^N \varphi_i(i), \quad (3.44)$$

where  $i$  goes over all electrons  $N$ ,  $\varphi_i(i)$  denotes the  $i$ th one-electron orbital being occupied by the  $i$ th electron. For practical reasons, the system of  $N$  one-electron orbitals is often chosen to be orthonormalised. To fulfil the Pauli principle, the wavefunction has to be antisymmetric regarding the permutation of electrons. To accomplish this requirement, instead of the product, the determinant of the one-electron orbitals should be used:

$$\psi^{Slater} = \frac{1}{\sqrt{N!}} \begin{vmatrix} \varphi_1(1) & \varphi_2(1) & \dots & \varphi_N(1) \\ \varphi_1(2) & \varphi_2(2) & \dots & \varphi_N(2) \\ \vdots & \vdots & \ddots & \vdots \\ \varphi_1(N) & \varphi_2(N) & \dots & \varphi_N(N) \end{vmatrix}, \quad (3.45)$$

where  $\varphi_i(j)$  describes the  $i$ th orbital being occupied by the  $j$ th electron and  $1/\sqrt{N!}$  is a normalising factor. This determinant is often referred to as the Slater determinant. It can be shown that during the solution of the N-electron problem according to the variational theorem, a system of N one-electron equations, analogous to the Schrödinger equation, can be derived:

$$\hat{f}(i)\tilde{\varphi}_i = \epsilon_i\tilde{\varphi}_i, \quad \text{where } i = 1, \dots, N. \quad (3.46)$$

This equation is the canonical Hartree-Fock (HF) equation of the  $i$ th canonical orbital  $\tilde{\varphi}_i$  generated by the linear combination of the one-electron functions,  $\epsilon_i$  is the orbital energy, and  $\hat{f}(i)$  is the one-electron Fock operator that depends on the coordinates of only the  $i$ th electron explicitly. This equation looks like an eigenvalue equation, however, the Fock operator depends implicitly on the other electrons too as their coordinates are integrated out when reducing the N-electron operator to a one-electron one. The solution of Eq 3.46 is possible only in an iterative way starting from the set of guess one-electron functions (assumed not to be too far from the

canonical set). After the solution, the new set of functions is used to build up the new Fock operator. This procedure is repeated until convergence is obtained. Such a procedure creates an average self-consistent electrostatic field (SCF).

Usually, we look for the eigenfunctions of the above system of equations as linear combinations of some beforehand chosen basis functions:

$$\varphi_i = \sum_{a=1}^{N_b} c_a(i) \chi_a, \quad (3.47)$$

where  $a$  goes over the set of basis functions  $\chi_a$  containing  $N_b$  functions, and  $c_a(i)$  is the coefficient of  $\chi_a$  in the series of the  $i$ th orbital. With the use of this basis set, the Hartree-Fock equations can be converted to a matrix equation, thus transforming the problem to (iterative) matrix diagonalisation:

$$\mathbf{F}C_i = \epsilon_i \mathbf{S}C_i, \quad (3.48)$$

where  $C_i$  is the vector of all coefficients  $c_a(i)$ , one element of the Fock matrix  $\mathbf{F}$  can be written as  $F_{ab} = \int d\mathbf{x}_1 \chi_a^*(\mathbf{x}_1) \hat{f} \chi_b(\mathbf{x}_1)$  ( $\chi_a^*$  being the complex conjugate of the function  $\chi_a$  and  $\mathbf{x}_1$  being the coordinates of one electron), whereas one element of the overlap matrix  $\mathbf{S}$  can be written as  $S_{ab} = \int d\mathbf{x}_1 \chi_a^*(\mathbf{x}_1) \chi_b(\mathbf{x}_1)$ . The above equation is called the Hartree-Fock-Roothan equation.

Although the Hartree-Fock method is quite expressive because it supports our approach related to atomic orbitals, it cannot produce reliable and quantitative results on many systems. One can refine this method by taking into account the electron correlation effects but this entails the growth of the time need of these more sophisticated methods (e.g. MP, CI, CC methods). On the other hand, there are large systems for which even the Hartree-Fock method is not feasible due to the huge costs of the calculation. There exist less sophisticated methods for these systems where the computationally expensive terms are neglected or reasonably approximated, e.g., by empirical formulas and parameters adjusted to experimental measurements. These methods are called semi-empirical methods, in contrast to the purely theoretical *ab initio* methods.

### 3.2.1 The AM1 semi-empirical method

The development of semi-empirical methods started in the 1960's with the goal of making molecular orbital calculations possible for large, primarily organic systems. These methods use three main approximations as compared to the Hartree-Fock

method, namely they i) treat only the valence electrons explicitly ('frozen core approximation'), this means one  $s$  and three  $p$  orbitals for heavy atoms, ii) use minimal basis set, and iii) neglect the main fraction of expensive two-electron integrals and replace the rest with empirical parameters.

The most frequently used semi-empirical methods (AM1[61], MNDO[62], PM3[63]) are all based on the Neglect of Diatomic Differential Overlap (NDDO) integral approximation. This approach belongs to the class of Zero Differential Overlap methods, in which all two-electron integrals involving two-center charge distributions are neglected. The three above mentioned, most popular methods are parametrised in such a way that the calculated energies are expressed as heats of formation instead of total energies.

The methods based on the NDDO approximation use Slater type orbitals (STOs) to construct the basis set:

$$\chi(r, \Theta, \Phi) = Nr^{n-1}e^{-\zeta r}Y_l^m(\Theta, \Phi), \quad (3.49)$$

where  $N$  is a normalising factor,  $n$  is the principal quantum number ( $n = 1, 2, \dots$ ),  $\zeta$  is a fitted atomic parameter,  $Y_l^m(\Theta, \Phi)$  is a spherical harmonic function, while  $r$ ,  $\Theta$  and  $\Phi$  are a spatial and two angular coordinates respectively.

The following notation will be used for the two-electron integrals to facilitate the equations:

$$\langle zy|mn\rangle = \int \int d\mathbf{x}_1 d\mathbf{x}_2 \chi_z^*(1)\chi_y(1)\frac{1}{r_{12}}\chi_m^*(2)\chi_n(2), \quad (3.50)$$

where  $\chi_y(1)$  denotes atomic orbital  $y$  being occupied by electron 1,  $\mathbf{x}_1$  denotes the coordinates of electron 1,  $r_{12}$  is the distance between electron 1 and 2, and the asterisk refers to complex conjugation. In the NDDO approximation this integral differs from zero only if  $z$  and  $y$  are on the same atom and  $m$  and  $n$  are also on the same atom. Note that this integral is written using atomic units, i.e., the charge of one electron is set to unity.

The diagonal element of the Fock matrix is approximated as

$$F_{yy} = U_{yy} - \sum_{B \neq A} q_B \langle yy|s_B s_B\rangle + \sum_z^A P_{zz} \left( \langle yy|zz\rangle - \frac{1}{2} \langle yz|yz\rangle \right) + \sum_{B \neq A} \sum_p^B \sum_q^B P_{pq} \langle yy|pq\rangle, \quad (3.51)$$

where  $y$  and  $z$  are orbitals on atom  $A$  while  $p$  and  $q$  are orbitals on atom  $B$ . The first term represents the diagonal one-electron element (one-electron one-center term) of the Fock matrix and is approximated by atomic orbital constants (this is the energy that an electron would feel if all the other valence electrons were removed from the atom). The second term is the approximation of the interaction between orbital  $y$  (on atom  $A$ ) and the  $s$  type valence orbital ( $s_B$ ) on atom  $B$ .  $q_B$  denotes the core charge on atom  $B$  thus it equals the atomic number of  $B$  minus the number of core electrons.  $P_{zz}$  and  $P_{pq}$  are density matrix elements, and are defined for closed-shell systems as

$$P_{pq} = \sum_{j=1}^{N_{valence}} c_{pj}^* c_{qj}, \quad (3.52)$$

where  $c_{pj}$  is a coefficient of atomic orbital  $p$ .

There are two types of off-diagonal (two-center) elements in the Fock matrix. The elements in which the orbitals  $y$  and  $z$  are on the same atom are in the first group, and are labeled as  $F_{zy}^{AA}$ . The other type has the orbitals  $p$  and  $z$  on different atoms and is labeled as  $F_{zp}^{AB}$ :

$$F_{zy}^{AA} = - \sum_{B \neq A} q_B \langle zy | s_B s_B \rangle + \frac{1}{2} P_{zz} (3 \langle zy | zy \rangle - \langle zz | yy \rangle) + \sum_{B \neq A} \sum_p^B \sum_q^B P_{pq} \langle zy | pq \rangle, \quad (3.53)$$

and

$$F_{zp}^{AB} = \frac{1}{2} (\beta_z + \beta_p) S_{zp} - \frac{1}{2} \sum_y^A \sum_q^B P_{yq} \langle zy | pq \rangle, \quad (3.54)$$

where  $S_{zp}$  is an element of the overlap matrix, i.e., it is the overlap between atomic orbitals  $z$  and  $p$ . The parameters  $\beta_z$  and  $\beta_p$  are fitted atomic parameters.

The total energy of the system is the sum of the total valence electronic energy and the energy of repulsion between the cores on atoms  $A$  and  $B$ . This latter has to be corrected because only valence electrons are considered, and the core electrons are treated together with the nuclei through an effective core potential, and thus the simple point charge model used in the HF method to calculate the nuclear repulsion energies is inappropriate in semi-empirical calculations.

In the above equations, the one-center two-electron integrals ( $\langle yy|zz\rangle$  and  $\langle yz|yz\rangle$  in Eq 3.51 and Eq 3.53) are fitted to atomic spectroscopic data. These approximated integrals are used together with intermolecular distances in different molecules to compute the two-electron two-center integrals ( $\langle zy|pq\rangle$ ). Atomic parameters  $U_{yy}$ ,  $\beta_z$  and  $\beta_p$  are fitted to reproduce heats of formation, molecular geometries and dipole moments.

In the three NDDO methods the correction of the core-core repulsion energy is different. In the AM1 method the total core-core repulsion is written as

$$f_{AB} = q_a q_b \langle s_A s_A | s_B s_B \rangle \left( 1 + e^{-\alpha_A R_{AB}} + e^{-\alpha_B R_{AB}} \right) + \frac{q_a q_b}{R_{AB}} \left( \sum_k a_{kA} e^{-b_{kA} (R_{AB} - c_{kA})^2} + \sum_k a_{kB} e^{-b_{kB} (R_{AB} - c_{kB})^2} \right), \quad (3.55)$$

where  $R_{AB}$  is the internuclear distance between atom  $A$  and  $B$ ;  $\alpha$ ,  $a$ ,  $b$  and  $c$  are fitted atomic parameters. The first row of this equation represents the MNDO modification coming from the changing screening effects of nuclei at short distances. The second row is a further modification in the AM1 and PM3 method to reduce the excessive core-core repulsion just outside bonding distances. Note that for the O–H and N–H interaction the MNDO correction is slightly different.

In the AM1 method the atomic  $\zeta$  parameters for  $s$  and  $p$  type orbitals are not set equal contrary to the MNDO method. PM3 method treats the one-center two-electron integrals as parameters. The AM1 method contains 13 types of parameters from which 8 are fitted to experimental data.

The above presented semi-empirical methods have to be used with circumspection, although they are the most performing semi-empirical methods. They may be used preferentially only for large systems (with about 1000–10000 atoms) where the more accurate ab initio methods cannot be carried out. On one hand, these methods are not able to describe H-bonding accurately and, on the other hand, computational errors tend to be unsystematic in many cases. A critical area of application concerns calculations of nitrogen containing compounds because the inversion barriers of trivalent nitrogen are badly reproduced. This fact results in distortion of some N-containing structures. This is usually the case in simulating peptides: the structure of the amide group differs from the planar configuration. This error is the tiniest for the AM1 method but it makes, however, even this method poorly suited for the study of peptide conformations.

## Chapter 4

# Adsorption of VOCs on ice

### 4.1 Introduction

In Section 2.2 we have seen how VOCs influence the atmosphere. In this chapter we are interested in how they are adsorbed at the surface of ice: In what chemical potential range does the adsorption take place? What is the structure of the adsorption layer the VOC molecules are adsorbed in? Which are the most preferred adsorption positions and surface orientations? What is the strength of the interactions formed between ice and adsorbate molecules?

To shed light on these details a number of experimental studies have been carried out. Thus, the adsorption of acetone[64, 65, 66, 67, 68, 69, 70, 71], acetic acid[72, 73], formaldehyde[71], formic acid[73, 74], methanol[67, 71, 75], acetaldehyde[67] and 2,3-butanedione[68] on ice has been studied using either a Knudsen cell flow reactor or a coated-wall flow tube. These studies led to the conclusion that the interaction between VOCs and ice is of the simplest type, i.e., reversible physisorption, and the corresponding adsorption enthalpies are between  $-70$  and  $-50$  kJ mol<sup>-1</sup>, with the exception of formaldehyde, which exhibits very low affinity to the ice surface[71].

A growing number of theoretical studies have also recently been devoted to the characterisation of the details of the adsorption processes at the surface of ice, based either on ab initio calculations[76, 77, 78] or classical simulations[75, 79, 80, 81, 82, 83, 84, 85]. The main advantage of computer simulations in studying such problems comes from the fact that a large number of molecules can be treated, and the effect of the temperature can also be taken into account in the calculations. The grand canonical Monte Carlo method[41] is particularly suitable for such studies because, in this way, the entire adsorption isotherm can be calculated by varying the chemical

potential of the adsorbate molecule in a series of simulations.

The three VOCs (i.e. acetone, formic acid and benzaldehyde) studied in my work are expected to form quite complex interactions with the ice surface: All of them can participate in hydrogen bonding. Furthermore, the aromatic benzene ring of benzaldehyde provides an enhanced electronic density that may also interact with the strongly electronegative water O.

Formic acid seems to create the most complex interactions with ice compared to acetone and benzaldehyde due to the fact that formic acid can not only accept but also donate hydrogen in forming hydrogen bonds, whereas acetone and benzaldehyde can act only as an acceptor. Accurate study of the structure of formic acid – formic acid dimers has revealed that unusual C-H $\cdots$ O type hydrogen bonds may also be formed between formic acid molecules[86]. This type of H-bond was also found to be present in the liquid phase of formic acid[87].

#### 4.1.1 Common points in the numerical studies

##### 4.1.1.1 Common computational details

During my work, the same tools were used to analyse the adsorption behaviour of the three VOCs. In addition, the numerical starting points were also similar: The adsorption was studied at the surface of a hexagonal, proton-disordered ice. This ice phase contained 18 molecular layers, each of which consisting of 160 water molecules. The molecules belonging to the innermost two layers were kept fixed in the simulations, whereas the molecules of the outer layers were allowed to move. The  $X$ ,  $Y$ , and  $Z$  edges of the rectangular basic simulation box were 100.0, 35.926, and 38.891 Å long respectively. The ice surface was parallel to the  $YZ$  plane. Standard periodic boundary conditions were applied.

In every case a set of Monte Carlo simulations was performed on the grand canonical ensemble. The value of the chemical potential of the adsorbate was controlled through the  $B$  parameter of Adams defined in Eq 3.21. For performing the simulations we used the MMC[88] code of Mezei. During the simulations all interactions were truncated to zero beyond the centre-centre cut-off radius of 12.5 Å. Molecule displacement and adsorbate insertion/deletion attempts were done in an alternating order. In the particle displacement step, a randomly chosen molecule was translated to a random distance by no more than 0.25 Å, and randomly rotated around a randomly chosen space-fixed axis by the maximum angle of 15°. In an insertion/deletion attempt it was tried either, by 50 % probability, to remove a

randomly chosen adsorbate molecule from, or, also by 50 % probability, to insert an extra adsorbate molecule to the system. For inserting a molecule the cavity-biased method of Mezei[46, 47] was used (see Section 3.1.1.1). As an illustration, Figure 4.1 shows a side-view of our ice phase placed in the middle of the simulation box. The gas phase in our system is on the left and right side of this ice slab.

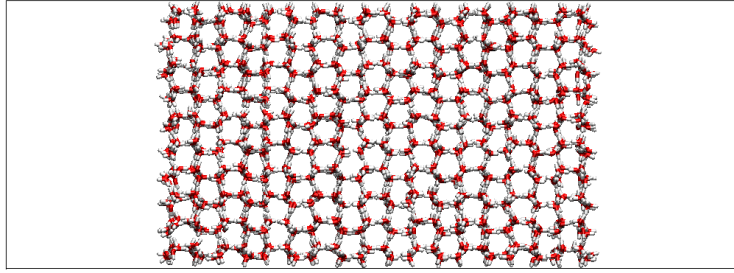


Figure 4.1: Side-view of our ice slab placed in the middle of the simulation box.

#### 4.1.1.2 Adsorption isotherms

The primary result of the simulation is the isotherm in the  $\langle N \rangle (B)$  form, i.e., the average number of particles as a function of the  $B$  value. Using the definition of the  $B$  parameter of Adams (see Eq 3.21) one can obtain the isotherm in the  $\langle N \rangle (\mu)$  form. This can be further converted into the more convenient and practical  $\Gamma(p_{rel})$  form, where  $\Gamma$  is the surface density of the adsorbed molecules, and  $p_{rel}$  is the relative pressure, i.e., the pressure of the vapour phase normalised by the pressure of the saturated vapour of the adsorbate. In cases the pressure is low enough so the ideal gas law is applicable,  $p_{rel}$  values can easily be calculated[89]. If the situation is beyond the applicability of the ideal gas law, a more complicated procedure should be followed to relate the chemical potential and the corresponding pressure. This procedure involves usually the application of equations of state. Appendix C shows an example for this case. In our study, however, at sufficiently low pressure the ideal gas law holds thus one can write[89]

$$p_{rel} = \frac{p}{p_0} = \frac{\exp B}{\exp B_0} = \frac{\exp \beta \mu}{\exp \beta \mu_0}, \quad (4.1)$$

where  $B_0$  and  $\mu_0$  are the  $B$  and  $\mu$  values, respectively, at which condensation occurs. The value of  $\Gamma$  can easily be given by the expression

$$\Gamma = \frac{\langle N \rangle}{2YZ}, \quad (4.2)$$

using the reasonable assumption that all the adsorbate molecules of the system are adsorbed at the surface, and considering the fact that the system contains two surfaces along the surface normal axis  $X$ . Since Eq 4.1 is only valid at the vapour phase, the  $\langle N \rangle (\mu)$  isotherm can only be converted into the  $\Gamma(p_{rel})$  form up to the point of condensation.

The obtained isotherms in the  $\Gamma(p_{rel})$  form can be adjusted using the Langmuir isotherm:

$$\Gamma(p_{rel}) = \Gamma_{max} \frac{p_{rel}K}{1 + p_{rel}K}, \quad (4.3)$$

where the parameters  $\Gamma_{max}$  and  $K$  are the saturated surface density and the partitioning coefficient between the solid and gas phase respectively. The Langmuir theory assumes that i) all the adsorption sites are equivalent at the surface; ii) the lateral interactions between the adsorbate molecules are negligible; and iii) no multilayer adsorption occurs. Another common choice in the analysis of the adsorption isotherm is to use the Brunauer-Emmett-Teller (BET) theory[90]:

$$\Gamma(p_{rel}) = \frac{\Gamma_{mono} p_{rel} C}{(1 - p_{rel}) [1 + p_{rel}(C - 1)]}, \quad (4.4)$$

where  $\Gamma_{mono}$  and  $C$  are the surface density of the saturated monolayer and the BET coefficient respectively. The BET theory differs from the Langmuir model by allowing multilayer adsorption, and hence it has to account for the interaction between consecutive adsorption layers. However, lateral interactions within a given layer are still neglected in this model. The  $C$  parameter is related to the energetics of the adsorption:

$$C = \exp\left(\frac{\Delta H_{out} - \Delta H_1}{RT}\right), \quad (4.5)$$

where  $\Delta H_1$  and  $\Delta H_{out}$  are the enthalpies of adsorption in the first and subsequent outer layers, respectively. The BET parameters  $\Gamma_{mono}$  and  $C$  are conventionally determined by fitting the linearised form of the BET isotherm:

$$\frac{p_{rel}}{\Gamma(1 - p_{rel})} = \frac{1}{\Gamma_{mono}C} + \frac{C - 1}{\Gamma_{mono}} p_{rel}. \quad (4.6)$$

In practice, the data can be fitted by a straight line only in the  $0.05 \leq p_{rel} \leq 0.35$  range, thus one also has to limit the fitting procedure to this range.

### 4.1.1.3 Density profiles

To analyse the ordering of the adsorbate molecules along the surface normal axis  $X$  one may calculate the number density profiles of the molecules. During the calculation of this profile the simulation box is divided virtually into thin slices along the surface normal axis  $X$ . In the collected configurations the number of the molecules falling in each slice is counted, which is then normalised by the number of configurations. The positions of the molecules are represented usually by that of their central atom.

### 4.1.1.4 Interaction energy distribution

In order to characterise the energetic background of the adsorption process in the simulation, the distribution of the total binding energy of the adsorbed molecules  $U^{TOT}$  (i.e., the interaction energy of a given adsorbate molecule with the rest of the system) can be calculated, as well as the contributions coming from the interactions with the ice phase  $U^{ice}$  and with the other admolecules  $U^{ac}$ ,  $U^{FA}$  and  $U^{BA}$  in the case of acetone, formic acid and benzaldehyde respectively.

### 4.1.1.5 Orientational analysis

The orientation of a rigid body relative to an external direction can be fully described by two independent orientational variables. Therefore, the orientational statistics of the molecules relative to a flat surface can only be given unambiguously by the bivariate joint distribution of two such variables[91, 92]. Jedlovszky and co-workers previously demonstrated that the polar angles  $\vartheta$  and  $\phi$  of the surface normal vector in a local Cartesian frame fixed to the individual molecules represent a suitable choice of these variables[91, 92].

Once the coordinate frame is defined in a reasonable way, the bivariate distribution functions can be calculated and plotted as maps using different tones to represent different values. It should be noted that  $\vartheta$  is the angle of two general spatial vectors, but  $\phi$  is formed by two vectors restricted to lie in a given plane by definition, and hence uncorrelated orientation of the molecules with the surface results in a uniform bivariate distribution only if  $\cos \vartheta$  and  $\phi$  are chosen as independent variables.

## 4.2 Adsorption of acetone

### 4.2.1 Computational details of the simulations

Although several different potential models were proposed to describe acetone[93, 94, 95, 96, 97], the majority of these models are unable to capture the mixing properties of acetone with water[98, 99]. However, adsorbate – adsorbent interactions may play a very important role in the adsorption, in particular, at low pressures, where the adsorbate – adsorbent interaction is the main driving force of the adsorption. For this purpose, we chose to use the four-site KBFF acetone model (where the methyl group is described by one single interaction site) of Weerasinghe and Smith[97], which was developed to reproduce various thermodynamic properties of acetone – water mixtures. By developing this model, Weerasinghe and Smith used the three-site SPC/E water potential[100] and therefore we also chose this model to describe the water molecules in our systems. The values of the used potential parameters are summarised in Table 4.1.

Molecule	Interaction site	$\sigma / \text{\AA}$	$\epsilon / \text{kJ mol}^{-1}$	$q / e$
Water	O	3.166	0.6506	-0.8476
	H	0.0	0.0	0.4238
Acetone	Me	3.748	0.8672	0.0
	C	3.360	0.3300	0.565
	O	3.100	0.5600	-0.565

Table 4.1: Interaction parameters of the water and acetone models used in our simulations. ‘Me’ denotes the single interaction site describing the whole methyl group.

Taking into account the long range part of the electrostatic interaction beyond the cut-off radius in such an inhomogeneous and anisotropic system is a non-trivial task. The application of the standard Ewald summation technique[41, 60] would lead to the simulation of an infinite stack of ice and vapour layers, whereas in using the method of reaction field correction[57, 58] one has to face the difficulty that the system is consisted of two phases of markedly different dielectric constants. In order to investigate the importance of the exact treatment of long range electrostatics we performed two series of simulations.

In the first set we used reaction field correction, setting the dielectric constant of the continuum,  $\epsilon_{RF}$ , beyond the cut-off sphere to infinity, whereas in the second set no long range correction was applied, i.e.,  $\epsilon_{RF}$  was set to unity. These two sets of simulations represent the limiting cases corresponding to the lower and upper estimates of the effect of long range electrostatics.

The simulations were performed at 28 different B values, ranging from  $-17$  to  $-5$ , which corresponds to the chemical potentials falling in the range between  $-51.12$  and  $-31.01$  kJ mol $^{-1}$ . The systems were equilibrated by performing  $10^8$  Monte Carlo steps, while the production stage was  $2 \times 10^8$  Monte Carlo steps long. In order to analyse the properties of the adsorption layer 2500 sample configurations, separated by  $8 \times 10^4$  Monte Carlo steps, were saved in four systems, characterised by the chemical potential values of  $-48.54$ ,  $-41.91$ ,  $-40.26$ , and  $-39.43$  kJ mol $^{-1}$ , respectively.

## 4.2.2 Results

### 4.2.2.1 Adsorption isotherm

The adsorption isotherms are shown in Figure 4.2 as obtained with and without applying reaction field correction. As is seen, the two isotherms are almost identical; the only difference is that the point of condensation occurs at a slightly lower chemical potential value if no long range correction is applied. Due to the observed insensitivity of the results to the exact treatment of the long range correction of the electrostatic interaction, in the following we only present the results obtained with a choice of  $\epsilon_{RF} = 1$ , unless otherwise indicated.

At the low  $\mu$  part the obtained isotherms exhibit an exponential increase up to the  $\mu$  value of about  $-47$  kJ mol $^{-1}$ . This part corresponds to the situation when the adsorptions of the individual acetone molecules are independent of each other. Above this chemical potential value the slope of the isotherm starts to increasingly deviate from the exponential form, however, this slope never approaches zero. In other words, the isotherm does not exhibit any nearly constant plateau below the point of condensation at about  $\mu = -40$  kJ mol $^{-1}$ . This behaviour of the isotherm indicates that the saturated adsorption monolayer is not of a particular stability.

The observed shape of the isotherm is in a clear contrast with what was observed previously either for methanol or for formaldehyde. Thus, the adsorption isotherm of formaldehyde on ice shows a nearly exponential increase up to the point of condensation, indicating the Langmuir-like behaviour of this system[85], whereas in the case of methanol the adsorption isotherm exhibits a clear plateau in a broad range of chemical potentials[75]. The adsorption isotherms of methanol and formaldehyde on ice are shown in the insets of Figure 4.2 for comparison. In this respect, the adsorption behaviour of acetone on ice is between those of formaldehyde and methanol.

To shed more light on the details of the adsorption process we converted the

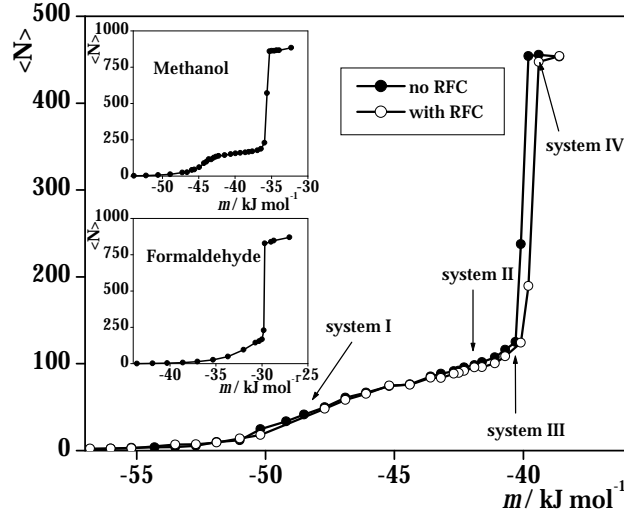


Figure 4.2: Simulated adsorption isotherms of acetone on ice. Full circles: simulations without reaction field correction, open circles: simulations applying reaction field correction with the choice of  $\epsilon_{RF} = \infty$ . The arrows indicate the systems that were chosen for further analyses. The upper and lower insets show the isotherms obtained previously for methanol[75] and formaldehyde[85], respectively.

obtained  $\langle N \rangle(\mu)$  curve to the  $\Gamma(p_{rel})$  form (see Eq 4.1 and 4.2). From the  $\langle N \rangle(\mu)$  isotherm we estimated the value of  $\mu_0$  to be  $-40.05 \text{ kJ mol}^{-1}$ . The obtained  $\Gamma(p_{rel})$  isotherm is shown in Figure 4.3. For comparison, the similar isotherms obtained previously for methanol[75] and formaldehyde[85] are indicated in the insets of Figure 4.3.

The deviation of the obtained  $\Gamma(p_{rel})$  isotherm from various experimental data sets[68, 71] remains in the same order as the reported deviation of the different experimental isotherms from each other. Nevertheless, the simulation underestimates the adsorption at low pressures. This is probably due to the fact that in the simulation a perfect ice surface was used, whereas in experimental situations the surface layer of ice can be defected and can also be subject to surface melting to an unknown extent. This view is also supported by the finding of Schaff and Roberts that amorphous ice can adsorb a considerably higher amount of acetone than crystalline ice[101, 102].

As is seen, the rapidly increasing part of the curve at low pressures is not followed by a saturation region; instead the isotherm exhibits a monotonous increase, indicating the non-Langmuir nature of this adsorption. Despite this, at low pressures, i.e., up to about the  $p_{rel}$  value of 0.07, the obtained  $\Gamma(p_{rel})$  curve can be well fitted by the Langmuir isotherm, as is seen in Figure 4.4. The values of  $\Gamma_{max}$  and  $K$  are summarised in Table 4.2 as resulted from this fitting.

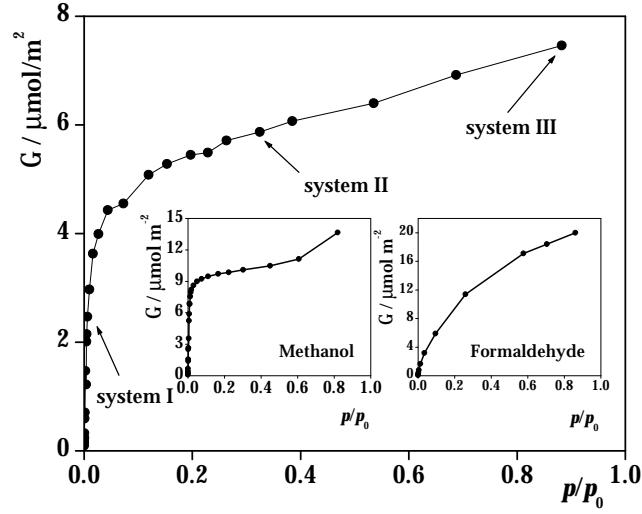


Figure 4.3: Adsorption isotherm (surface density vs. relative pressure) of acetone on ice, as obtained from the simulations. The arrows indicate the systems that were chosen for further analyses. The left and right insets show the isotherms obtained previously for methanol[75] and formaldehyde[85], respectively.

Although the validity of the assumptions of the Langmuir theory (see Section 4.1.1.2) is difficult to be checked in experimental situations, computer simulation methods provide a unique opportunity to test them. In the present case, the assumptions of the Langmuir theory are only valid up to the relative pressure value of about 0.07. As it will be discussed in detail later, above this pressure the lateral interactions between the adsorbed acetone molecules become increasingly important, and above  $p_{rel} \approx 0.5$  even multilayer adsorption occurs, as is evidenced by the increasing slope of the  $\Gamma(p_{rel})$  curve above this pressure.

In order to take into account the effect of this possible multilayer adsorption, we

Model	Parameter	Value
Langmuir	$\Gamma_{max}$	$(5.04 \pm 0.26) \mu\text{mol m}^{-2} = (3.02 \pm 0.16) \times 10^{14} \text{ cm}^{-2}$
	$K$	$148 \pm 22$
BET	$\Gamma_{mono}$	$(3.96 \pm 0.34) \mu\text{mol m}^{-2} = (2.38 \pm 0.20) \times 10^{14} \text{ cm}^{-2}$
	$C$	$0.985 \pm 0.16$
Simulation	$\Gamma_{mono}$	$(6.52 \pm 0.03) \mu\text{mol m}^{-2} = (3.91 \pm 0.02) \times 10^{14} \text{ cm}^{-2}$

Table 4.2: Parameters of the Langmuir and BET functions fitted to the calculated adsorption isotherm, and the monolayer capacity resulting directly from our simulations. Error bars correspond to the limits of the confidence interval of 95%.

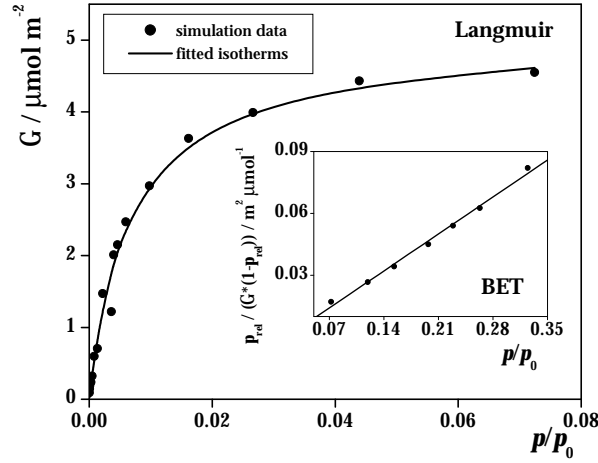


Figure 4.4: Langmuir fit (solid curve) to the points of the simulated isotherm (circles) up to the relative pressure of 0.07. The inset shows the BET fit (solid line) to these data (circles) up to  $p_{rel} = 0.35$ . The adjustments of the isotherms were done in the pressure ranges shown in the figure.

performed also the adjustment of the BET isotherm (see Eq 4.4) to the simulated data points. The result of this fitting is shown in the inset of Figure 4.4, whereas the  $\Gamma_{mono}$  and  $C$  values are included in Table 4.2.

Although the  $\Gamma_{max}$  parameter of the Langmuir isotherm has basically the same physical meaning as the  $\Gamma_{mono}$  value of the BET isotherm, the obtained  $\Gamma_{max}$  and  $\Gamma_{mono}$  values deviate largely, by 20–25% from each other (see Table 4.2). This finding again emphasizes the fact that the assumptions lying behind at least some of these functional forms are not valid for the system investigated here.

This point can be checked by determining the value of  $\Gamma_{mono}$  directly from the simulations (as explained in detail in the following section), and be compared with the fitted values. Since the  $\Gamma_{mono}$  value of  $6.52 \mu\text{mol m}^{-2}$  resulting directly from the simulation, is about 30 and 60% larger than the values estimated from the Langmuir and BET theories, respectively (see Table 4.2), the invalidity of an assumption that is behind both theories can be suspected. Considering the strongly dipolar character of the acetone molecule, the invalid assumption is likely the neglect of the lateral interactions. This point will be further analysed in the following subsections.

#### 4.2.2.2 Characterisation of the adsorption layers

In order to characterise the structural and energetic properties of the adsorption, four systems, corresponding to four markedly different points of the isotherm were

chosen for further analyses. System I, characterised by the chemical potential value of  $-48.54 \text{ kJ mol}^{-1}$  corresponds to the exponentially rising part of the  $\langle N \rangle(\mu)$  isotherm. This chemical potential range can be characterised by adsorbed acetone molecules being far enough from each other forming thus negligibly weak lateral interactions. System II, corresponding to the chemical potential value of  $-41.91 \text{ kJ mol}^{-1}$  is on the slowly rising part of the isotherm. Finally, systems III and IV, being at  $\mu = -40.26 \text{ kJ mol}^{-1}$  and  $\mu = -39.43 \text{ kJ mol}^{-1}$ , are slightly below and slightly above the point of condensation, respectively. The points representing these systems on the isotherms are marked by arrows in Figure 4.2 and 4.3.

**Density profiles.** In the calculation of density profiles the positions of the water and acetone molecules were represented by their central O and carbonyl C atom respectively. The resulting profiles of acetone, symmetrised over the two surfaces present in the basic simulation box, are shown in Figure 4.5 as obtained in the four systems. In addition, the density profiles of the water molecules are also shown as obtained in system I. It should be noted that the water profiles are found to be almost identical in each system analysed.

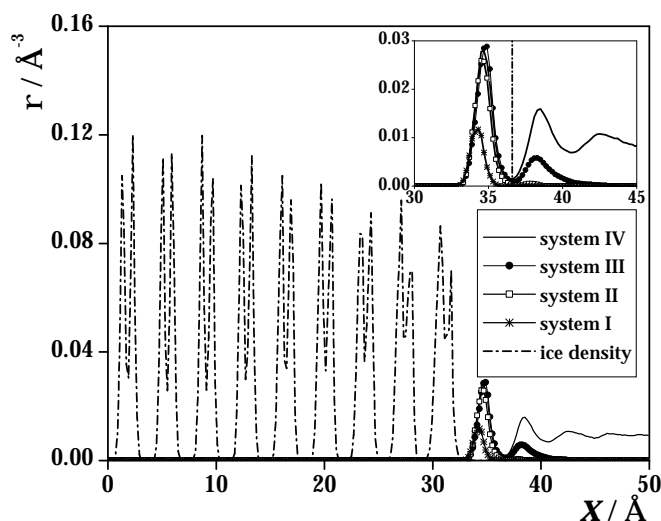


Figure 4.5: Number density profiles of the acetone molecules in systems I (asterisks), II (open squares), III (filled circles), and IV (solid line). The number density profile of the water molecules in system I is also indicated (dash-dotted line). The inset shows the acetone profiles on a magnified scale. The dashed vertical line indicates the boundary of the first molecular layer of adsorbed acetone.

The nine water peaks are followed by the density peak of the acetone molecules being in direct contact with the ice surface. Clearly, this first adsorption layer is highly unsaturated in system I, where the height of this density peak is about one

third of that in the other systems. In system II the adsorbed molecules form a nearly saturated monolayer at the ice surface, and traces of the second molecular layer can also be observed.

It is also seen that the peak corresponding to the first layer is not only higher but also broader here than in system I, indicating that upon saturation this layer also becomes thicker. In system III the second layer starts to be built up, the surface density of acetone in this layer is about 25% of that in the saturated first layer. Finally, system IV corresponds to condensed acetone, as the acetone density never drops to zero here.

The surface density of the saturated monolayer can easily be calculated from the density profile, by integrating the first peak in a system containing the saturated first layer, i.e., in system III or IV. The resulting value of  $6.52 \mu\text{mol m}^{-2}$  strongly deviates from the estimates obtained both from the Langmuir and the BET theory, as discussed in the previous subsection. The reasons of this deviation are discussed in detail in the following subsections.

**Distribution of the distances between water and acetone molecules.** To characterise the structure of the first adsorption layer we calculated the distribution of the distances of the acetone oxygens from the nearest water O and H atoms in systems I–IV. Note that here we took into account only the acetone molecules belonging to the first adsorption layer. The obtained distributions, normalised to the average number of the adsorbed molecules in the first layer, are plotted in Figure 4.6.

Both of these functions are bimodal in systems II–IV, having a sharp and high peak at low distances (i.e., at 2.83 and 1.80 Å in the case of  $\text{O}_{\text{ac}}\text{--O}_{\text{wat}}$  and  $\text{O}_{\text{ac}}\text{--H}_{\text{wat}}$  distributions, respectively), which is followed by a broader second peak of a much smaller height at larger distances. This second peak is, however, missing in system I. Between these two peaks the distributions drop to zero, which allows us to make an unambiguous distinction between the acetone molecules that give rise to the different peaks. The positions of the first peaks correspond to the hydrogen bonding O–O and O–H distances. This means that some of the adsorbed acetone molecules are hydrogen bonded to the ice surface, whilst at higher surface coverage some others are oriented away from the surface by their carbonyl group.

The separate integration of the two peaks reveals that in systems II–IV 73–76 acetone molecules are hydrogen bonded to the ice surface, and in system II 21, whereas in systems III and IV 34 non-hydrogen bonded acetone molecules belong to the first adsorption layer. This finding indicates that upon saturation the acetone molecules occupy the hydrogen bonding positions first, and the non-hydrogen bond-

ing positions start to be taken only afterwards. It is also seen that both distributions are almost identical in systems III and IV, indicating that once the first adsorption layer is completed, its structure is independent of the saturation of the outer layers.

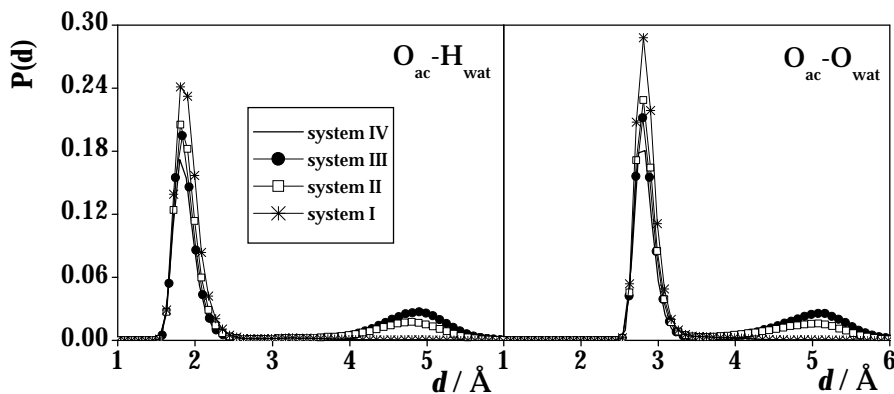


Figure 4.6: Distribution of the distance of the acetone O atom belonging to the first molecular layer from the nearest water O atom (top), and water H atom (bottom). Data corresponding to systems I–IV are marked by asterisks, open squares, filled circles, and solid lines, respectively.

**Energetics of the adsorption.** Energy distributions introduced in Section 4.1.1.4 were also calculated in the four systems analysed. The distributions of  $U^{TOT}$ ,  $U^{ac}$  and  $U^{ice}$  are presented in Figure 4.7. As is seen, the total binding energy distribution shifts to lower energies upon increasing the chemical potential of acetone. Thus, in system I the  $P(U^{TOT})$  distribution is peaked at  $-55.7 \text{ kJ mol}^{-1}$ , whereas in system IV this peak appears at  $-82.2 \text{ kJ mol}^{-1}$ . This shift is related to the increasing number of acetone molecules, and indicates that at high surface coverage acetone – acetone interactions contribute at least as much to the thermodynamic driving force of the adsorption as acetone – ice interactions.

Not surprisingly, the evolution of the  $P(U^{ac})$  distribution with the acetone chemical potential shows a rather similar picture. Thus, in system I this distribution is peaked at  $-3.5 \text{ kJ mol}^{-1}$ , indicating that here the adsorbate – adsorbate interactions are still almost negligible. This confirms the validity of the assumption that in this range the Langmuir theory still holds. The increasing amount of the acetone molecules leads evidently to the increase of the acetone – acetone interactions. Thus, in system IV the peak of the  $P(U^{ac})$  distribution appears at  $-47.7 \text{ kJ mol}^{-1}$ . A similar binding energy value was obtained previously in liquid acetone using a different

potential model[95].

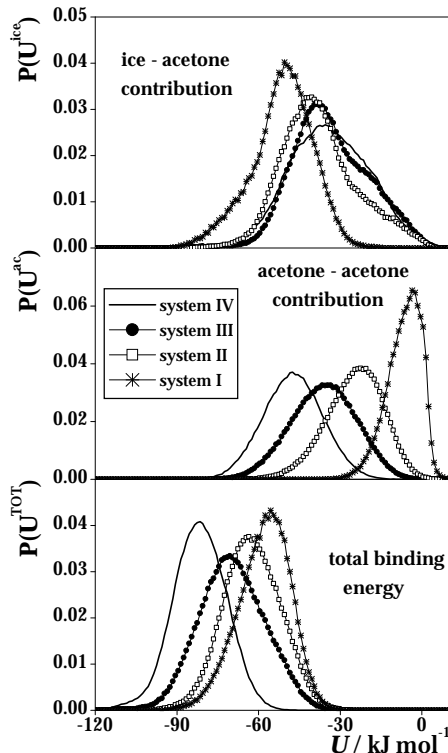


Figure 4.7: Distribution of the binding energy (bottom) of the adsorbed acetone molecules and that of the contributions coming from the interaction with the other adsorbed molecules (middle), and with the ice phase (top). Data corresponding to systems I–IV are marked by asterisks, open squares, filled circles and solid lines, respectively.

Quite a different picture is seen when the ice – acetone energy contribution is analysed. At low surface coverage (system I) the unimodal  $P(U^{ice})$  distribution is peaked at  $-50.6 \text{ kJ mol}^{-1}$  indicating that the adsorbed acetone molecules form two hydrogen bonds with the surface waters. The mean value of  $-51.4 \text{ kJ mol}^{-1}$  of this distribution can be compared to the experimental heat of the adsorption  $\Delta_0 H^{ads}$ , which is usually determined at very low surface coverages, where the lateral interactions are negligible, and hence  $\Delta_0 H^{ads}$  does not depend on the surface coverage yet. The values of  $\Delta_0 H^{ads}$  are collected in Table 4.3 as obtained in a number of recent experimental studies. The clear agreement between the simulated and experimental values confirms our results, and validates the choice of the used potential models.

Upon increasing the acetone surface density the peak of the  $P(U^{ice})$  curve gradually shifts to higher (i.e., lower in magnitude) values, up to about  $-35 \text{ kJ mol}^{-1}$ ,

$T / \text{K}$	$\Delta_0 H^{ads} / \text{kJ mol}^{-1}$	Method	Ref.
200	$-51.4 \pm 1.3$	Our study	
198 – 223	$-46 \pm 7$	Coated wall flow tube	[71]
193 – 223	$-48.1 \pm 3.1$	Coated wall flow tube / Langmuir	[68]
	$-50.3 \pm 2.5$	Coated wall flow tube / BET	
205 – 243	$-54.4 \pm 7.6$	Chromatography	[65]
193 – 213	$-55 \pm 7$	Volumetric	[64]
190 – 220	$-49 \pm 3$	Coated wall flow tube / Ic ice	[69]
	$-32 \pm 6$	Coated wall flow tube / Ih ice	
198 – 223	$-52 \pm 2$	Chromatography	[66]
190 – 223	$-43.7 \pm 7.9$	Coated wall flow tube	[103]

Table 4.3: Heat of the adsorption of acetone on ice, as resulted from the present work and from previous experimental studies.

indicating that in systems of higher surface coverage the majority of the acetone molecules form only one hydrogen bond with the ice surface. Further, these distributions exhibit two shoulders, at both sides of the main peak. The shoulder located around  $-50 \text{ kJ mol}^{-1}$  is given by the acetone molecules that are double hydrogen bonded to the ice phase.

The high energy side shoulder, located at about  $-20 \text{ kJ mol}^{-1}$ , clearly becomes more pronounced with increasing surface coverage. This shoulder can be attributed to non-H-bonding acetone molecules belonging to the first adsorption layer, as discussed in the previous subsection. To demonstrate this, in system III we also calculated the  $P(U^{ice})$  distribution separately for the acetone molecules that give rise to the first, and for those giving rise to the second peak of  $P(d_{O_{ac}-O_{wat}})$  (see Figure 4.8).

As is seen, the peak of the hydrogen bonded acetones appears at about the same position than the peak of  $P(U^{ice})$  in system III (i.e., at  $-40.3 \text{ kJ mol}^{-1}$ ), whereas that of the non-hydrogen bonded acetones is at  $-18.7 \text{ kJ mol}^{-1}$ . This relatively strong interaction of the non-hydrogen bonded acetone molecules with ice is probably due to the electrostatic interaction of the large dipole moment of the acetone molecule with the charge distribution of the ice phase.

**Orientation of adsorbed molecules.** In our study the local coordinate frame fixed to the acetone molecules is defined in the following way. The origin is located at the carbonyl C atom; the  $z$  axis lies along the dipole vector of the acetone molecule pointing from the O to the carbonyl C, the  $x$  axis is the molecular normal axis, and

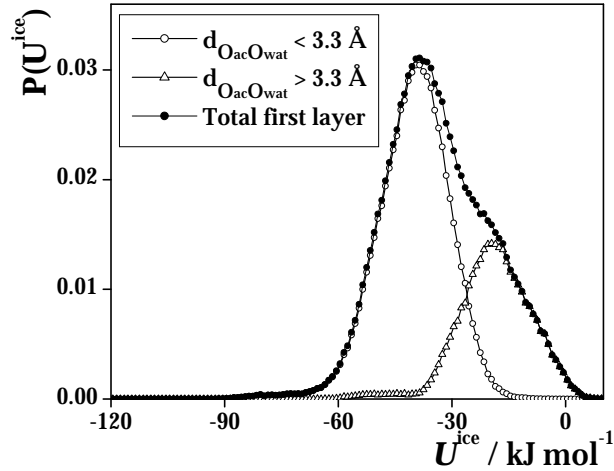


Figure 4.8: Interaction energy distribution of an adsorbed acetone molecule of the first molecular layer with the ice phase in system III, considering only the molecules whose O atom is closer to the nearest water O than 3.3 Å (open circles), and those molecules whose O atom is farther from the nearest water O atom than 3.3 Å (open triangles). The same distribution of all acetone molecules is also indicated (full circles).

the  $y$  axis is perpendicular of the above two axes. Thus,  $\vartheta$  is the angle between the interface normal vector pointing away from the ice phase  $\underline{X}$  and the molecular dipole vector.

The definition of this local Cartesian frame and of the polar angles  $\vartheta$  and  $\phi$  is demonstrated in Figure 4.9. It should be noted that, due to the definition of this frame and the symmetry of the molecule, the orientational distribution can be fully described by restricting us only to the  $0^\circ \leq \vartheta \leq 180^\circ$  and  $0^\circ \leq \phi \leq 90^\circ$  ranges.

The bivariate  $P(\cos \vartheta, \phi)$  orientational distributions of the adsorbed molecules are plotted in Figure 4.10 as obtained in the first and second molecular layers of the four systems studied.

In system I the acetone molecules have only one preferred orientation, which is denoted here by A. This orientation is characterised by the  $\cos \vartheta$  and  $\phi$  values of 0.3 and  $0^\circ$ , respectively. In this orientation, the acetone molecule is slightly tilted, pointing to the ice surface with the O atom, while the two methyl groups are at equal distance from the ice surface.

At higher surface coverage (system II) another orientation, corresponding to  $\cos \vartheta = 0.55$  and  $\phi = 90^\circ$  also becomes preferred. In this orientation, marked with B, the main symmetry axis of the molecule is slightly more tilted than in orientation

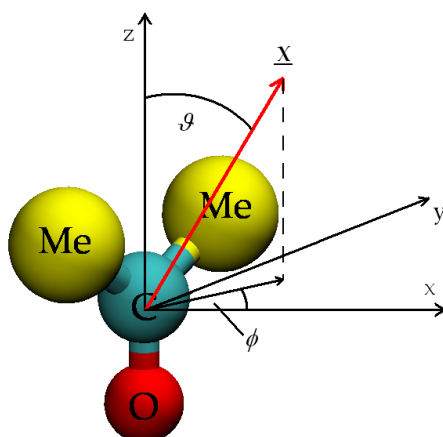


Figure 4.9: Definition of the local Cartesian frame fixed to the individual acetone molecules, and of the polar angles  $\vartheta$  and  $\phi$  describing the orientation of the surface normal vector  $\underline{X}$  pointing away from the ice phase.

A, and the molecular plane is now perpendicular to the ice surface.

Finally, in systems III and IV when acetone molecules have acetone neighbours also in the second layer a third orientation corresponding to the  $\cos \vartheta$  value of  $-1$  emerges. In this orientation, denoted here as C, the acetone molecule is perpendicular to the ice surface, pointing by its O atom away from the ice phase.

It is also seen that in the second layer of system III the molecules only prefer orientations A and B. It should be noted that very similar orientational preferences were observed at the surface of liquid acetone[104]. On the other hand, in system IV, where the second layer is followed by other acetone layers, orientation C is also clearly preferred in the second layer. The orientations A, B and C, preferred by the acetone molecules in the different systems are illustrated in Figure 4.11.

The physical background of these orientational preferences can be understood by considering the four possible orientations of the water molecules (see Figure 4.11) at the surface layer of the ice phase. In two of these orientations (i.e., 1 and 4) the water molecule points flatly to the vapour phase by one or two of its O–H bonds, whereas in orientation 2 one of the O–H bonds sticks straight to the vapour phase.

Thus, an adsorbed acetone molecule of orientation A can form two hydrogen bonds with the surface waters of either orientation 1 or 4, whereas in orientation B an acetone molecule can accept one hydrogen bond from a surface water of orientation 2. These possible hydrogen bonding patterns are illustrated in Figure 4.12.

It should be noted that orientations A and B can be related to the  $\beta$  acetones, while orientation C to the  $\alpha$  acetone molecules of Schaff and Roberts[102], who studied the desorption of acetone from ice by Fourier transform infrared reflection-

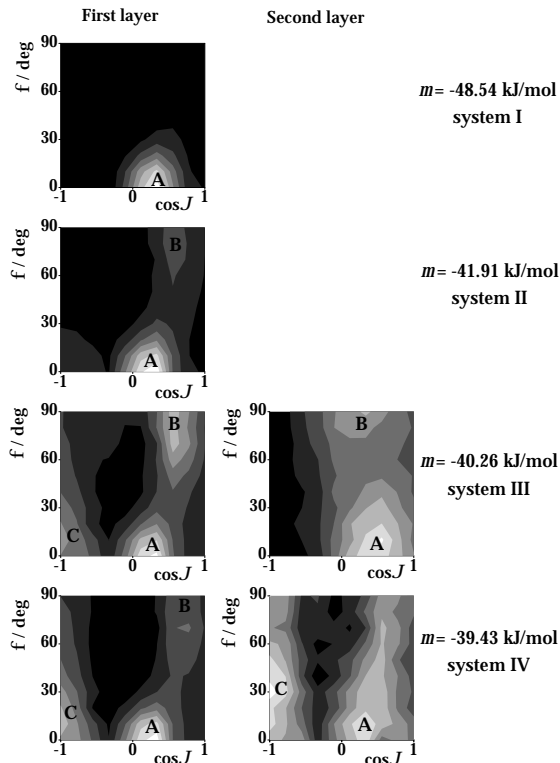


Figure 4.10: Orientational maps of the adsorbed acetone molecules belonging to the first (left column) and second (right column) molecular layer relative to the ice surface in systems I–IV (from the top to the bottom). The peaks corresponding to the different preferred acetone orientations are marked with A–C. Lighter shades of grey indicate higher probabilities.

absorption (FTIR–RA) spectroscopy. Similar distinction was made by Mitlin and Leung between ‘dangling acetone–OH complexes’ (orientations A and B) and ‘van der Waals complexes’ (orientation C) by FTIR–RA spectroscopic measurements[105].

Orientation A was also observed by Marinelli and Allouche at defected ice surface by ab initio calculations[106]. Further, orientations analogous to A and B were also observed in the adsorption layer of formaldehyde on ice, but with considerably smaller adsorption energies[85]. This difference in the adsorption energies of formaldehyde and acetone was also observed in experimental studies[71].

In the light of the analyses carried out, we can now give a possible scenario of the adsorption of acetone molecules at the ice surface. Thus, in system I, at low surface coverage, the adsorbed molecules are in orientation A, and form two hydrogen bonds with the ice phase. Up to the completion of the adsorption sites where acetone molecules can be bound in this orientation (i.e., up to the  $p_{rel} \approx$

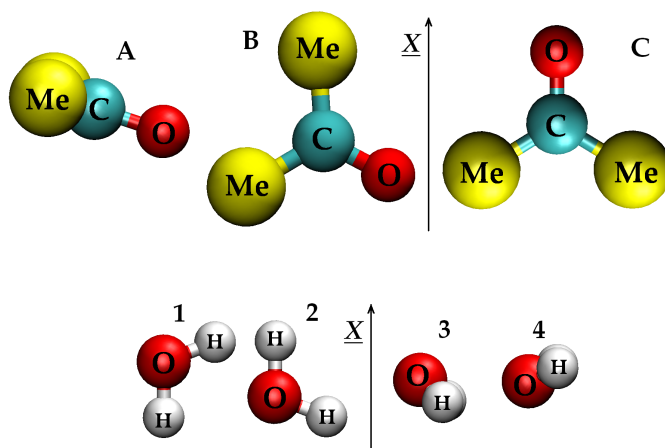


Figure 4.11: Illustration of the preferred orientations of the acetone molecules adsorbed at the ice surface (top row) and surface water molecules (bottom row) relative to the surface normal  $\underline{X}$  pointing away from the ice phase.

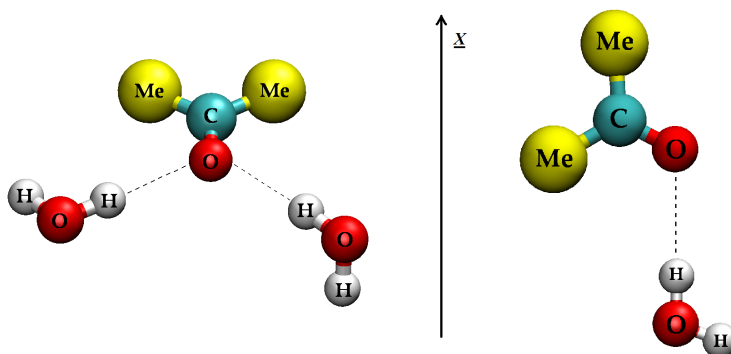


Figure 4.12: Possible hydrogen bonding patterns between the adsorbed acetone molecules of the first molecular layer and surface water molecules of the ice phase ( $\underline{X}$  being the surface normal vector).

0.07) the adsorption isotherm exhibits Langmuir behaviour as the adsorption sites are equivalent, and the lateral interactions are negligible.

Further, the  $\Gamma_{max}$  value obtained from the Langmuir fit at low pressure might be interpreted as the maximum surface density of acetones being in orientation A. The obtained  $5.04 \mu\text{mol m}^{-2}$  value is in agreement with the experimental value of  $(4.5 \pm 1.2) \mu\text{mol m}^{-2}$  [71]. As the surface density increases, new orientations occupying less surface area become preferred resulting thus in the calculated surface density of  $6.52 \mu\text{mol m}^{-2}$  in the saturated first adsorption layer.

Furthermore, the second peak of the  $P(d_{O_{ac}-O_{wat}})$  and  $P(d_{O_{ac}-H_{wat}})$  distributions (see Figure 4.6) can be clearly attributed to the acetone molecules of orientation C. To demonstrate this we calculated the  $P(\cos \vartheta, \phi)$  orientational map

separately for acetone molecules giving rise to the first, and for those giving rise to the second peak of  $P(d_{O_{ac}-O_{wat}})$  in the first layer of system III. These maps, shown in Figure 4.13, indicates that the molecules contributing to the second peak of  $P(d_{O_{ac}-O_{wat}})$  (and also to the shoulder of  $P(U^{ice})$  at about  $-18 \text{ kJ mol}^{-1}$  see Figure 4.8) are in orientation C, whereas the other molecules are either in orientation A or B.

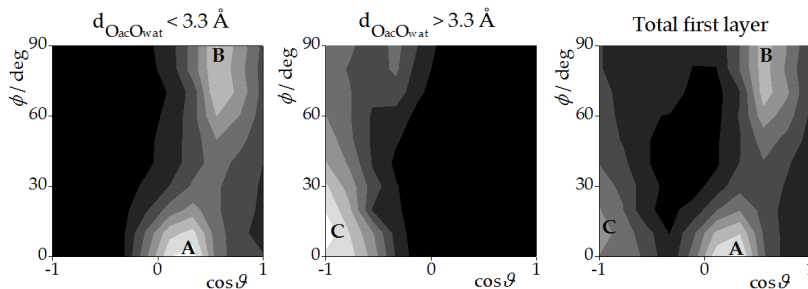


Figure 4.13: Orientational map of the acetone molecules whose O atom is closer to the nearest water O than  $3.3 \text{ \AA}$  (left), and of those being farther from the nearest water O atom than  $3.3 \text{ \AA}$  (middle) as is calculated in the first layer of system III. The same distribution of the entire first layer (right) is also shown.

The molecules in orientation C seem to appear after the second layer started to be build up, as we have seen from the density profiles. These molecules are likely to optimise their interaction with the molecules being in the second layer. This is supported by the fact that orientation C appears only if at least traces of the second layer are also present.

## 4.3 Adsorption of formic acid

### 4.3.1 Computational details of the simulations

Simulations were performed with 36 different  $B$  values, ranging from  $-24$  to  $-4$ , which corresponds to the chemical potential range of  $-68.10$  to  $-34.85 \text{ kJ mol}^{-1}$  at  $200 \text{ K}$ . Water and formic acid molecules were described by the TIP5P model[108] and by the rigid five-site Jedlovszky–Turi potential model[107], respectively. In accordance with the original parametrisation of the TIP5P water model[108], and with the results obtained for acetone, no long-range correction was applied.

The systems were equilibrated by performing  $10^8$  Monte Carlo steps (including both particle displacement and insertion/deletion attempts). The number of the

adsorbed molecules was averaged over  $2 \times 10^8$  equilibrium configurations at each  $B$  value. According to the features of the adsorption isotherm, five systems were selected for more detailed analysis. In these systems, 2500 sample configurations, separated by  $8 \times 10^4$  Monte Carlo steps each, were saved.

## 4.3.2 Results

### 4.3.2.1 Adsorption isotherm

The calculated  $\langle N \rangle(\mu)$  isotherm obtained from the simulation is shown in Figure 4.14. At low  $\mu$  values, the isotherm exhibits an exponential increase, indicating that the adsorption of the individual molecules takes place independently of each other. Then, around the  $\mu$  value of about  $-57 \text{ kJ mol}^{-1}$ , the slope of the isotherm starts to decrease, leading to the appearance of a plateau region. Here the adsorption layer is close to be saturated. In this respect, this isotherm is rather similar to what was previously obtained for methanol[75] as opposed to that of formaldehyde[85] and acetone (see Section 4.2).

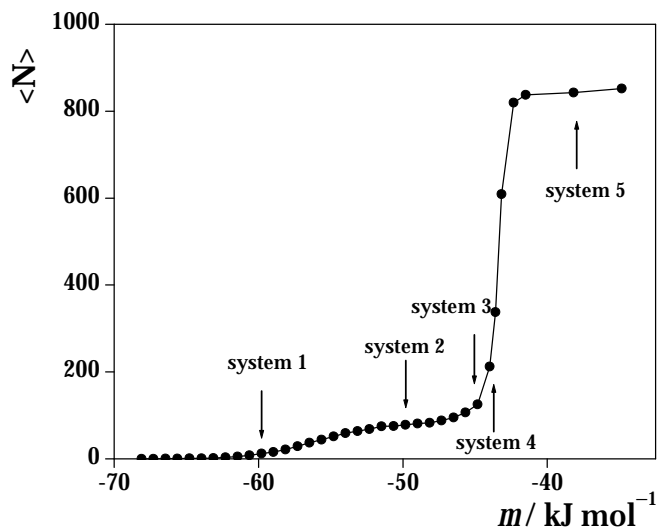


Figure 4.14: Average number of formic acid molecules in the basic simulation box as a function of the formic acid chemical potential. The systems analysed in detail are indicated by the arrows.

Between about  $-45$  and  $-42 \text{ kJ mol}^{-1}$ , the slope of the isotherm rapidly increases again. This feature can be related to the point of condensation, as above the  $\mu$  value of  $-42 \text{ kJ mol}^{-1}$ , the system contains the liquid phase of formic acid. However, the  $\mu$  range within which the condensation occurs is surprisingly broad. In fact,

condensation is a first-order phase transition, and hence at the boiling (condensation) point it is accompanied by an infinitesimally small change of the chemical potential.

This finding clearly suggests that in this chemical potential range, multilayer adsorption occurs, i.e., besides the first molecular layer, further layers of formic acid are adsorbed at the ice surface, while the bulk phase of formic acid is still vapour. In interpreting this result, it should be noted that the real width of the chemical potential range corresponding to multilayer adsorption is probably even broader than what is obtained in the simulation since it is likely to be underestimated due to the finite size of the basic simulation box. Namely, in the presence of three to four layers of adsorbed formic acid, the adsorption layers at the two ice surfaces in the basic box become too close to each other, and hence, their interaction with each other is no longer negligible, which can lead to the disappearance of the vapour phase between them.

Our numerical study was carried out jointly with the experimental investigation of the group of John N. Crowley[109]. Their results are compared to ours in the next subsections.

**Comparison of the simulated and experimental isotherms.** In order to make the simulated isotherm directly comparable with the experimental curve we converted the primary isotherm to the  $\Gamma(p_{rel})$  form. Here, we estimated the value of  $B_0$  to be  $-9.25$  corresponding to  $\mu_0 = -43.58 \text{ kJ mol}^{-1}$ . However, the real value of  $B_0$  might be slightly larger because of the aforementioned possible underestimation of the condensation point. For making a comparison between the experimental and simulation data, the experimental curves were also converted to the  $\Gamma(p_{rel})$  form. The experimental  $p_0$  value was estimated by the Antoine equation:

$$\log_{10} p_0 = a - \frac{b}{T + c}, \quad (4.7)$$

using the parameters of formic acid of  $a = 2.00121$ ,  $b = 515 \text{ K}$  and  $c = -139.408 \text{ K}$  [110]. The comparison of the isotherms simulated at 200 K and measured at 197 K is shown in Figure 4.15. As is seen, the rapid linear increase of both the simulated and measured isotherms is followed by the continuous increase, of a slighter slope, of the adsorbed quantity in the entire  $p_{rel}$  range. The simulation somewhat overestimates the amount of the adsorbed molecules, however, the deviation from the experimental curve never exceeds about 30–40%. This deviation can, at least partly, be attributed to the improper detection of the point of condensation in the simulation due to finite size effects, as discussed earlier.

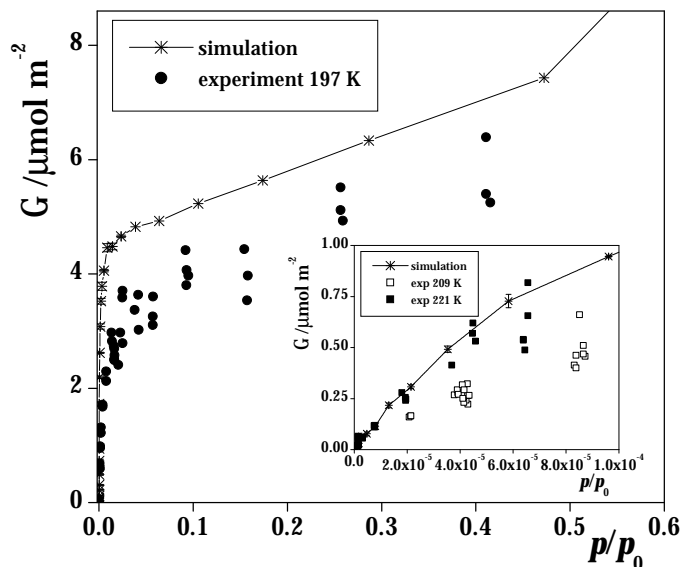


Figure 4.15: Comparison of the adsorption isotherm of formic acid on ice as obtained from the simulations at 200 K (asterisks) and from the flow tube measurements at 197 K (filled circles)[109]. The inset shows the very low pressure part of the adsorption isotherm as obtained from the simulations (asterisks) and from the flow tube measurements at 209 (open squares) and 221 K (filled squares). Error bars are shown whenever they are larger than the symbols.

In order to further investigate the origin of this deviation, we also compared the simulated data with the experimental isotherms measured at somewhat higher temperatures (i.e., at 209 and 221 K) but only up to considerably lower  $p_{rel}$  values than at 197 K. This comparison is shown in the inset of Figure 4.15. As is seen, the amount of the adsorbed molecules at a given  $p_{rel}$  value is higher at higher temperatures, and the simulation results agree very well with the experimental data measured at 221 K.

This deviation can be, at least partly, explained by the error in the Antoine parameters used, since these parameters were measured at considerably higher temperatures [110]. Further, such a shift is not surprising since the water and formic acid potential models used were optimised to reproduce the properties of the respective neat liquid phases rather than the interaction of these molecules with each other[107, 108]. In light of this consideration, the agreement of the simulated and experimental isotherms can be regarded as satisfactory.

**Langmuir and BET analyses.** The  $\Gamma(p_{rel})$  isotherms obtained both by computer simulations and by experimental methods clearly show non-Langmuir behaviour since at large  $p_{rel}$  values they still increase noticeably instead of exhibiting

a nearly constant plateau (Figure 4.15).

In order to understand the origin of the constant increase of the obtained isotherms, we fitted the Langmuir isotherm to the obtained simulation and experimental data sets below  $p_{rel} = 0.04$ . The result of this fitting, shown in Figure 4.16 indicates that in this pressure range the obtained isotherms can satisfactorily be described in terms of the Langmuir model.

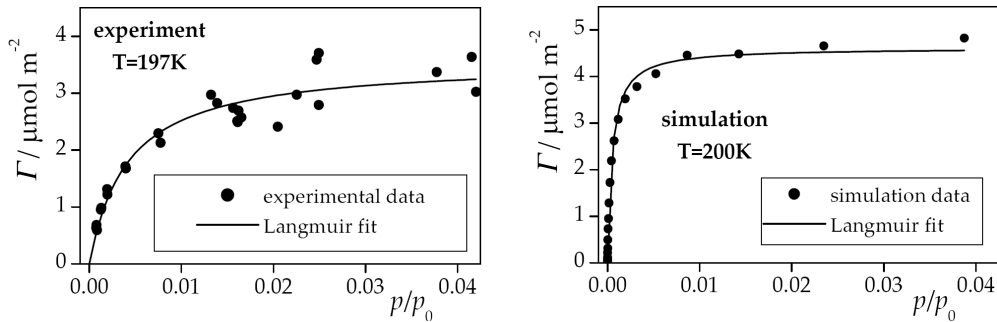


Figure 4.16: Langmuir fit (solid curves) of the points of the obtained isotherms (filled circles) up to the relative pressure of 0.04. Left: experimental isotherm, measured at 197 K; right: isotherm obtained from the simulations at 200 K.

The Langmuir fit was repeated by gradually increasing the  $p_{rel}$  range considered. However, in this case the agreement of the data points and the fitted function worsened considerably, indicating that the Langmuir behaviour of the isotherm breaks down above  $p_{rel} = 0.04$ . This finding can be interpreted in the following way. Below  $p_{rel} = 0.04$ , formic acid molecules occupy a certain type of adsorption site, denoted here as  $\alpha$  sites. Bonding to these sites is probably accompanied by a large (i.e., strongly negative) adsorption energy, since the binding of the formic acid molecules to these sites precedes that to other adsorption sites.

Further increase of the pressure leads to the gradual saturation of the first adsorption layer, as the formic acid molecules occupy now the non- $\alpha$  sites in this layer. Saturation of the first adsorption layer occurs at about  $p_{rel} = 0.5$ , and above this pressure outer adsorption layers are built up. The value of the Langmuir partitioning coefficient  $K$  is found to be rather high when fitting the simulation data set below the relative pressure value of  $p_{rel} = 0.04$ , i.e.,  $2070 \pm 140$ . This value agrees excellently with the experimental data of  $K_{exp} = 2095 \pm 205$ , obtained at 209 K, indicating again the small temperature shift. The surface density of the system in which all  $\alpha$  sites are saturated (i.e., the  $\Gamma_{max}$  parameter) is found to be  $(4.52 \pm 0.07) \mu\text{mol m}^{-2}$  in the simulations, which somewhat overestimates the experimental value of  $(3.65 \pm 0.83) \mu\text{mol m}^{-2}$ .

To analyse the possibility of the multilayer adsorption the fit of the BET isotherm was also performed to the simulation data as well as to the experimental values at 187, 197 and 209 K, as is shown in Figure 4.17. As is seen, the simulated data set lies somewhat below the experimental one obtained at 197 K; however, it agrees well with that measured at 209 K (see the inset of Figure 4.17), indicating again the temperature shift of the simulated properties.

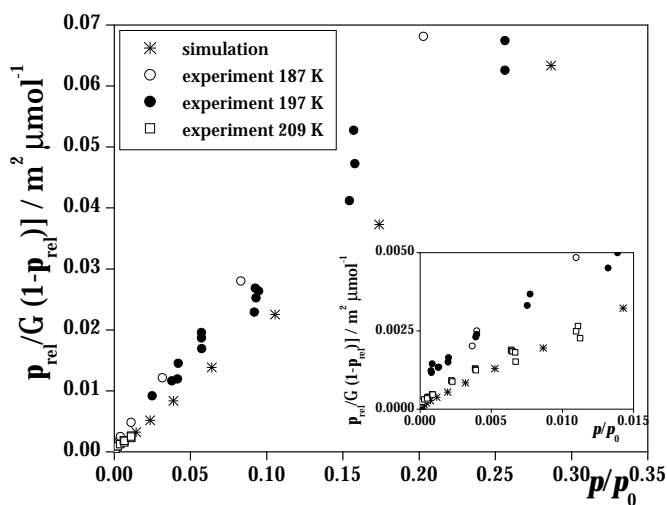


Figure 4.17: Points of the isotherms obtained by simulation at 200 K (asterisks) and by flow tube measurements at 187 (open circles), 197 (filled circles), and 209 K (open squares), shown in the linearised form of the BET isotherm. The inset enlarges the data corresponding to very low pressures.

The value of the  $\Gamma_{mono}$  parameter is in a good agreement with the  $\Gamma_{max}$  value of the Langmuir isotherm, being  $(4.68 \pm 0.01) \mu\text{mol m}^{-2}$  in the case of the simulated data, while the experimental values scatter between 3.9 and  $4.5 \mu\text{mol m}^{-2}$  depending on the temperature. It should be noted that, similarly to  $\Gamma_{max}$ , the  $\Gamma_{mono}$  value also reflects the saturation of the  $\alpha$  sites, since the molecules occupy the  $\alpha$  sites first, and hence the non- $\alpha$  sites of the first molecular layer are considered to be in an outer layer from the point of view of the BET theory.

The difference of the adsorption enthalpies corresponding to the  $\alpha$  sites and to all other sites resulted in  $(12.3 \pm 0.8 \text{ kJ mol}^{-1})$  from the simulation, again in a reasonable agreement with the experimental data, which scatters between 7.2 and  $12.2 \text{ kJ mol}^{-1}$  at the different temperatures.

### 4.3.2.2 Characterisation of the adsorption layers

**Density profiles.** Detailed analyses were performed on 5 sets of sample configurations corresponding to 5 different  $\mu$  values. Thus system 1, characterised by the chemical potential value of  $-59.79 \text{ kJ mol}^{-1}$  corresponds to the case when even the  $\alpha$  type adsorption sites are not saturated. System 2, being at  $\mu = -49.81 \text{ kJ mol}^{-1}$ ,  $p_{rel} = 0.0235$  falls into the range where Langmuir theory still holds. In this system,  $\alpha$  sites are almost completely saturated. System 3 corresponds to the point where the steepness of the  $\Gamma(p_{rel})$  isotherm suddenly increases ( $\mu = -44.83 \text{ kJ mol}^{-1}$ ,  $p_{rel} = 0.472$ ). Thus, in this system, the first adsorption layer is saturated, but multilayer adsorption does not occur yet. System 4 is at  $\mu = -43.99 \text{ kJ mol}^{-1}$ , i.e., still below the condensation point. This system is characterised by more than one adsorption layer. Finally, system 5 at  $\mu = -38.17 \text{ kJ mol}^{-1}$  corresponds to condensed formic acid. The molecular number density profiles computed in these five systems are shown in Figure 4.18. The number density profile of the water molecules is also indicated, as obtained in system 1.

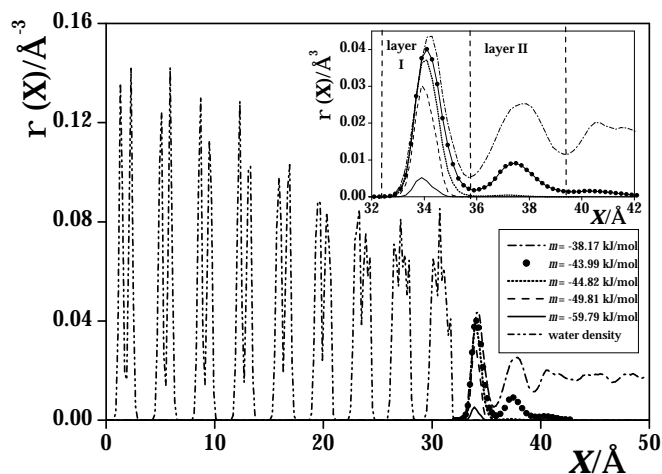


Figure 4.18: Number density profiles of the formic acid molecules in systems 1 (solid lines), 2 (dashed lines), 3 (dotted lines), 4 (filled circles), and 5 (dash-dotted lines). The number density profile of the water molecules in system 1 is also indicated (dash-dot-dotted line). The inset shows the formic acid density profiles on a magnified scale. The dashed vertical lines indicate the border of the first and second molecular layers of formic acid.

The formic acid density profiles are consistent with the picture suggested by the behaviour of the isotherm. Thus, in systems 1–3, the formic acid molecules are all attached to the surface of ice, forming a monomolecular layer. The density

profile obtained in system 2 is considerably higher than that of system 1; however, it occurs exactly at the same position confirming that upon going from system 1 to system 2 the same type of adsorption sites are occupied. However, when moving from system 2 to system 3, the density peak of the adsorbed molecules becomes higher and broader and it is also shifted somewhat toward the gas phase. This fact supports our assumption that above  $p_{rel} = 0.04$  an other type of adsorption site starts to be occupied than below this value. In system 4, a second and also a third molecular layer of the adsorbed molecules appear. The fact that the first density peak in this system agrees well with that in system 3 confirms that the first molecular layer is indeed almost fully saturated in system 3. Finally, in system 5, the simulation box is entirely filled with formic acid, indicating that this system is already above the condensation point.

**Energetics of the Adsorption.** The three types of interaction energy distribution presented in Section 4.1.1.4 were calculated in the five systems analysed. The distributions obtained in systems 1–3 as well as those in the first and in the second adsorption layer of system 4 are shown in Figure 4.19.

The  $P(U^{TOT})$  distributions obtained in systems 1 and 2 are very similar to each other. In particular, they appear at the same position, suggesting that the lateral interactions between the adsorbed molecules are rather weak. This is confirmed by the  $P(U^{FA})$  distributions of the two systems, as the peak of this distribution appears very close to zero in both cases. Upon further saturation the peak of the total binding energy distribution gradually shifts to lower energies due to the increasing lateral interactions. The  $P(U^{TOT})$  distributions obtained in the first and second layers of system 4 are rather close to each other; the mean binding energy value is  $-78.4 \text{ kJ mol}^{-1}$  in the first and  $-72.3 \text{ kJ mol}^{-1}$  in the second layer.

The distributions of the  $P(U^{ice})$  and  $P(U^{FA})$  contributions to the total binding energy show a more detailed picture. Thus, in systems 1 and 2, the  $P(U^{ice})$  distribution is unimodal, having its peak at very low energies, between  $-61$  and  $-64 \text{ kJ mol}^{-1}$ , indicating that formic acid molecules form two exceptionally strong hydrogen bonds with the ice surface at the  $\alpha$  positions. These values are also in a reasonable agreement with the experimental value of the heat of adsorption of  $(-54 \pm 8) \text{ kJ mol}^{-1}$ , determined from the temperature dependence of the isotherm in very low pressure range[109].

Upon increasing the surface coverage, another peak of  $P(U^{ice})$  appears at considerably higher energies, i.e., around  $-20 \text{ kJ mol}^{-1}$ . The bimodal shape of  $P(U^{ice})$  in systems 3 and 4 is in accordance with our former conclusion that the saturation of the  $\alpha$  sites is followed by further saturation of the first molecular layer by occupying

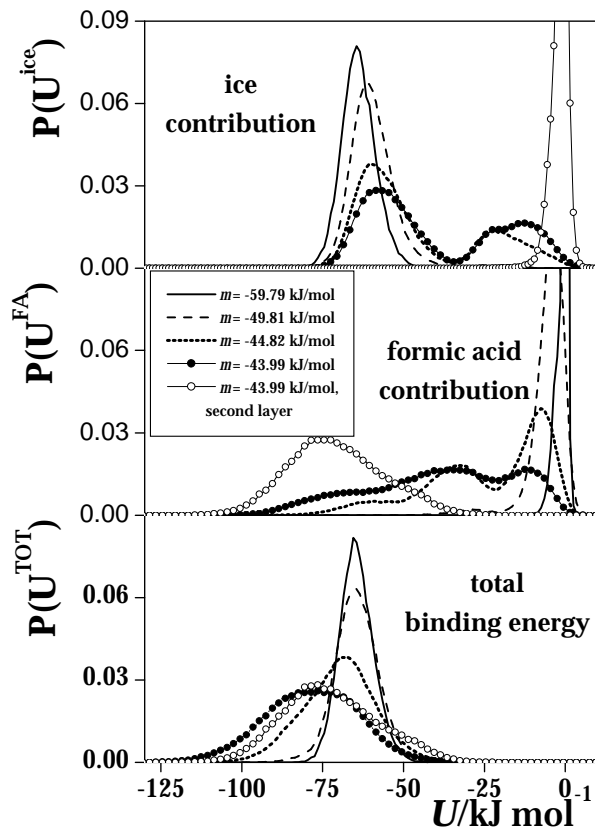


Figure 4.19: Distribution of the binding energy of the adsorbed formic acid molecules and the contributions coming from the formic acid – formic acid interaction (middle panel) and from the formic acid – ice interaction (top panel). Solid lines: system 1; dashed lines: system 2; dotted lines: system 3; filled circles: first molecular layer of system 4; open circles: second molecular layer of system 4.

other (non- $\alpha$ ) sites. The position of this second peak of  $P(U^{ice})$  indicates that at these sites, the adsorbed formic acid molecules cannot form more than one hydrogen bond, and this hydrogen bond is weaker than those formed at  $\alpha$  positions.

However, this weak binding of the adsorbed molecules at non- $\alpha$  positions is accompanied by rather strong lateral interactions between these molecules. Thus, the  $P(U^{FA})$  distribution in system 3 as well as that in the first layer of system 4 is trimodal. The peak closest to zero can be associated with the molecules being at  $\alpha$  positions since these molecules do not have strong (hydrogen-bonding) interactions with their neighbours. The second peak, located at about  $-33 \text{ kJ mol}^{-1}$ , is given by the molecules that form only one strong (O-H $\cdots$ O type) hydrogen bond with other formic acids. The unusual broadness of this peak suggests that some of these molecules probably also form a weak C-H $\cdots$ O type hydrogen bond with another formic

acid molecule. Finally, the peak located at the lowest energies is clearly given by the molecules that form two strong, O-H $\cdots$ O type hydrogen bond with their neighbours.

It is also seen that in the second layer of system 4, the  $P(U^{FA})$  distribution is again unimodal, having its peak at about  $-75 \text{ kJ mol}^{-1}$ , indicating that in the second layer, the majority of the formic acid molecules maintain two strong O-H $\cdots$ O type hydrogen bonds with their neighbours, probably by forming pairs of cyclic hydrogen-bonded dimers. This finding is also in accordance both with the former computer simulation result of Picaud and co-workers[79] and with the experimental finding of Bahr and Kempter[111] on the adsorption of acetic acid on ice, namely that acetic acid molecules form dimers above the saturation of the first molecular layer on the ice surface.

**Surface Orientation of the Adsorbed Molecules.** To characterise the orientational preferences of the formic acid molecules we defined the Cartesian frame in the following way. Its  $x$  axis lies along the C-H bond of the molecule, pointing from the H to the C atom, axis  $z$  is the molecular normal axis, whereas axis  $y$  is perpendicular to the above two. It should be noted that, due to the planar structure of the formic acid molecule, axis  $z$  of the local frame can always be directed in such a way that angle  $\vartheta$  is less than  $90^\circ$ . The definition of this local Cartesian frame and that of the polar angles  $\vartheta$  and  $\phi$  is illustrated in Figure 4.20.

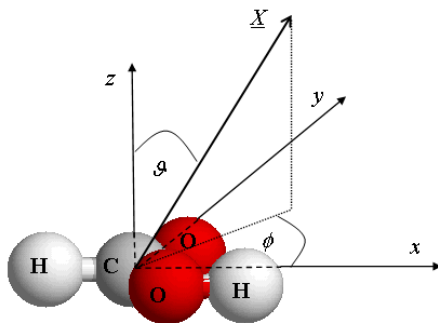


Figure 4.20: Definition of the local Cartesian frame fixed to the individual formic acid molecules and of the polar angles  $\vartheta$  and  $\phi$  describing the orientation of the surface normal vector pointing to the vapour phase  $\underline{X}$  in this frame.

The  $P(\cos \vartheta, \phi)$  orientation maps of the adsorbed formic acid molecules in systems 1–3 as well as those in the first and in the second layer of systems 4 and 5 are shown in Figure 4.21. As is seen, in systems 1 and 2, the formic acid molecules prefer the orientation characterised by  $\cos \vartheta = 0$  and  $\phi = 180^\circ$ .

This orientation, illustrated in Figure 4.22, will be referred to here as orientation I. In this orientation, the plane of the molecule is perpendicular to the ice surface

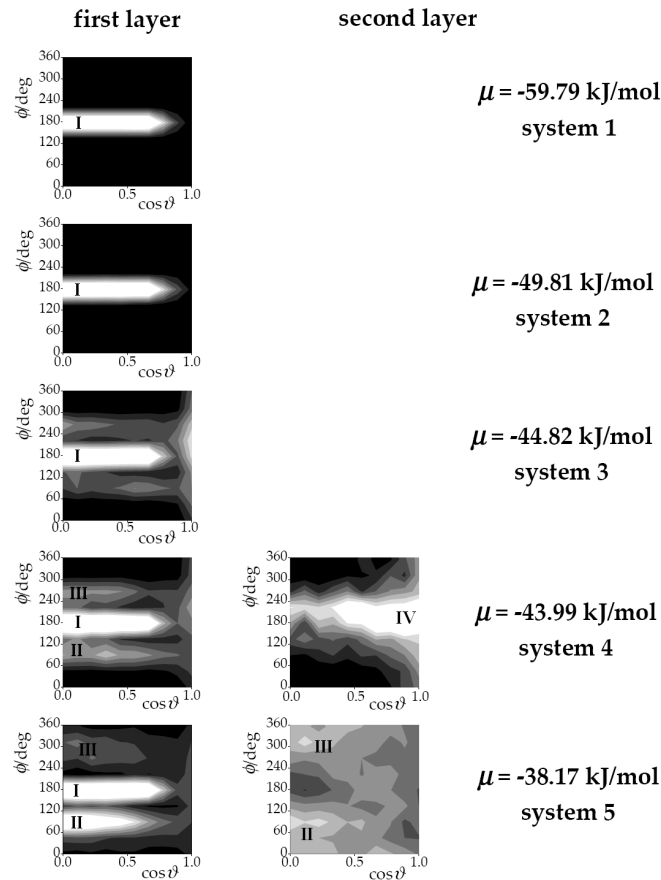


Figure 4.21: Orientational maps of the formic acid molecules of the first (first column) and second molecular layer (second column) at the ice surface in systems 1 (top row), 2 (second row), 3 (third row), 4 (fourth row), and 5 (bottom row). Lighter colours indicate higher probabilities. The peaks corresponding to preferred formic acid orientations relative to the ice surface are marked by I–IV.

(as reflected in the zero value of  $\cos \vartheta$ ), and the two O atoms point to the ice, whereas the non-acidic H points to the vapour phase. Considering the fact that the water molecules have four different orientations at the surface of Ih ice (see Figure 4.11), the preference of the formic acid molecules for orientation I at low surface coverages can easily be explained. Thus, in orientation I, a formic acid molecule can form two strong hydrogen bonds with the surface waters, one by donating its acidic H to a water molecule being in orientation 3, and the other one by accepting a dangling H of a water of orientation 2.

It should be noted that this relative orientation of formic acid and water molecules is also preferred in a cluster formed by one formic acid and two water molecules, as shown by Wei et al. from ab initio calculations (see Figure 1 of Ref. [112]). On the basis of this finding we can now specify the  $\alpha$  type adsorption sites, which are thus

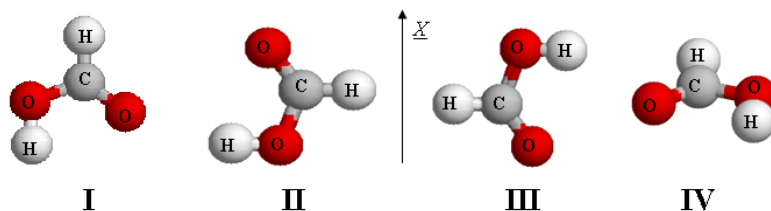


Figure 4.22: Preferred orientations of the formic acid molecules belonging to the first molecular layer at the surface of ice.  $\underline{X}$  is the surface normal vector pointing away from the ice phase. The C, O, and H atoms are shown by gray, red, and white colours, respectively.

characterised by two neighbouring surface waters being in orientation 2 and 3. The hydrogen-bonding scheme of the formic acid molecules at the  $\alpha$  type adsorption sites is illustrated in Figure 4.23a.

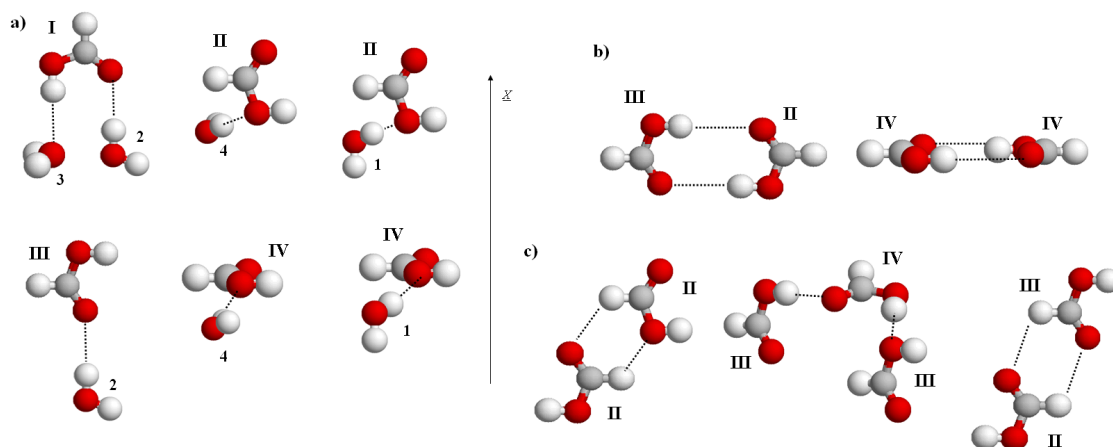


Figure 4.23: Possible hydrogen bonding patterns between (a) an adsorbed formic acid molecule in the first molecular layer and surface waters, (b) two adsorbed formic acid molecules belonging to the same molecular layer, and (c) two or three adsorbed formic acid molecules belonging to two consecutive molecular layers, if the molecules are aligned in one of their preferred orientations.  $\underline{X}$  is the surface normal. The C, O, and H atoms are shown by gray, red, and white colours, respectively.

The  $P(\cos \vartheta, \phi)$  orientation maps of systems 3–5 show that after the saturation of the  $\alpha$  type sites formic acid molecules are adsorbed at the ice surface in three different, new orientations. These orientations are denoted as II, III, and IV. Both orientations II and III correspond to the  $\cos \vartheta$  value of 0, i.e., the plane of the molecule is also perpendicular to the ice surface. The value of  $\phi$  in orientation II is about  $90^\circ$ , whereas in orientation III, it is  $270^\circ$ . This means that the acidic OH group is located at the vapour phase side of the molecule in orientation III and at the ice

phase side in orientation II, while the O-H bond is almost parallel with the surface. Finally, orientation IV corresponds to the  $\cos \vartheta$  value of 1, i.e., when the molecule lies parallel with the ice surface. Orientations II, III, and IV are also illustrated in Figure 4.22.

Considering also the possible orientations of the surface water molecules, it is seen that a formic acid molecule in orientation II or IV can form a hydrogen bond with a water molecule in either orientation 1 or 4. The H atom donated by the water molecule is accepted in both cases by one of the lone pairs of the hydroxyl O atom of the formic acid. Further, a hydrogen bond between the carbonyl O of a formic acid in orientation III and a dangling H of a water of orientation 2 can also be formed. These possible water – formic acid hydrogen bonds are illustrated in Figure 4.23a.

It should also be noted that a formic acid molecule in orientation II and another one in orientation III as well as two formic acid molecules in orientation IV can form a cyclic, double H-bonded dimer with each other. In these dimers, both of the hydrogen bonds are formed between the carboxylic O and the acidic H of the other molecule. These possible hydrogen-bonding patterns between two formic acid molecules within the same adsorption layer are shown in Figure 4.23b.

Analysing the orientation of the formic acid molecules in the second adsorption layer it is seen (Figure 4.21) that in system 4 the dominant orientation is clearly IV, however, in the case of condensed formic acid (system 5), orientations II and III dominate, whereas orientation IV completely disappears. Further, in the first layer of systems 4 and 5 only a weak trace of orientation IV can be observed. Clearly, a molecule of orientation IV in the second layer can form two O-H...O type hydrogen bonds with two molecules of orientation III of the first layer, one accepting and the other one donating the hydrogen (see Figure 4.23c). Further, a molecule of the second layer being in either orientation II or III can form a cyclic dimer with a molecule of orientation II of the first layer by two C-H...O type hydrogen bonds. Both of these dimer arrangements, shown in Figure 4.23c, correspond to a local minimum of the formic acid dimer energy surface[107]. Obviously, a formic acid molecule in orientation II and another one in orientation III as well as two molecules in orientation IV can form cyclic, double O-H...O bonded dimers also within the second layer.

Now we can understand why orientation IV is not preferred in the inner layers just only in the outmost one. Although a molecule being in orientation IV can form two strong O-H...O type H-bonds with formic acids of the previous layer, the gradual completion of the adsorption layers does not favour such a lying orientation as opposed to orientations occupying smaller area. On the other hand, molecules

in orientation II and III can be H-bonded both to the layer beyond and beneath, whereas a formic acid in orientation IV can only bind to the previous layer.

## 4.4 Adsorption of benzaldehyde

### 4.4.1 Computational details of the simulations

In modelling the adsorption of benzaldehyde on ice, a series of 29 grand canonical Monte Carlo simulations was performed in the  $\mu$  range between  $-70.31$  and  $-60.66$  kJ mol $^{-1}$  at  $T = 233$  K. Water molecules were described by the rigid five-site TIP5P potential[108], whereas benzaldehyde was modelled by the OPLS force field[113] using the charge distribution calculated by Canneaux et al[114]. In accordance with the original parametrisation of the TIP5P water model[108], and with the results obtained for acetone, no long-range correction was applied.

The systems were equilibrated by performing  $100 - 500 \times 10^6$  Monte Carlo steps. The number of benzaldehyde molecules in the system was then averaged over  $300 - 400 \times 10^6$  equilibrium configurations. Finally, at selected chemical potential values 2000 sample configurations, separated from each other by  $10^5$  Monte Carlo steps each, were saved for detailed analyses.

### 4.4.2 Results

#### 4.4.2.1 Adsorption isotherm

The calculated adsorption isotherm is shown in Figure 4.24 in the  $\langle N \rangle(\mu)$  form. As is seen, at low chemical potentials it shows an exponential increase up to the  $\mu$  value of about  $-62$  kJ mol $^{-1}$ . The exponential increase of the isotherm indicates that the adsorption of an individual molecule at the ice surface is independent from the presence or absence of other adsorbed benzaldehyde molecules. Then, in the chemical potential range between  $-62.0$  and  $-61.1$  kJ mol $^{-1}$  the isotherm exhibits a saturation plateau, where the surface density of the benzaldehyde molecules is about  $6.7 \mu\text{mol m}^{-2}$ . This plateau corresponds to the presence of a particularly stable adsorption layer.

Properties of this stable layer are analysed in detail in a following section. Finally, between the  $\mu$  values of  $-61.1$  and  $-61.05$  kJ mol $^{-1}$  condensation of benzaldehyde occurs; above this chemical potential the system contains liquid benzaldehyde.

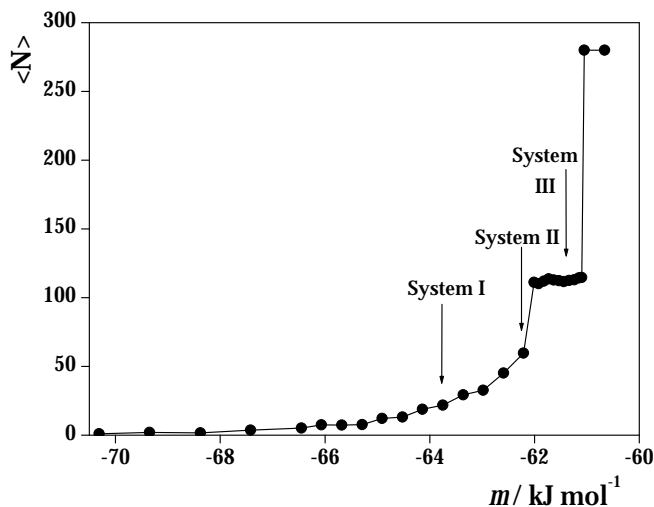


Figure 4.24: Average number of benzaldehyde molecules in the basic simulation box as a function of the benzaldehyde chemical potential. The arrows indicate the three systems considered for detailed analysis.

Considering the behaviour of the calculated isotherm we chose three different chemical potential values at which detailed analysis of the adsorption layer is performed. Thus, system I, corresponding to the chemical potential value of  $-63.75 \text{ kJ mol}^{-1}$  is located at the exponentially rising part of the isotherm. At this chemical potential value even the first molecular layer of the adsorbed benzaldehyde molecules is far from being saturated. System II, being at the  $\mu$  value of  $-62.21 \text{ kJ mol}^{-1}$  is located close to the saturation plateau, whereas system III is chosen to be at this plateau, at  $\mu = -61.44 \text{ kJ mol}^{-1}$ , where the benzaldehyde molecules form their particularly stable adsorption layer.

Our numerical study was carried out jointly with the experimental investigation of the group of Stéphane Le Calvé[115]. Their results are compared to ours in the next subsections.

**Comparison of the simulated and experimental isotherms.** To convert the experimental isotherm[115] to the  $\Gamma(p_{rel})$  form the  $p_0$  value was extrapolated, as it is not available in the literature, using the Antoine equation (see Eq 4.7). The Antoine parameter values of  $a = 16.35$ ,  $b = 3748.62 \text{ K}$ , and  $c = -66.12 \text{ K}$ [116], corresponding to the pressure value in Torr units, were used resulting in the  $p_0$  value of  $0.295 \text{ Pa}$  at  $233 \text{ K}$ .

From the calculated isotherm the value of  $\mu_0$  was determined to be  $-61.075 \text{ kJ mol}^{-1}$ . The comparison of the experimental and calculated isotherms obtained

at 233 K is presented in Figure 4.25. As is seen, the two isotherms are in excellent agreement with each other. Although the simulation data correspond to slightly lower surface coverage values, the two set of data agrees almost within the error bars with each other.

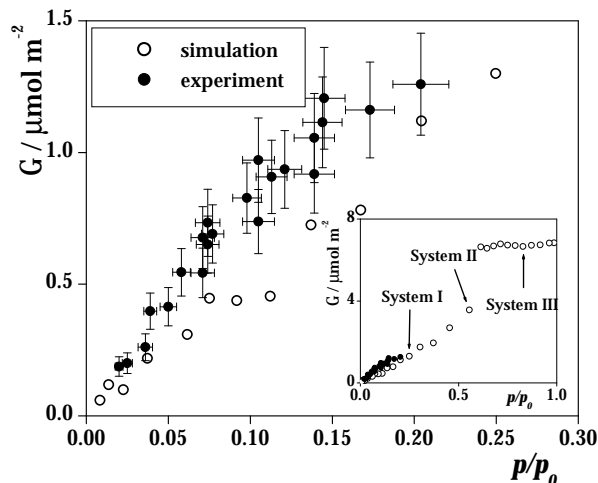


Figure 4.25: Comparison of the experimental (full circles)[115] and simulated (open circles) adsorption isotherms of benzaldehyde on ice at 233 K. The error bars of the simulated data points are always smaller than the symbols. The inset shows the same comparison in the entire  $0 \leq p_{rel} \leq 1$  pressure range. The arrows indicate the three systems considered for detailed analysis.

It should finally be noted that the simulated isotherm clearly shows a non-Langmuir behaviour above the pressure range explored in the experiments. This isotherm is quite similar to those found in the case of methanol[75] and formic acid (see Section 4.3), and is in a clear contrast with our previous findings concerning the adsorption of formaldehyde[85] and acetone (see Section 4.2) on ice. This can be interpreted in terms of possible strong lateral interactions of the adsorbed benzaldehyde molecules.

#### 4.4.2.2 Characterisation of the adsorption layers

**Density profiles.** The density profiles of the benzaldehyde molecules in systems I–III are shown in Figure 4.26. In calculating these profiles the position of the benzene ring C atom to which the CHO group is attached represented the position of the entire benzaldehyde molecule.

As is seen, in system I the obtained profile is unimodal, having its peak at the  $X$  value of 33.9 Å, just about 2 Å away from the point where the ice density

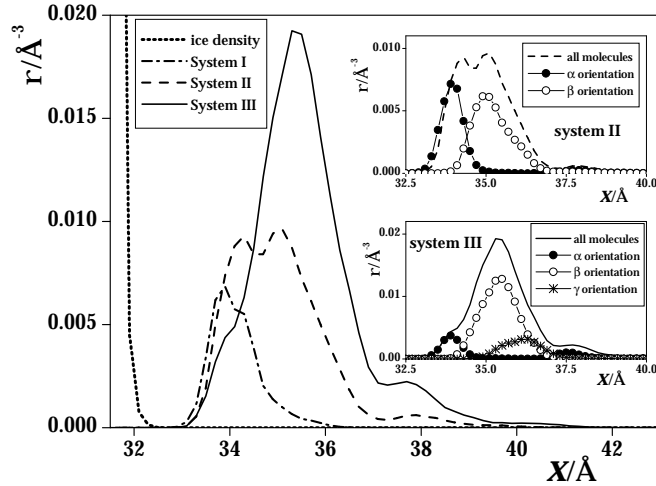


Figure 4.26: Number density profile of the adsorbed benzaldehyde molecules in system I (dash-dotted line), system II (dashed line), and system III (solid line). The number density profile of the surface waters is also indicated (dotted line). The insets show the contribution of the  $\alpha$  (full circles),  $\beta$  (open circles) and  $\gamma$  (asterisks) oriented benzaldehyde molecules to the total density profile in systems II (upper inset) and III (lower inset).

drops to zero. This close contact with the ice phase suggests that the benzaldehyde molecules in this system are probably lying parallel with the ice surface. In contrast, in system II the density profile is already bimodal. The first maximum of this broad curve is close to the position of the peak in system I, whereas the second peak appears farther away from the ice phase, i.e., at  $X = 35.1$  Å. The fact that the profile is now split into two peaks indicates that the adsorbed molecules are aligned in two different orientations relative to the ice surface. The difference of 1 Å between the position of the two peaks suggests that the other preferred orientation of the adsorbate molecules is probably close to be perpendicular to the surface.

Finally, in system III, the benzaldehyde density profile exhibits again a unimodal peak, now at  $X = 35.4$  Å, close to the position of the second maximum of the profile of system II, and only a shoulder is seen around the  $X$  value of 34 Å. This main peak is followed by a small second peak around the  $X$  value of 37.7 Å. This finding suggests that i) in system III, i.e., when benzaldehyde forms a particularly stable adsorption layer at the ice surface, the dominant orientation is already more or less perpendicular to the surface (simply because the number of adsorbed molecules can be maximised in this way), and ii) besides the saturated first molecular layer, traces of a second layer are also present in this stable adsorption layer.

**Orientation of the Adsorbed Molecules.** In analysing the orientation of the adsorbed benzaldehyde molecules relative to the ice surface we defined the local Cartesian frame in the following way. The origin of this frame is the O atom, its  $z$  axis points along the O=C double bond, the  $y$  axis also lies in the plane of the molecule and is oriented toward the benzene ring, while the  $x$  axis is perpendicular to the molecular plane. The surface normal vector  $\underline{X}$  is directed from the ice phase toward the adsorption layer by our convention. It should also be noted that, due to the planar structure of the benzaldehyde molecule, this frame can always be chosen in such a way that  $\phi$  does not exceed  $180^\circ$ . The definition of this local Cartesian frame is illustrated in Figure 4.27.

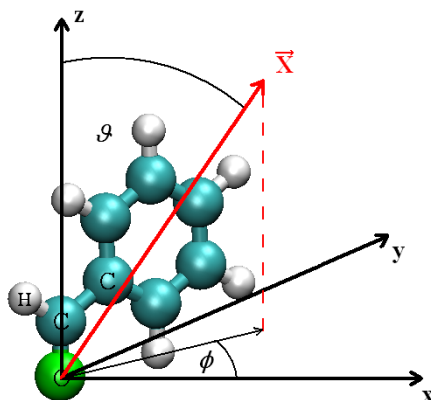


Figure 4.27: Definition of the local Cartesian frame fixed to the individual benzaldehyde molecules, and of the polar angles  $\vartheta$  and  $\phi$  of the surface normal vector, pointing, by our convention, away from the ice phase,  $\underline{X}$ .

The  $P(\cos \vartheta, \phi)$  orientational maps of the adsorbed benzaldehyde molecules in systems I–III are shown in Figure 4.28. Because the peaks of these maps are too sharp as compared to the maps of formic acid and acetone, we chose here to use a reverse colouring method, i.e., darker tones mean higher probabilities. As is seen, at low surface coverages (i.e., in system I) the  $P(\cos \vartheta, \phi)$  distribution exhibits two sharp peaks at the points characterised by  $\cos \vartheta = 0.1$ ,  $\phi = 0^\circ$ , and  $\cos \vartheta = 0.1$ ,  $\phi = 180^\circ$ . These peaks correspond to the same preferred alignment, denoted here by  $\alpha$ , i.e., when the benzaldehyde molecule lies almost parallel with the ice surface and the C=O bond declines slightly, by about  $5 - 10^\circ$  from the surface plane pointing toward the ice phase with the O atom.

With increasing surface coverages another peak of the  $P(\cos \vartheta, \phi)$  map, marked here by  $\beta$ , emerges around the point of  $\cos \vartheta = 0.2$ ,  $\phi = 90^\circ$ . In system II this peak is only seen as a small secondary maximum, but in system III it becomes dominant.

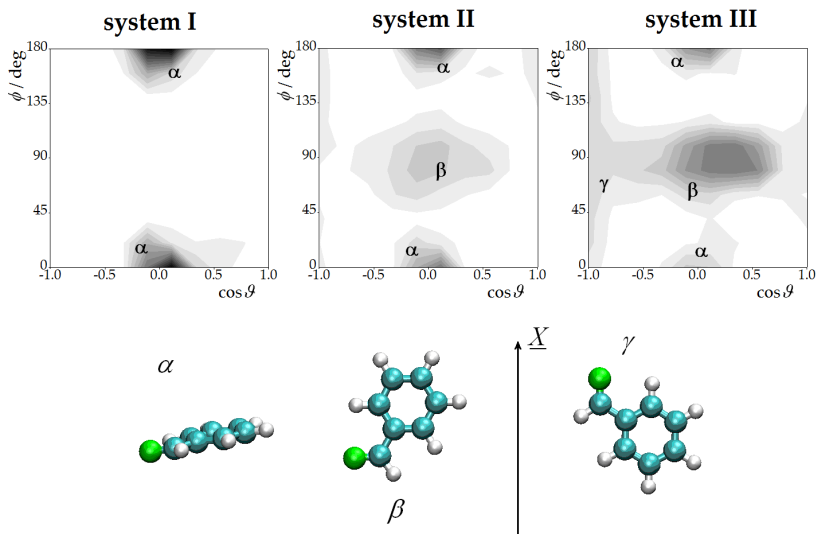


Figure 4.28: Orientational map of the adsorbed benzaldehyde molecules in systems I (left), II (middle), and III (right). Darker colours indicate higher probabilities. The peaks corresponding to the preferred benzaldehyde orientations are marked by  $\alpha$ ,  $\beta$ , and  $\gamma$ . These orientations are also illustrated.  $X$  is the surface normal vector pointing away from the ice phase.

In this alignment the plane of the benzaldehyde molecule is perpendicular to the ice surface, the axis of the C=O double bond forms an angle of about  $15 - 20^\circ$  with the surface, and the benzene ring points toward the vapour phase. Finally, in system III a third orientation, corresponding to the  $\cos \vartheta$  value of  $-1$  is also slightly preferred. In this orientation, denoted as  $\gamma$  the benzaldehyde molecule is again perpendicular to the ice surface, but points straight away from the ice phase by its carbonyl group. The preferred orientations  $\alpha$ ,  $\beta$ , and  $\gamma$  of the adsorbed benzaldehyde molecules are illustrated in Figure 4.28.

To support our previous conclusions drawn on the density profiles about the molecular orientations in system II and III, we also calculated separately the density profiles of the molecules being in the distinct orientations. This kind of deconvolution of the density peak is shown in the insets of Figure 4.26. This analysis reveals that the first deconvoluted density peak (i.e. being at the smallest  $X$  values) in system II and system III, similarly to the entire peak in system I, are indeed given by the adsorbate molecules of orientation  $\alpha$ . Further, the second peak of the deconvoluted density profile, located at about  $35.5 \text{ \AA}$  in system II and system III is given by the molecules that are perpendicular to the surface. Benzaldehyde molecules of orientation  $\gamma$  in system III give rise to the profile at high  $X$  values. Finally, it is also seen that the molecules forming traces of the second molecular layer in system III

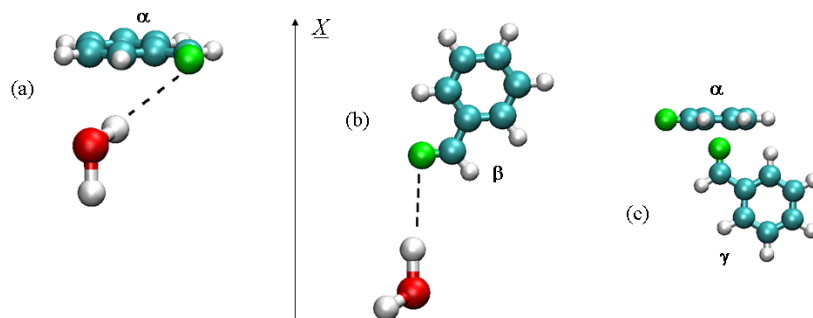


Figure 4.29: Illustration of the strong attractive interactions between (a) a water and an adsorbed benzaldehyde of orientation  $\alpha$ , (b) a water and an adsorbed benzaldehyde of orientation  $\beta$ , and (c) a benzaldehyde of orientation  $\alpha$  and an other one of orientation  $\gamma$ .  $\underline{X}$  is the surface normal vector pointing away from the ice phase.

are again in orientation  $\alpha$ .

These orientational preferences can be understood by considering the possible interactions the molecules can form in the given orientations. Thus, the interactions of the molecules being in orientation  $\alpha$  are maximised due to the lying position since, in this way, their atoms can get as close to the previous layer as possible. The highly electronegative O atoms of either the waters or the  $\gamma$  benzaldehydes located in the first layer can interact with the enhanced electronic density of the benzene ring of a benzaldehyde molecule. On the other hand, these lying molecules are able to form hydrogen bonds with the flatly aligned surface OH groups[75] of the ice phase due to the slight,  $5 - 10^\circ$  deviation of the C=O axis from the exactly parallel alignment with the surface.

Upon saturation of the first molecular layer, however, the increasing amount of the adsorbate molecules increases the competition for the area to be occupied at the surface, and hence the preference for the perpendicular orientations also increases. Orientation  $\beta$  can be stabilised by a hydrogen bond formed with a surface water molecule (see Figure 4.29b). The preference of the benzaldehyde molecules for orientation  $\gamma$  occurs simultaneously with the appearance of the second molecular layer in system III. This alignment is stabilised by the interactions formed with the  $\alpha$  oriented lying molecules of the second layer as it was detailed above (see Figure 4.29c).

It should be noted that the picture we have seen in the orientational preferences of the adsorbate molecules is quite similar to that seen in the study of the adsorption of acetone.

**Energetics of the Adsorption.** In order to analyse the energetic background

of the adsorption the procedure presented in a former sections of this chapter (see Section 4.1.1.4) was also performed. The resulting  $P(U^{TOT})$ ,  $P(U^{ice})$  and  $P(U^{BA})$  distributions are illustrated in Figure 4.30 as obtained in systems I–III.

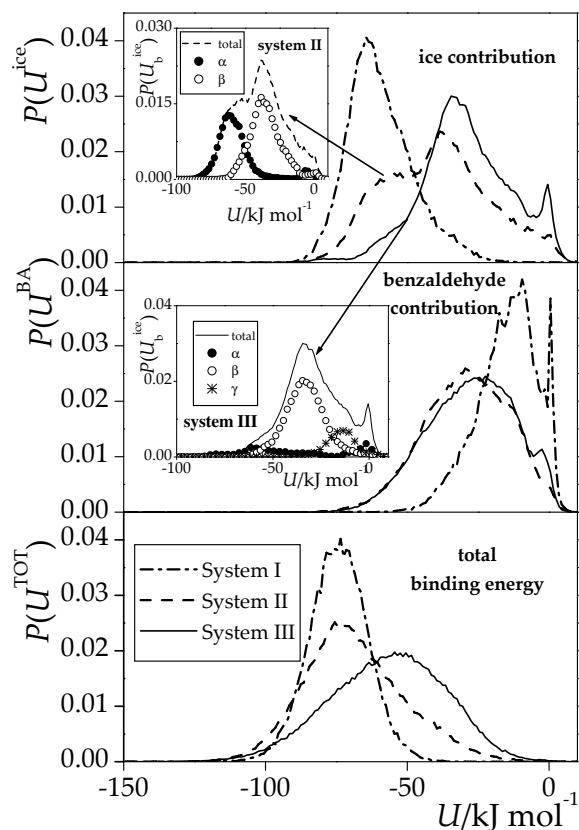


Figure 4.30: Distribution of the total binding energy of an adsorbed benzaldehyde molecule and the contributions coming from the interactions with the other adsorbed benzaldehyde molecules (middle panel) and with the ice phase (top panel) in systems I (dash-dotted line), II (dashed line), and III (solid line). The insets show the contribution of the  $\alpha$  (full circles),  $\beta$  (open circles) and  $\gamma$  (asterisks) oriented benzaldehyde molecules to the  $P(U^{ice})$  distribution in systems II (upper inset) and III (lower inset).

In system I, the distribution of the ice – benzaldehyde interaction  $P(U^{ice})$  is unimodal, having its peak at about  $-64 \text{ kJ mol}^{-1}$ . The unimodality of this peak is in accordance with our previous finding that here all the adsorbed molecules are aligned in the same way. The mean value of this distribution is  $(-59.4 \pm 5.1) \text{ kJ mol}^{-1}$  (error corresponding to the 95% level of confidence), which agrees roughly with the sum of the mean ice – benzene interaction energy ( $-39 \text{ kJ mol}^{-1}$  measured at the surface of amorphous solid water at 141 K)[117] and the mean ice – formaldehyde interaction energy ( $-27.3 \text{ kJ mol}^{-1}$  obtained from computer simulation at the surface of Ih ice at

200 K)[85] at low surface coverages. Further, this value is in an excellent agreement with the experimental value of the adsorption enthalpy of  $(-61.4 \pm 9.7)$  kJ mol<sup>-1</sup>, obtained at very low surface coverages[115].

In system II the  $P(U^{ice})$  distribution is bimodal: besides its peak around  $-58$  kJ mol<sup>-1</sup> it also exhibits another, higher peak at about  $-38$  kJ mol<sup>-1</sup>. This bimodal shape is consistent with the dual orientational preferences of the adsorbed molecules as the peak at lower energies is given by the  $\alpha$ , while that at higher energies by the  $\beta$  oriented benzaldehyde molecules (see the upper inset of Figure 4.30).

Finally, in system III, the main peak of the  $P(U^{ice})$  distribution appears at about  $-34$  kJ mol<sup>-1</sup>, and it also has two shoulders located at  $-58$  kJ mol<sup>-1</sup> and  $-14$  kJ mol<sup>-1</sup>. This distribution has also a second peak of smaller intensity close to zero. As is expected, the shoulder at low energies is given by the few  $\alpha$  oriented molecules, while the main peak is related to the  $\beta$  oriented molecules. The high energy shoulder can be attributed to the molecules of orientation  $\gamma$ , whereas the peak around zero energies is given by the molecules of the second molecular layer as they are already far from the surface (see the lower inset of Figure 4.30).

The  $P(U^{BA})$  distribution has a peak at zero and another one around  $-10$  kJ mol<sup>-1</sup> in system I. The zero energy peak is clearly coming from the isolated benzaldehyde molecules. The presence of the other peak in the system of low surface coverage indicates the tendency of the adsorbed benzaldehyde molecules for forming lateral self-aggregates rather than being always isolated from each other. At higher surface coverages, however, the  $P(U^{BA})$  distribution becomes unimodal, having its peak around  $-28$  kJ mol<sup>-1</sup>. This energy might be related to the  $\pi$ - $\pi$  and dipole-dipole type interaction of the neighbouring adsorbate molecules.

The distribution of the entire binding energy  $P(U^{TOT})$  exhibits a single peak around  $-75$  kJ mol<sup>-1</sup> both in system I and system II. The total energy of the adsorption of a benzaldehyde molecule in these systems is rather low, and is also comparable with multiple hydrogen bond forming adsorbates such as methanol[75] or formic acid (see Section 4.3). The lack of the possibility of multiple hydrogen bond formation is compensated here by either the strong interaction formed between the benzene ring and a strongly electronegative O atom or the  $\pi$ - $\pi$  and dipole-dipole type interactions between two perpendicularly oriented adsorbate molecules. Further increase of the surface coverage leads to somewhat weaker average attraction experienced by the individual molecules, as is reflected in the fact that the peak of the  $P(U^{TOT})$  distribution appears around  $-50$  kJ mol<sup>-1</sup> in system III. This weakening of the average binding energy is, however, overcompensated by the large increase of the number of adsorbed molecules, making thus the saturated adsorption layer

considerably stable.

## 4.5 Conclusions

In this chapter we have presented a numerical procedure enabling us to thoroughly investigate adsorption processes in computer simulations based on the GCMC method, as it has been demonstrated in the case of the adsorption of acetone, formic acid and benzaldehyde at the surface of Ih ice. The questions posed in the introduction of this chapter are now answered, showing that the results of this procedure can clearly contribute to the understanding of the adsorption processes at the molecular level. Computer simulation techniques allow us to study the mechanism, the energetic background as well as the driving force of the adsorption at the different stages of the adsorption process.

We have seen that the studied isotherms can be characterised by a Langmuir-like behaviour only in a low pressure range. This range corresponds to the occupation of the adsorption sites by molecules being in a typical orientation. At this very low pressure region the assumptions of the Langmuir isotherm are valid, and the adsorbate – ice interaction is clearly the driving force of the adsorption. In studying the adsorption behaviour and the possibility of multilayer adsorption one can also use the BET isotherm, whose two of the three main assumptions are the same as in the Langmuir theory.

The saturated monomolecular surface density obtained from the simulation always exceeds the monolayer capacity of the BET and of the Langmuir theory, as these latter values correspond to the occupation of only one type of adsorption sites. By increasing pressure, the adsorbate – adsorbate interactions become more and more important, simultaneously with the decrease of the surface area available for the adsorbates. These effects result in the change of the preferences for surface orientations. We also identified the main type of interactions formed between an adsorbate and a water molecule as well as between two adsorbate molecules. In the systems studied, the former was always H-bond, whereas the latter might be either dipole–dipole type interaction (in the case of acetone and benzaldehyde), or  $\pi$ – $\pi$  type interaction of benzaldehyde, or O–H $\cdots$ O and C–H $\cdots$ O type H-bonds between formic acids leading to the appearance of cyclic dimers or intra-layer H-bonding motives.

In investigating the adsorption of formic acid and benzaldehyde, our computer simulation study was performed jointly with experimental measurements, providing thus the possibility of the direct comparison of our results with the experiments. For

benzaldehyde and formic acid the agreement between measured and simulated data was excellent. In the case of acetone the comparison was more difficult because of the great diversity of the measured curves. Generally, even if a reliable experimental adsorption isotherm exists in the literature the comparison is not always easy to perform because, on one hand, either the measured saturated vapour pressure values are not available or the parameters of the Antoine equation do not produce trustworthy result at the investigated temperature. On the other hand, contrary to the experiments, the structure of the ice crystal in simulations is always perfect, whereas real ice crystals have a defected surface that may result in enhanced adsorption capacity[101, 102]. Thus, an excellent accordance between experimental and measured isotherms is not always achievable even if the potential models used in the simulations are suitable for our purpose.

However, the reasonable reproduction of the experimental adsorption isotherms as well as heats of adsorption is a clear test of the reliability of the potential model used. In our studies, the experimental heats of adsorption were always very well reproduced, confirming our choice of potential model in every case. The separate analysis of the molecules giving rise to different density peaks or those being in different orientations allows us to explain the scenario of the adsorption. We can also interpret the possible structure of the adsorption layer by identifying the molecules bound to the surface, and those binding to molecules being in the next layer.

The studies presented in this chapter doubtlessly demonstrated that the GCMC simulation technique is a very useful tool in understanding the mechanism of the adsorption processes, since, by the use of this technique, it is possible to reveal the atomistic details, which are invisible in experiments. Furthermore, simulations can provide predictive information on systems, which are under conditions that exclude, or, at least, make difficult their experimental investigation.

## Chapter 5

# Water adsorption on soot

### 5.1 Introduction

In the previous chapter we have studied adsorption on the surface of ice, which is known to be the most abundant atmospheric solid particle (see Section 2.4.1). Now we will focus on soot, which is also very abundant in Earth's atmosphere. More precisely, we are now aiming at investigating the possible effects of the structural and morphological characteristics of soot particles on the water adsorption. From an experimental point of view, this phenomenon seems quite challenging, because an exhaustive study requires geometrical, chemical and optical characterisation of the primary carbonaceous soot particles[34]. Since in-situ measurements are hardly feasible, the hydration properties of soot in real conditions, e.g. behind airplanes are poorly known. It is thus again a situation where the real power of computer simulation techniques can be exploited.

As it has been discussed in Section 2.4.2, the primary soot particles are found to have an onion-like structure and a quasi spherical shape, with diameters ranging between 5 and 50 nm. It is also known that soot may contain a certain number of hydrophilic sites[39]. The presence of both such polar groups and micropores in the structure of soot can explain the unexpected affinity between such carbonaceous particles and water[118].

From a theoretical point of view, a lot of studies have recently been published on the adsorption of water in porous carbon[119, 120, 121, 122, 123, 124]. Such a molecular level understanding can be achieved by performing either first-principles calculations, or numerical simulations based on empirical potentials to describe the water-soot interactions. In a series of previous papers, quantum chemical calculations[125,

126, 127, 128] were used to characterise the influence of the polar OH, COOH, and C–O–C (epoxide-like) groups on the water adsorption at a partially oxidised soot particle of nanometer size. The results of these calculations clearly showed the preferential adsorption of water molecules at carbonaceous surfaces containing carboxyl rather than hydroxyl or epoxide-like groups, because of the possible formation of two hydrogen bonds between the COOH group and the first water molecules. These results were confirmed by classical molecular dynamics simulations performed at finite temperature using empirical potential models fitted to results of quantum mechanical calculations[129, 130, 131].

Further, Moulin and co-workers[132, 133] carried out GCMC simulations to calculate water adsorption isotherms on model soot particles of spherical shape. These soot particles either consisted of carbon atoms only[132], or contained also a small amount of oxygen atoms in the form of COOH and OH groups randomly distributed inside and at the outer surface of the soot particle[133]. The main conclusion of these studies is that the driving force of the water adsorption outside or/and inside carbonaceous nanoparticles mostly comes from the attraction of the already adsorbed water molecules. The first water molecules can be trapped by hydrophilic chemical groups, or by confinement effects in pores of small size. However, this latter conclusion might depend not only on the size of the pores, but also on the way they are created in the carbonaceous structure. Indeed, these soot nanoparticles were made of randomly distributed elemental chemical units on concentric spheres, each elemental unit containing 19 C atoms arranged in five fused benzene rings.

Contrary to the work of Moulin et al. our goal was to study more realistic carbonaceous particles that might thus be considered as trustworthy models of real soot particles. The adsorption isotherms as well as the energetic and morphological details of the adsorption process were then investigated and will thus be presented in the following.

## 5.2 Computational details

### 5.2.1 Soot models

Two different types of soot particles were considered in our studies. The starting point in the construction of type I particles was a soot ball with an onion-like structure consisting of four concentric spherical fullerene molecules that can be characterised by the radii of 7.04 Å (C<sub>240</sub>), 10.89 Å (C<sub>540</sub>), 14.36 Å (C<sub>960</sub>) and 18.15 Å

( $C_{1500}$ ). In this  $C_{240}@C_{540}@C_{960}@C_{1500}$  particle the distance between two successive shells ranges from 3.5 to 3.8 Å, close to the distance of two successive graphite layers[134]. Then, at the surface of each shell pores of a radius varying from 1.2 to 3.4 Å were created in randomly chosen positions. Two neighbouring pores were separated by the distance of 3.0–6.8 Å from each other. Four models of this type, consisting of 2976, 2376, 2207 and 2133 carbon atoms, respectively, were generated with different pore densities. The resulting structures were then relaxed in a molecular dynamics simulation, performed on the canonical ( $N,V,T$ ) ensemble at 298 K, in which the C–C interactions were described by the reactive AIREBO potential[56]. The use of this potential allows to break and create bonds as it has been shown in Section 3.1.3.2. These simulations were 48 ps long, using the integration time step of 1 fs. This procedure resulted in four different soot models, characterised by different carbon atom densities and morphologically different cavities. The particles containing 2976, 2376, 2207 and 2133 carbon atoms, shown in Figure 5.1, will be referred to in the following text as  $S_1^I$ ,  $S_2^I$ ,  $S_3^I$  and  $S_4^I$ , respectively.

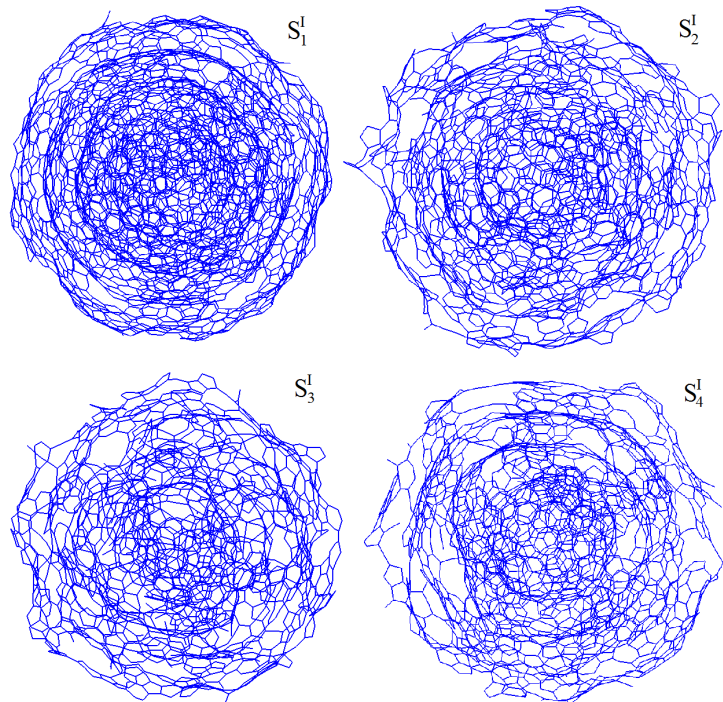


Figure 5.1: The four type I soot models:  $S_1^I$ ,  $S_2^I$ ,  $S_3^I$  and  $S_4^I$  containing 2976, 2376, 2207 and 2133 atoms respectively.

A different type of soot particle, marked as type II was also created using a similar procedure. This model is based on the five-shell  $C_{60}@C_{240}@C_{540}@C_{960}@C_{1500}$  concentric fullerene particle. However, in contrast to type I models, here one single

large cavity was created inside the soot ball in the following way: A second shell atom was randomly chosen as the center of the initial cavity, and all carbon atoms being located closer to the central one than  $8.81 \text{ \AA}$  were then removed. The resulting structures were relaxed in a molecular dynamics simulation with the use of the AIREBO potential in the same way as in the case of the type I soot models. The structure containing one large cavity is denoted by  $S^{II}$ .

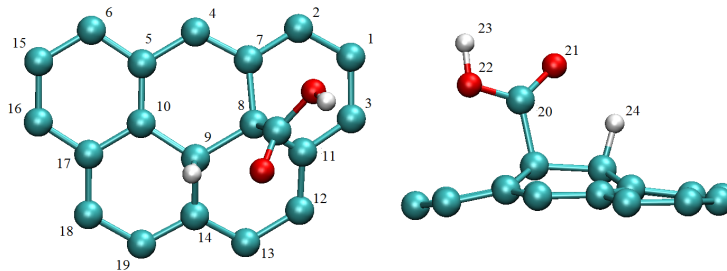


Figure 5.2: The  $C_{19}HCOOH$  unit placed inside the type II soot model. The numbers indicate the numbering of the atoms of this motive.

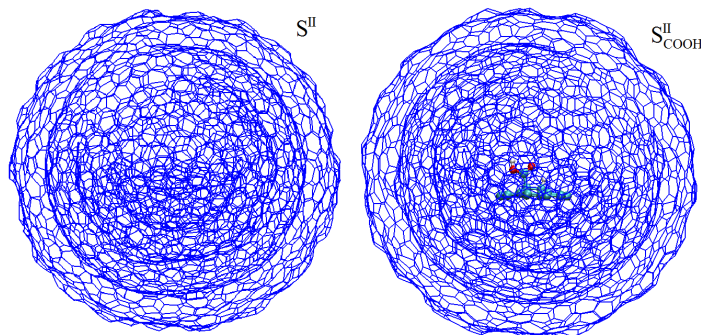


Figure 5.3: Type II soot models with and without the  $C_{19}HCOOH$  unit inside:  $S^{II}$  and  $S^{II}_{COOH}$ , both containing 2999 carbon atoms.

Finally, to study also the effect of chemical defects on water adsorption a modified version of the  $S^{II}$  soot model was also considered. In their work, Moulin et al.[133] demonstrated that a carbonaceous surface consisting also of several COOH groups can attract more water molecules than the pure carbon surface, whereas the presence of the OH groups has no such effect. Therefore, in the modified version of the  $S^{II}$  soot particle the innermost carbon motive containing 19 atoms (i.e., what remained from the innermost  $C_{60}$  fullerene after the removal of the carbon atoms) was substituted with a  $C_{19}HCOOH$  unit, consisting of five fused benzene rings ( $C_{19}$ ) as well as an additional COOH group and a H atom anchored to the surface. The COOH group and the H atom were placed to the C8 and C9 carbon atoms of this unit, respectively,

breaking a double bond of the conjugate system.

The resulting  $C_{19}HCOOH$  unit was then optimised in ab initio calculation[125, 126]. The atomistic structure of this unit as well as the numbering scheme of its carbon atoms is illustrated in Figure 5.2. The soot ball obtained by substituting the innermost carbon motive of  $S^{II}$  with this  $C_{19}HCOOH$  unit is referred to here as  $S_{COOH}^{II}$ . Figure 5.3 illustrates the structure of the type II soot particles considered.

The radius of all soot models considered here falls into the range of 17–18 Å. It should finally be emphasised that these models are more realistic representations of soot emitted by aircrafts or collected in flames than what was used in previous studies[132, 133] in the sense that they are chemically stable. Indeed, soot models considered in former analyses contained randomly distributed carbonaceous units on concentric spheres in a non-optimised arrangement. In contrast, the stability of the present models is provided by the use of the reactive potential in the relaxation procedure.

### 5.2.2 Grand canonical Monte Carlo simulations

In order to calculate the adsorption isotherm of water on the various soot models, we performed a series of GCMC simulations at 298 K. The edge length of the basic cubic simulation box was set to 85.27 Å in every case. Standard periodic boundary conditions were applied. The value of the chemical potential was controlled through the  $B$  parameter of Adams (see Eq 3.21). The simulations were performed at different  $B$  values, ranging between  $-2$  and  $1.6$ , corresponding to the chemical potential range of  $[-48.5; -39.6]$  kJ mol $^{-1}$ .

Water molecules were described by the rigid four-site TIP4P model[135]. The interaction potential between the soot and the water molecules was calculated as the sum of pairwise additive atom-atom Lennard-Jones contributions between the atoms of the soot and of the water molecules. Hydrogen atoms were disregarded. A second, electrostatic term of the interaction potential was also taken into account coming from the interaction between point charges located on water molecules and on the  $C_{19}HCOOH$  unit. The charges of this latter were computed by ab initio calculations[125, 126]. The parameters of these interactions are summarised in Tables 5.1 and 5.2.

The soot particles were regarded as indeformable rigid bodies in the simulations. Moreover, the soot particles were considered as being chemically inert with respect to water, i.e., water chemisorption or dissociation events were disregarded. All interactions beyond the cut-off radius of 12.5 Å were truncated to zero. To perform

Atom type	Involved atoms	$\epsilon / \text{kJ mol}^{-1}$	$\sigma / \text{\AA}$
hydroxyl O	O22	0.879	2.95
carbonyl O	O21	0.707	2.99
carboxylic O	C20	0.439	3.74
C-(COOH)	C8	0.439	3.74
C(-H)	C9	0.439	3.74
bare C	all other soot atoms	0.273	3.40

Table 5.1: Lennard-Jones parameters corresponding to the different soot atoms. The numbering scheme of the atoms of the  $\text{C}_{19}\text{HCOOH}$  unit is shown in Figure 5.2.

Atom	$q / e$	Atom	$q / e$	Atom	$q / e$
C(1)	0.02632	C(9)	0.03061	C(17)	-0.07994
C(2)	-0.00799	C(10)	0.01969	C(18)	0.08944
C(3)	-0.03800	C(11)	-0.02432	C(19)	-0.03808
C(4)	-0.01532	C(12)	-0.06398	C(20)	0.70994
C(5)	-0.05713	C(13)	-0.02978	O(21)	-0.50409
C(6)	0.0000	C(14)	-0.04232	O(22)	-0.58818
C(7)	-0.06614	C(15)	0.00000	H(23)	0.45265
C(8)	0.14731	C(16)	0.00000	H(24)	0.07931

Table 5.2: Point charges located on the  $\text{C}_{19}\text{HCOOH}$  unit, used in the calculation of the electrostatic interaction between water and soot. The numbering scheme of the atoms of the  $\text{C}_{19}\text{HCOOH}$  unit is shown in Figure 5.2.

the simulations Mezei's MMC code[88] was used. During the simulations water displacement and insertion/deletion attempts were done in an alternating order. In a particle displacement step a randomly chosen water molecule was translated to a random distance by no more than  $0.25 \text{ \AA}$ , and rotated around a randomly chosen space-fixed axis by no more than  $15^\circ$ .

In an insertion/deletion attempt it was tried either, by 50 % probability, to remove a randomly chosen water molecule from, or, also by 50 % probability, to insert an extra water molecule to the system. For inserting a molecule the cavity-biased algorithm of Mezei[46, 47] was applied. The systems were equilibrated by performing  $6 \times 10^8$  Monte Carlo steps. In the production stage, the total number of water molecules in the system was averaged over  $4 \times 10^8$  Monte Carlo steps long trajectories. For further analyses, 4000 equilibrium sample configurations, separated by  $10^5$  Monte Carlo steps each, were saved at selected chemical potential values.

## 5.3 Results

### 5.3.1 Adsorption isotherms

The adsorption isotherms obtained for the different I and II type soot models are shown in Figures 5.4 and 5.5 respectively. As it can be seen, the different type I model soot particles have rather similar adsorption abilities. Although the adsorption isotherm of the  $S_1^I$  particle, i.e., the one being characterised by a noticeably higher density than the others start to rise at lower chemical potential (i.e., at lower relative pressure), type I particles exhibit a rather similar isotherm. To distinguish between the water molecules adsorbed by soot particles and the ones being in the vapour phase of the system we calculated the average number of water molecules being located inside the soot particle,  $\langle N_{inside} \rangle$  at selected chemical potentials. The obtained values of  $\langle N_{inside} \rangle$  are also included in Figures 5.4 and 5.5. As is seen, all the type I soot particles can incorporate about 20 water molecules. In interpreting this result, it should be noted that the largest pore inside these soot models is located in the middle of the particle, inside the innermost fullerene layer, where a  $C_{60}$  fullerene layer could be still incorporated. The obtained results suggest that the smaller pores scattered inside the different type I soot particles in different densities and in different ways do not play an important role in water adsorption.

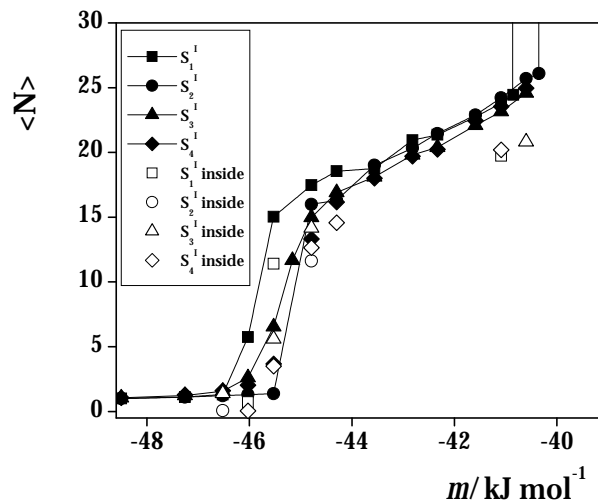


Figure 5.4: The adsorption isotherms obtained on type I soot models:  $S_1^I$  (squares),  $S_2^I$  (circles),  $S_3^I$  (triangles),  $S_4^I$  (diamonds). Open circles correspond to the equilibrium number of water molecules inside the soot particles.

This picture is further refined by considering the results obtained for the two type II soot models. As is seen from Figure 5.5, the addition of an internal COOH group has a strong effect on the adsorption properties. Namely, the adsorption of water starts at considerably lower chemical potential values (and, hence, at lower vapour pressures) if the adsorbing soot particle contains also a polar COOH group in its internal core. In this case, the water molecules directly bound to the single COOH group can act as a condensation center. Thus, their presence in the system at lower chemical potential values than what corresponds to the appearance of the first water molecules in the bare carbon soot  $S^{II}$  attracts also a number of other water molecules, which are bound to these ‘primary’ waters by hydrogen bonding interactions. It is also seen that the saturation part of the two isotherms almost perfectly coincides with each other, both of the type II soots considered can incorporate about 65–70 water molecules, reflecting also the much larger size of the internal pore in the type II soot than that in the type I soot particles.

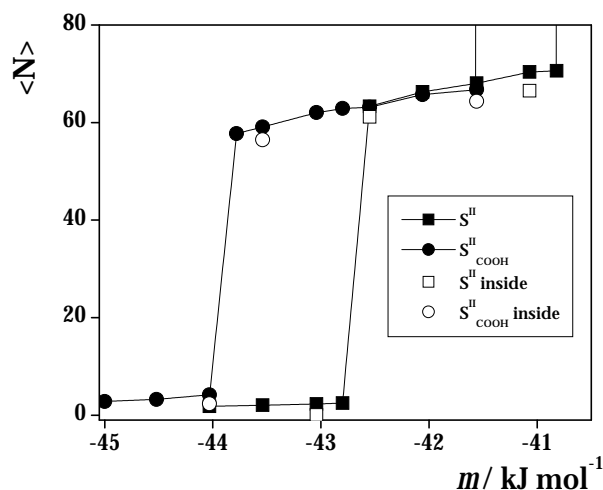


Figure 5.5: Adsorption isotherms obtained on type II soot models:  $S^{II}$  (squares) and  $S^{II}_{\text{COOH}}$  (circles). Open symbols indicate the average number of waters inside the soot particles.

It should be noted that hysteresis phenomenon is expected to occur when studying the adsorption in such a porous media as our soot particles. To investigate the possible effect of the desorption hysteresis we repeated, as a test, the calculation of the adsorption isotherm on the  $S_2^I$  particle starting the simulation from a box that contained a particle full of water molecules. It turned out that the obtained desorption isotherm is almost identical to the adsorption isotherm indicating that there is

no significant hysteresis related to water adsorption on this kind of soot particles.

The obtained results suggest that two possible factors might determine the adsorption ability of the different soot particles. First, the size and shape of the pore plays an important role in this respect. It is clear that the main driving force of water adsorption in large apolar carriers, such as soot balls is the water–water interaction, i.e., the possibility of hydrogen bond formation with already adsorbed water molecules[132, 133]. Therefore, adsorbing pores should be large enough, and their shape should be sufficiently compact to host a large enough water cluster the molecules of which can form a sufficient number of hydrogen bonds to stabilise themselves in the apolar environment. If the pore is too small or it is simply too narrow then the number of hydrogen bonded neighbours of the water molecules is limited by these geometric constraints. In this case, the energy gain of the adsorbed water molecules might not overcompensate the effect of the entropy loss accompanying their clustering, which prevents their adsorption. This seems to be the case in the smaller pores of the type I soot particles. Further, the amount of water a soot particle can adsorb is obviously related to the size of the pore inside the soot.

On the other hand, water–water interaction can only lead to the adsorption of new water molecules if the soot already contains at least some traces of water. Thus, the second possible factor that might determine adsorption is the ability of the soot particle of attracting the first few water molecules. In other words, the pores inside the soot might contain a few adsorption sites at which water molecules can be particularly strongly bound even in the absence of other water molecules. In this case, these first adsorbed waters can act as nucleation centers for the adsorption at higher chemical potential values. This effect is clearly demonstrated in the case of the type II soot particles, where the optimal location of the first adsorbed water molecules can indeed initiate the adsorption of other water molecules, and it is also likely to be the factor responsible for the fact that the adsorption isotherms obtained on the different type I soot particles start at somewhat different chemical potentials.

In order to investigate the impact of these two factors, i.e., the role of the optimal pore shape and of the optimal location of the first adsorbed molecules, in the following we analyse in detail the position of the first adsorbed molecules inside the various soot balls, the morphological properties of the pores in our various soot models, and the energetic background of the adsorption process investigated.

### 5.3.2 Position of the first adsorbed molecules

In order to investigate the role of the position of the first few adsorbed water

molecules we determined the position of the water molecules inside the  $S_2^I$ ,  $S_3^I$  and  $S_{COOH}^{II}$  soot balls at very low loadings, i.e., at the chemical potential values of  $-46.52 \text{ kJ mol}^{-1}$  ( $S_2^I$  and  $S_3^I$ ) and  $-44.03 \text{ kJ mol}^{-1}$  ( $S_{COOH}^{II}$ ). In these systems,  $S_2^I$ ,  $S_3^I$  and  $S_{COOH}^{II}$  soots contain, on average, 0.064, 1.4 and 2.32 water molecules, respectively. To map the position of the adsorbed water molecules we set a  $120 \times 120 \times 120$  grid on each soot (using the grid spacing of  $0.33 \text{ \AA}$ ), and marked the grid points at which an adsorbed water molecule is found at least  $\nu$  times in our samples. The value of  $\nu$  is set to 1, 3 and 10 for the  $S_2^I$ ,  $S_3^I$  and  $S_{COOH}^{II}$  soot balls respectively.

The maps of these first adsorbed water molecules inside the  $S_2^I$ ,  $S_3^I$  and  $S_{COOH}^{II}$  soots are shown in Figure 5.6. As is seen, in all cases there are some particular regions of the largest, innermost cavity where these water molecules prefer to stay. An equilibrium snapshot of the largest cavity inside the  $S_2^I$  soot at high loading (corresponding to the chemical potential value of  $-39.86 \text{ kJ mol}^{-1}$  and to the average number of adsorbed water molecules of 23) is also shown in Figure 5.6. The comparison of this snapshot (Figure 5.6b) with the map of the possible binding positions of the first water molecules at low pressures (Figure 5.6a) shows that the positions among which a few are occupied by the first adsorbed water molecules agree well with the positions of the water molecules located in the pore at high loadings.

At low pressure, the binding positions in  $S_3^I$  soot (Figure 5.6c) are located close to the surface of the pores at points where it is locally of rather large curvature, and hence a large number of close water-carbon contacts can be formed. Such positions are typically located at the vicinity of a pentagonal face of the fullerene layer (as the curvature of the fullerene surface is larger at the pentagonal than at the hexagonal faces). Such a ‘nest’ for an initially adsorbed water molecule is marked by A in Figure 5.6c.

As is seen, in this position the distance of the adsorbed water molecule from all the C atoms of the nearby pentagonal face falls always between  $3.4$  and  $3.6 \text{ \AA}$ . Another possibility is if the water molecule is close to the C atoms of two consecutive fullerene layers. An example for this is the position marked by B in Figure 5.6c, which is located in a small pore, merged with the largest cavity inside the soot. In this way, the water molecule occupying position B can be equally close (i.e., within  $4.0$ – $4.5 \text{ \AA}$ ) to a number of C atoms of the innermost fullerene layer and also to those of the outer layer (not shown in Figure 5.6c for clarity).

Finally, Figure 5.6d shows the preferential location of the first water molecules adsorbed by the  $S_{COOH}^{II}$  soot. As is expected, these water molecules are almost exclusively located around the polar COOH group of the  $C_{19}HCOOH$  unit, presumably forming multiple hydrogen bonds with it.

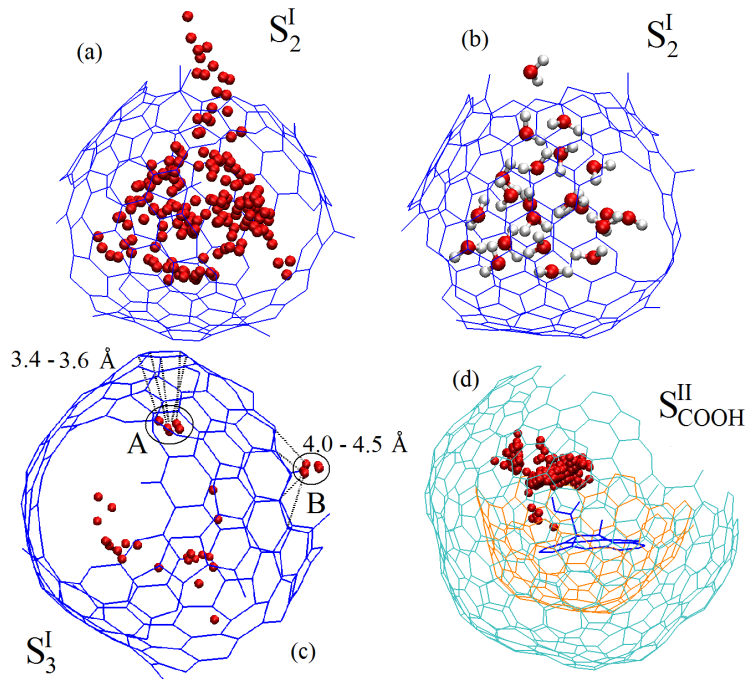


Figure 5.6: Preferential positions of the first adsorbed water molecules inside the (a)  $S_2^I$ , (c)  $S_3^I$ , and (d)  $S_{COOH}^{II}$  soot balls at low loading. For clarity, only the inner part of the soot balls is represented. An equilibrium snapshot of the water molecules inside the largest cavity of the  $S_2^I$  soot at high loading is also shown in this Figure (b)

### 5.3.3 Analysis of the pore morphology

In order to investigate the role of the second possible factor, i.e., pore morphology on the adsorption ability of the soot ball, we analyse here the size, the length and the volume of the pores in our soot models. (It should be recalled that although the pores were originally created by removing the C atoms located within a pre-defined sphere from the soot ball, this initial spherical shape of the pores could be severely modified during the relaxation of the soot particles in the molecular dynamics simulations done with the reactive AIREBO potential, see Section 5.2.1). Since this morphological study was not carried out by myself, we will not go into the details, but for clarity, the basis of this analysis will be shortly summarised here.

A very efficient approach of studying the morphology of interatomic pores is based on the Voronoi-Delaunay method[136, 137, 138, 139, 140]. In a three dimensional assembly of atoms the Voronoi region of a given atom is the locus of the spatial points that are closer to this atom than to any other one. If all the atoms are of the same size, this region is the well known Voronoi polyhedron[141, 142].

The Voronoi regions constructed for all atoms constitute a tessellation, namely a decomposition of the space without gaps and overlaps. The edges and vertices of the Voronoi regions pertinent to this tessellation constitute a network (called the Voronoi network). Edges and vertices of the Voronoi network are the loci of points that are equally far from the nearest three and four atoms, respectively. Thus, each vertex of the Voronoi network corresponds to a quadruplet of four mutually neighboring atoms, whose particular feature is that the inscribed sphere between them is empty, i.e., does not overlap with any atoms of the system. Such a quadruplet of atoms determines a tetrahedron, called the Delaunay simplex. Thus, the Delaunay simplices represent the simplest cavities located between the atoms, and any complex pore can be considered as a cluster of such simplices.

Further, each edge of the Voronoi network represents a fairway passing through the narrow bottleneck between three atoms from one vertex to the neighbouring one. These features make the Voronoi network a very convenient tool for analysis of pores. Once this network is determined, the properties of the corresponding pores can be easily analysed[138, 139]. Algorithms and programs for constructing the Voronoi network can easily be found for the special case of uniform atom size[145], whereas for the general case of atoms of different radii such an algorithm was recently published[146]. It should be noted that our models consist of C atoms of uniform size, with the exception of the two O atoms of the  $C_{19}HCOOH$  units present in the  $S_{COOH}^{II}$  soot model. (Since the H atoms do not carry Lennard-Jones interaction centers, they are also neglected in this analysis).

A physically meaningful way of defining pores is to regard regions of the empty interatomic space that is accessible for a spherical probe of the pre-defined radius  $R_{probe}$ . Here we set  $R_{probe}$  to be  $1.4 \text{ \AA}$ , corresponding roughly to the size of a water O atom. In this way, regions of the empty space between the soot C atoms that are accessible for a single water molecule are considered as pores. Thus, interstitial spheres (determined by the Delaunay simplices) with the radius larger than  $1.4 \text{ \AA}$  correspond to the simplicial cavities accessible for our probe. Further, if the bottleneck radius between two such neighbouring simplicial cavities is also larger than  $1.4 \text{ \AA}$ , both of them are included in the same cluster, and hence belong to the same complex pore. In this way, all the pores accessible for a water molecule can be detected. Such a pore can be described either as a cluster of the corresponding Delaunay simplices, or as an aggregate of the (usually strongly overlapping) interstitial spheres, or by the list of the surrounding atoms. The largest pores inside the five bare carbon soot models considered are shown in Figure 5.7 as an assemble of empty spheres with radii of at least  $1.4 \text{ \AA}$  (the pore inside the  $S_{COOH}^{II}$  soot particle is not shown here

since it looks almost indistinguishable from that in the  $S^{II}$  particle).

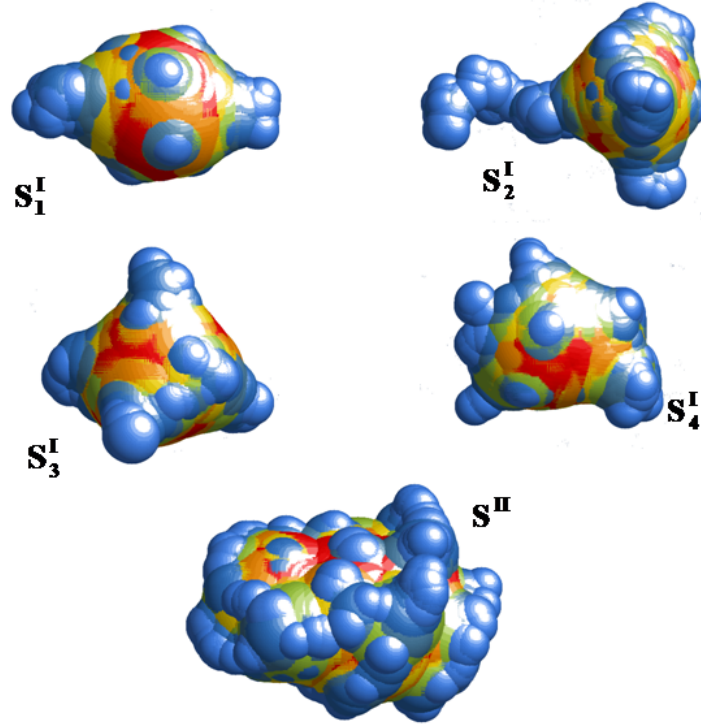


Figure 5.7: The largest pores represented by the combination of empty spheres inscribed into the 5 bare carbon soot particles considered here as is resulted form the Voronoi analysis. Different colours correspond to different radii from blue (smallest one) to red (largest one).

In analysing the morphology of the interatomic pores in our soot models we calculated the following characteristics. The volume of a pore  $V$  is calculated as the sum of the empty volume of the corresponding Delaunay simplices. Pores can also be characterised by the radius of the largest interstitial sphere (simplicial cavity) belonging to them,  $R_{max}$ , and by their length (i.e., the largest distance between two points inside the corresponding aggregate of simplicial cavities),  $L$ . In the pore morphology analysis we take into account only the largest pore in each of the six soot particles considered.

The values of  $V$ ,  $R_{max}$ , and  $L$  corresponding to the different soot models are summarised in Table 5.3. This table also contains the estimated maximum number of water molecules that could be incorporated in the largest pore and in the largest spherical cavity,  $N_{max}$  and  $N_{sp}$ , respectively (assuming the experimental number density of liquid water of  $0.0334 \text{ \AA}^{-3}$ ), and the average number of water molecules found to be adsorbed inside the soot at the highest loading,  $\langle N \rangle_{ads}$ . As is seen, the

pores can, on one hand, always incorporate considerably more water molecules than what would correspond to the volume of their largest simplicial spherical cavity, but, on the other hand, they never contain as much water as what would correspond to their total volume. Instead, even at the highest loading the water content of these pores is just 60–80% of their nominal capacity.

These findings suggest that (i) the water content of the smaller pores is negligible (as even the largest pore is never completely filled), and (ii) similarly to the pores themselves, the shape of the water droplets located inside them is highly non-spherical as well. However, the shape of the water droplet does not necessarily follow strictly that of the pore, as reflected in the difference of the  $\langle N \rangle_{ads}$  and  $N_{max}$  values. Since the main driving force of the water adsorption on soot is found to be the formation of possible new water–water hydrogen bonds, the shape of the water droplet (and hence the number of the water molecules belonging to it) is determined by the requirement that, within the constraints imposed by the pore shape, the hydrogen bonding network of the adsorbed water molecules should be optimal. In particular, narrow and elongated pockets of the pore, where the hydrogen bonding ability of the water molecules is strongly limited by steric factors are likely not to be completely filled.

Soot model	$V / \text{\AA}^3$	$L / \text{\AA}$	$R_{max} / \text{\AA}$	$N_{sp}$	$N_{max}$	$\langle N \rangle_{ads}$
$S_1^I$	803	18.5	4.89	16.3	26.8	19.7
$S_2^I$	1132	22.4	4.73	14.8	37.8	22.8
$S_3^I$	869	15.6	4.69	14.4	29.0	20.8
$S_4^I$	868	17.6	4.48	12.6	29.0	20.2
$S^{II}$	2497	22.2	5.23	20.0	83.4	67.5
$S_{COOH}^{II}$	2478	22.2	5.15	19.1	82.8	64.3

Table 5.3: Properties of the largest pores in the different soot models considered.

This requirement also implies that the more spherical a pore is the more efficiently it can be filled. In order to demonstrate this, we calculated the value of  $\langle N \rangle_{ads}/N_{max}$ , characterising the relative filling of the pores, as a function of the ratio of  $L/R_{max}$  (i.e., that of the linear size of the pore and the radius of its largest spherical cavity), characterising the deviation of the pore shape from the perfect sphere. The obtained data are shown in Figure 5.8. The correlation between  $\langle N \rangle_{ads}/N_{max}$  and  $L/R_{max}$  is clear for both types of soot, indicating that, at least in the case of not too much different pores, more spherical pores can more efficiently be filled by the adsorbed water molecules.

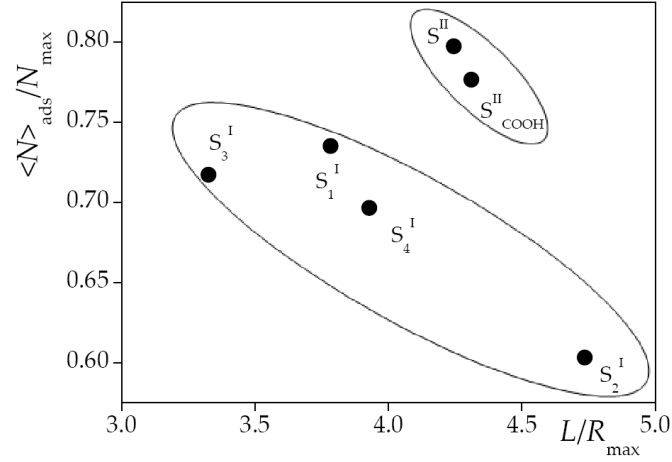


Figure 5.8: Ratio  $\langle N \rangle_{ads}/N_{max}$  between the average number  $\langle N \rangle_{ads}$  of water molecules found to be adsorbed inside the soot at the highest loading and the maximum number  $N_{max}$  of water molecules that could be incorporated in the largest pore of the soot as a function of the ratio  $L/R_{max}$  between the length and the radius of the largest interstitial sphere inside the pores.

### 5.3.4 Energetics of the adsorption

In order to investigate the energetic background of the adsorption in detail we also calculated the distribution of the binding energy of the adsorbed water molecules,  $U_b$  (i.e., their interaction energy with the rest of the system) as well as the contributions coming from the interactions with the soot ball and with the other water molecules,  $U_b^{soot}$  and  $U_b^{wat}$ , respectively, for all the six soot particles considered. Note that we performed these calculations at two chemical potential values corresponding to a low and a high loading of the cavities. The low loading state can be located on the isotherm at slightly below the chemical potential value where water molecules start to occur permanently inside the cavity. High loading corresponded to a system that was somewhat below the condensation, i.e., where the average number of water molecules inside the cavity was maximum. The different chemical potential values corresponding to different loadings for the six systems studied, together with the corresponding average number of water molecules in the cavities are collected in Table 5.4. The obtained  $P(U_b)$ ,  $P(U_b^{soot})$  and  $P(U_b^{wat})$  distributions for the low and high loadings are shown in Figures 5.9 and 5.10 for the type I and II soots, respectively.

In the case of low loadings, the vast majority (i.e., at least 95%) of the adsorbed

Soot model	low loading		high loading	
	$\mu / \text{kJ mol}^{-1}$	$\langle N_{inside} \rangle$	$\mu / \text{kJ mol}^{-1}$	$\langle N_{inside} \rangle$
$S_1^I$	-46.03	0.72	-41.09	19.7
$S_2^I$	-46.52	0.064	-40.35	22.3
$S_3^I$	-46.52	1.39	-40.60	20.8
$S_4^I$	-46.03	0.042	-41.09	20.2
$S^{II}$	-43.04	1.05	-41.07	67.5
$S_{COOH}^{II}$	-44.03	2.32	-41.56	64.3

Table 5.4: Chemical potential values and the average number of water molecules inside the cavity both corresponding to the low and high loading of the six soot particles studied.

water molecules are located in the vapour phase, being isolated from each other as well as from the soot ball. This is reflected in the high and narrow peak of the  $P(U_b)$ ,  $P(U_b^{soot})$  and  $P(U_b^{wat})$  distributions at zero energy. In the case of the bare carbon soots the energy of interaction of the few adsorbed water molecules with the soot ball turns out to be around  $-10 \text{ kJ mol}^{-1}$ . In the case of the  $S_1^I$  soot ball the peak of the  $P(U_b^{soot})$  distribution is located at somewhat lower energies (i.e., around  $-11 \text{ kJ mol}^{-1}$ ) than for the other type I soots, where this value is always around  $-8.5 \text{ kJ mol}^{-1}$  (see the inset of Figure 5.9a). This difference is in accordance with our previous finding that adsorption on the  $S_1^I$  soot starts at somewhat lower chemical potentials (pressures) than that on the other type I soot balls (see Figure 5.4), and stresses again the role of the optimal location of the first adsorbed water molecules in the adsorption process. It should be recalled that among the type I soots  $S_1^I$  contains far the largest number of C atoms, which is likely to be related with its ability of more easily binding the first few water molecules than the other type I soots.

It is also seen from Figure 5.9a that in the case of the  $S_1^I$  and  $S_3^I$  soots, which contain a much larger amount of water at the selected chemical potential than either  $S_2^I$  or  $S_4^I$  (see Table 5.4), the  $P(U_b^{soot})$  distribution already exhibits a shoulder at its high energy side, around  $-5 \text{ kJ mol}^{-1}$ . This shoulder reflects the presence of water molecules that are weakly bound to the soot, as they are already bound by the other adsorbed water molecules rather than by the soot ball itself. Correspondingly, the  $P(U_b^{wat})$  distribution of these soots shows a peak around  $-20 \text{ kJ mol}^{-1}$  and another one between  $-45$  and  $-60 \text{ kJ mol}^{-1}$ . The former peak corresponds to waters with one, whereas the latter one to waters with two or three hydrogen bonded neighbors. It should also be noted that traces of the peak around  $-20 \text{ kJ mol}^{-1}$  already appear on the  $P(U_b^{wat})$  distribution of the  $S_2^I$  soot, clearly demonstrating that the main

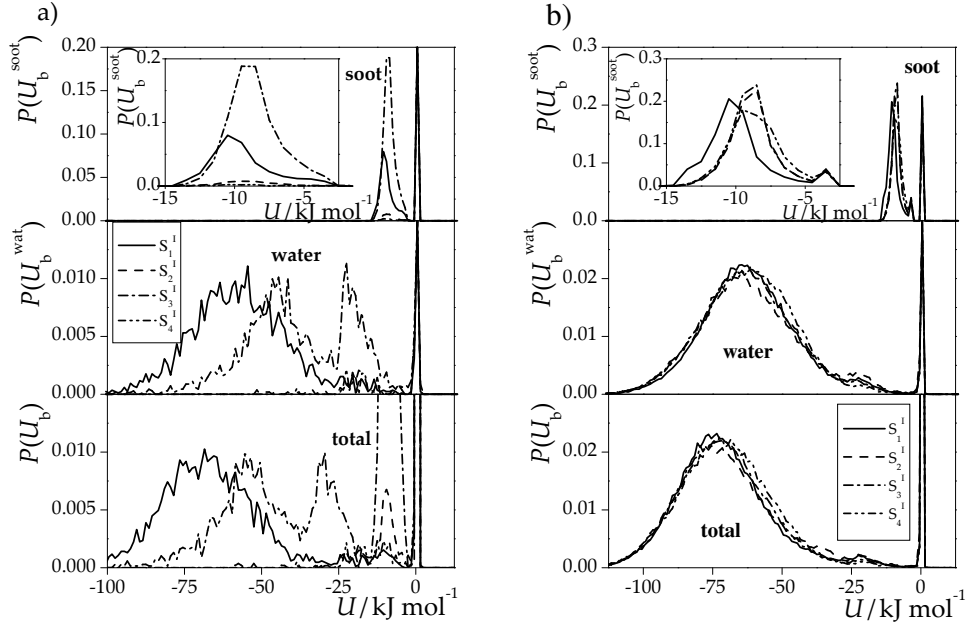


Figure 5.9: Distributions of the total binding energy of the water molecules ( $P(U_b)$ ) and of the contributions coming from the interaction with the soot ball ( $P(U_b^{soot})$ ) and with the other water molecules ( $P(U_b^{wat})$ ) in the case of the  $S_1^I$  (full line),  $S_2^I$  (dashed curve),  $S_3^I$  (dashed dotted line),  $S_4^I$  (dashed dotted dotted line) soot at (a) low and (b) high loadings.

driving force of the water adsorption on soot is the possibility of the formation of new water–water hydrogen bonds with the already adsorbed water molecules.

The  $P(U_b^{soot})$  distributions of the type I soots obtained at high loading (Figure 5.9b) are rather similar to those corresponding to low loading. It should be noted that now the majority (i.e., more than 80%) of the water molecules have interaction energy of roughly  $-10$   $\text{kJ mol}^{-1}$  with the soot ball. This finding reflects the relatively small size of the largest pore of these soot balls, as even at high loading the majority of the adsorbed water molecules is still in contact with the wall of the pore. The  $P(U_b^{wat})$  distribution exhibits a single, broad peak around  $-63$   $\text{kJ mol}^{-1}$ , indicating that the adsorbed water molecules form, on average, three hydrogen bonds with each other. The peak of the total binding energy distribution appears at  $-72$   $\text{kJ mol}^{-1}$ , which agrees almost perfectly with the sum of the peak positions of the  $P(U_b^{soot})$  and  $P(U_b^{wat})$  distributions.

The distributions corresponding to the bare carbon  $S^{II}$  soot ball show rather similar characteristics with those of the type I soot. At low loading (see Figure 5.10a and Table 5.4) the interaction energy of the adsorbed water molecules with the soot

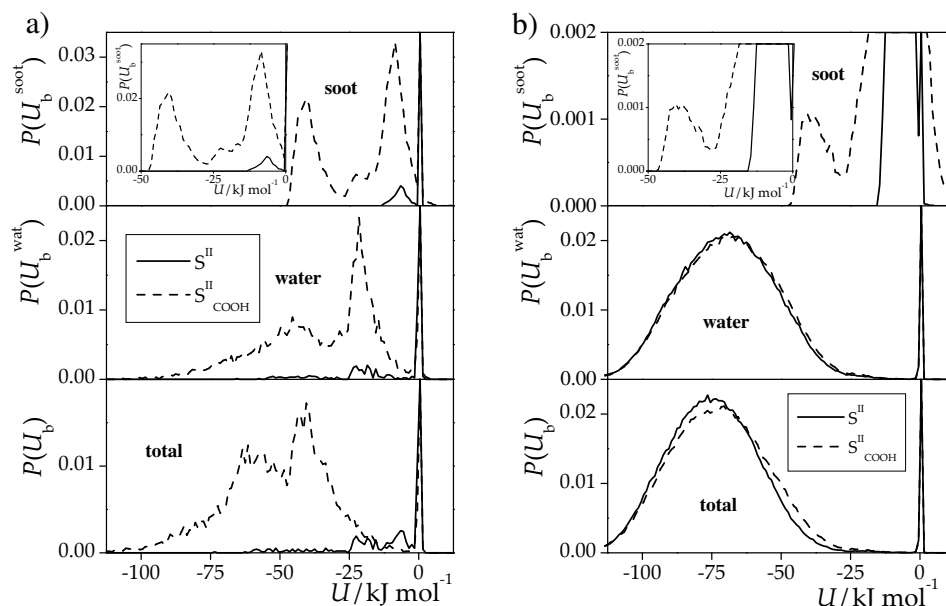


Figure 5.10: Same as Figure 5.9 for the  $S^{II}$  (full line) and  $S^{II}_{COOH}$  (dashed curve) soot.

ball has a peak at  $-6.5 \text{ kJ mol}^{-1}$ , reflecting the larger size of this pore, and hence the smaller curvature of its wall than that of the pores in the type I soots. The  $P(U_b^{wat})$  distribution shows a peak at  $-20 \text{ kJ mol}^{-1}$ , corresponding to the water molecules with one hydrogen bonded neighbour, and also traces of a small peak around  $-40 \text{ kJ mol}^{-1}$ , reflecting already the presence of a few water molecules with two hydrogen bonded neighbours.

In the case of the  $S^{II}_{COOH}$  soot, however, the picture is rather different, at least at low loading (Figure 5.10a). Here the  $P(U_b^{soot})$  distribution is bimodal, having a peak at  $-40 \text{ kJ mol}^{-1}$  and another one at  $-8 \text{ kJ mol}^{-1}$ . The first peak reflects the water molecules double hydrogen bonded to the COOH group, whereas the second peak corresponds to water molecules forming no hydrogen bond with this group, but interacting with the nearby C atoms of the pore wall. These waters are already hydrogen bonded to other waters, as reflected in the peaks of the  $P(U_b^{wat})$  distribution at  $-21 \text{ kJ mol}^{-1}$  and  $-45 \text{ kJ mol}^{-1}$ , given by waters with one and with two hydrogen bonded neighbours, respectively. The peaks of the  $P(U_b)$  total binding energy distribution, appearing around  $-60$  and  $-40 \text{ kJ mol}^{-1}$  indicate that the adsorbed water molecules form either two or three hydrogen bonds with their neighbors. In the light of our previous finding we can conclude that in the former case both hydrogen bonds are typically formed with another water molecule, whereas in the latter case two hydrogen bonds are formed with the COOH group and the third one with a water molecule.

The differences between the bare carbon  $S^{II}$  and the COOH-containing  $S_{COOH}^{II}$  soots, however, disappear at high loading (see Figure 5.10b), in accordance with our previous finding that the role of the polar COOH group is limited to the initiation of the adsorption at low pressures. Here, the amplitude of the peak of the  $P(U_b^{soot})$  distribution of the  $S_{COOH}^{II}$  soot at  $-40 \text{ kJ mol}^{-1}$  is an order of magnitude smaller than that at low loading, as hydrogen bonding with the COOH group now involves only a small minority of the adsorbed water molecules. Further, the majority of the waters (also not such a large fraction as in the case of the type I soots) are still in contact with the pore wall, and they form, on average, three hydrogen bonds with each other, irrespective of whether the soot contains a polar COOH group or not.

## 5.4 Conclusions

In this chapter we have presented a study on the adsorption process of water on chemically stable model soot particles by means of the grand canonical Monte Carlo method, and related the characteristics of the pores inside the soot ball with their adsorption ability. The obtained results clearly show that the main driving force of water adsorption on soot is the formation of new possible hydrogen bonds with the already adsorbed water molecules. We found that there are two important factors influencing the adsorption ability of soot. The first of these factors is the ability of the soot of accommodating the first adsorbed water molecules. Since the presence of these molecules initiates the adsorption of other waters, the stronger these first water molecules can be bound by the soot, the earlier starts the adsorption. This can be achieved when strong hydrophilic sites are present in the soot. Furthermore, higher soot density may also result in the enhanced affinity of water molecules for being accommodated in soot cavities.

The other factor concerns morphological characteristics, primarily size and shape of the pores. In general, adsorbing pores should be such that the hydrogen bonding network of the water molecules filling them should be optimal. It turned out that this requirement practically means that water molecules should be able to form, on average, at least three hydrogen bonds with each other. This implies that too small pores as well as narrow and deep pockets of the larger pores are not filled with water even at high pressures. Although the adsorbed water droplet is found not to be spherical, it turned out that, in general, more spherical pores can be more efficiently filled with water at high loading.

It is also clear that the size of the pores is a crucial factor of the adsorption.

Thus, smaller pores meet better with the first criterion, as the first adsorbed water molecules can interact stronger with the nearby C atoms of the soot in a small pore of highly curved wall. On the other hand, such pores satisfy less the second criterion, as the hydrogen bonding network of water filling smaller pores is more strongly restricted by steric factors. Our results thus suggest that there might be an optimal range of pore sizes in soots which corresponds to the best water adsorption ability of the soot, i.e., when it is able to bind a noticeable amount of water even at rather low pressures.

Note that although we investigated only soot micropores in our study, the results allow us to extend our conclusions to the interpretation of the stepwise structure of an experimental isotherm obtained on kerosene soot (see Figure 2.3). The distinct steps can thus be attributed to the gradual filling-up of the adsorption sites (pores and pockets) being characterised (as we have seen from this study) by either different size and shape or different amount of oxygenated functional (mainly COOH) groups. Note that such a comparative GCMC study may reveal a lot of details of such a complex process like the adsorption of water molecules on soot.

## Chapter 6

# Reactivity of soot particles

### 6.1 Introduction

In this chapter we present results concerning the effect of soot particles on the atmospheric oxidation reaction of PAHs by OH. PAH molecules have a high affinity for carbonaceous materials, thus the adsorption of PAHs on soot may influence their abundance in the gas phase, and also their atmospheric chemistry[147].

Soot particles are difficult to characterise from a physico-chemical point of view, as we have seen in Section 2.4.2. Their structure may be very diverse, their surface may be oxidised to a certain extent, and they might be associated with organic and inorganic materials at their surface. These result in the fact that soot is not a well-defined chemical substance[148]. As a consequence, studies of the physico-chemistry of PAHs on soot surfaces are very scarce.

Up to now, there have only been a limited number of controlled laboratory[149, 150] or field [151, 152] studies on the adsorption of PAHs onto soot, and, to our best knowledge, there is only one paper devoted to the experimental study of the uptake of aromatic hydrocarbons onto soot with a known surface area, as a function of temperature and partial pressure[11]. In their study, Esteve et al.[153] characterised the role of OH, NO<sub>2</sub> and NO radicals on the reactivity of 11 polyaromatic compounds adsorbed on graphite particles chosen as a model of atmospheric carbonaceous particles. In this study, all PAHs presented similar rate constants while reacting with OH, and, compared to the reactivity in the gas phase, the heterogeneous reaction with OH radicals seems to show a potential inhibiting effect of the graphite surface, meaning that the mechanisms may be sensibly different[153].

Only a few theoretical studies have been devoted to the structural and energetic

characterisation of the interactions between PAHs and carbonaceous surfaces like soot, primarily due to the fact that these systems are too large for tractable ab initio calculations. Indeed, a realistic theoretical simulation of intermolecular forces requires high-level electronic quantum calculations to account for dispersion effects. The term ‘high-level quantum calculation’ refers to the use of very large basis sets and a precise description of the correlation energy. Even for a simple perturbative approach, double excitations on two interacting molecules are necessary to mimic dispersion effects. Large basis sets are also necessary to minimise both the basis set convergence error and the basis set superposition error. Such high-level calculations require a great amount of computational resources[154], and, as a consequence, they can only be done for small systems, such as the benzene dimer[155].

Gonzalez and co-workers[156, 157] proposed a method called the Hartree-Fock Dispersion model (HFD) to calculate the structure and binding energy of aromatic clusters, following the work originally proposed by Hepburn et al.[158]. In this HFD method, the calculation of the intermolecular energies combines an ab initio self-consistent field (SCF) interaction energy with an empirical dispersion energy term described by the London theory that provides a very efficient analytical approach to account for dispersion effect[156]. The method was successfully used to describe dimers of benzene, naphthalene, anthracene and pyrene, as well as the naphthalene trimer[157]. However, even this simplified method is unable to handle large soot/PAH systems.

Collignon et al. have developed a new method[159, 160], which is applicable for large systems. The so-called semi-empirical-dispersion (SE-D) method, combines the semi-empirical description of the electrostatic and induction interactions with a sum of two-body London dispersion terms proportional to  $R^{-6}$  ( $R$  being the distance)[159].

In my work, this new method was used to describe the interaction between a PAH molecule and soot. This latter was replaced by a model particle as it is simpler and better characterised than real soot. The model particle was chosen to be a large graphene-like molecule consisting of fused benzene rings and having hydrogens only at the boundaries to eliminate free valences. It should be noted that a real soot surface is likely oxidised, and hence contains oxygenated functional groups, which may influence the chemistry of PAH molecules. But, as a first step, a large, flat and perfect carbonaceous surface was studied.

To investigate the oxidation reaction of benzene, naphthalene and anthracene by OH radical in the gas phase as compared to that occurring on a graphene surface, I used a new kinetic–statistical approach aiming at catching the differences between

the reactions taking place in the two phases. These oxidation reactions are known to have a negative activation barrier, i.e., the transition state can be characterised by a lower energy value relative to the separated reactants. The oxidation reaction of a PAH molecule by OH is illustrated by the reaction scheme given in Figure 6.1.

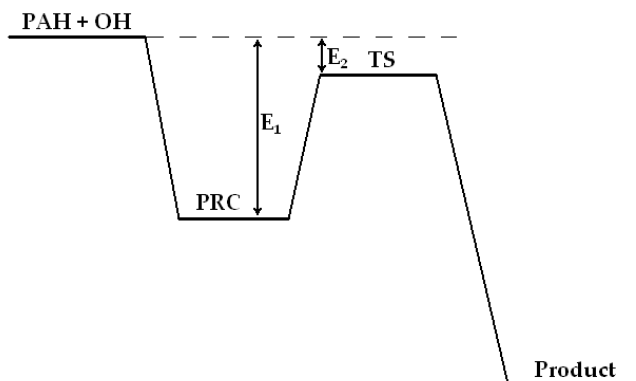


Figure 6.1: Schematic of the oxidation reaction of PAH molecules by OH radical. The energy of the reactants (PAH + OH) is taken as the reference state for the definition of the energies. PRC and TS define the pre-reactive complex and the transition state respectively.

## 6.2 The SE-D method

In this model, an analytical term is added to a semi-empirical description of the electrostatic interactions to account for dispersion forces in the calculation of the total energy, which is thus written as

$$U_{\text{SE-D}} = U_{\text{SE}} + f \times U_{\text{D}}, \quad (6.1)$$

where  $U_{\text{SE}}$  is the semi-empirical energy calculated at the AM1[61], PM3[63], or MNDO[62] level of theory,  $U_{\text{D}}$  is the dispersion energy, and  $f$  is a damping function used to avoid singularities in the dispersion term at short intermolecular distances. Note that these semi-empirical methods are proposed to reproduce, within a given average accuracy, molecular geometries, heats of formation and some other thermodynamical data. These quantities are related mainly to chemical forces that are responsible for bond energies. However, due to the reduced basis set used, it is impossible to reproduce a long-range quantum effect, such as dispersion. It is already almost impossible to do it with even a ‘reasonably good’ ab initio approach. On

the contrary, long-range electrostatic and induction effects are included in a more or less realistic way in the calculations by the SCF procedure itself. It turns out that the introduction of a sum of  $R^{-6}$  terms added at long distance to the SCF energy appears as an elegant way to include dispersion, even if it requires some ‘savoir-faire’ for the estimation of these terms.

The dispersion contribution to the total energy is thus expressed as[161]

$$f \times U_D = - \sum_{i=1}^{N_g} \sum_{j=1}^{N_p} \frac{1}{(1 + e^{\alpha(R_0 - R_{ij})})} \times \frac{[C_i^{(6)} C_j^{(6)}]^{1/2}}{R_{ij}^6}, \quad (6.2)$$

where  $N_g$  and  $N_p$  are the total number of atoms on the carbonaceous surface and in the PAH molecule considered, respectively.  $R_{ij}$  is the interatomic distance between a surface atom  $i$  and the  $j$ th atom of the PAH molecule, and  $C^{(6)}$  represents the two-body dispersion coefficients used to calculate the C–C, C–H and H–H interactions. The damping function  $f(R_{ij})$  has the two-parameter hyperbolic tangent function form proposed by Gonzales et al.[156, 157], in which  $\alpha$  and  $R_0$  are two empirical parameters that control the behaviour of the damping function, and thus of the dispersion interaction, as a function of the interatomic distances  $R_{ij}$ .

The dispersion parameters  $\alpha$ ,  $R_0$ , and  $C_j^{(6)}$  of the SE-D approach were fitted for the combination with a semi-empirical calculation of the SCF contribution to the interaction energy. The adjustment was performed on a set of ab initio and experimental results for 22 PAH dimers and mixed complexes, aiming at defining a transferable interaction potential for the calculations of dispersion energy between aromatic molecules and large graphene clusters[159]. Here, we chose the transferable SE-D parameter set suitable for use with the semi-empirical AM1 method because it proved to give slightly more reliable results[159]. However, the present study is not limited to the calculation of the interaction between PAHs and soot surface because it aims also at characterising the oxidation of the adsorbed PAHs by the OH radical. We thus extend the SE-D method to the calculations of the OH – PAH and OH – soot interactions, which are then written as

$$U_{AM1-D}^{OH} = U_{AM1}^{OH} - \sum_{i=1}^N \frac{1}{(1 + e^{\alpha^{OH}(R_0^{OH} - R_{iO})})} \times \frac{[C_{O,i}^{(6)}]}{R_{iO}^6}, \quad (6.3)$$

where the semi-empirical calculations are performed at the AM1 level for the consistency with the calculations of the PAH – soot interactions. The sum over  $i$  includes the total number  $N$  of carbon atoms in the system considered (soot + PAH), and the  $C_{O,i}^{(6)}$  parameter for the oxygen – carbon interactions is taken from the literature[162].

Note that all the hydrogen atoms are neglected in the calculations of the OH – soot and OH – PAH interactions.

The determination of the best values for the  $\alpha^{\text{OH}}$  and  $R_0^{\text{OH}}$  parameters of the damping function proved to be quite a delicate task, and it was performed in the following way. We performed AM1 calculations to characterise the pre-reactive complex (PRC) and the transition state (TS) corresponding to the oxidation reactions of PAH molecules by OH in the gas phase. For benzene, the results show that the equilibrium distance for the PRC is larger than 3.0 Å, and that the equilibrium distance for the corresponding TS is equal to 2.08 Å. To set up our SE-D model, we can thus reasonably think that the dispersion interactions between the incoming OH and the reacting benzene molecule play a significant role above 3.0 Å only, and should vanish between 2.1 and 3.0 Å. This led us to choose a  $R_0$  value equal to 2.75 Å for the O–C interactions in the OH–benzene system. The corresponding value of the  $\alpha$  parameter ( $\alpha = 64.00$ ) was chosen accordingly, to ensure a smooth disappearance of the dispersion interactions between 2.0 and 3.0 Å [160].

Similar procedure was performed for naphthalene and anthracene, thus the corresponding parameter values were  $R_0 = 2.95$  Å and  $\alpha = 16.00$  for both molecules. Note that the  $R_0$  values defined here are in agreement with values previously fitted in the literature on the basis of DFT calculations[163]. Note also that we will assume in the following that the parameters selected here for the O–C dispersion interactions are transferable to the calculations of the interactions between OH and soot. All the parameters used in the present calculations are given in Table 6.1.

	benzene	other PAHs
$C_{\text{C}}^{(6)}$	2207.94	2207.94
$C_{\text{H}}^{(6)}$	48.6	48.6
$C_{\text{OC}}^{(6)}$	1923.51	1923.51
$\alpha$	3.96	3.96
$R_0$	2.68	2.68
$\alpha^{\text{OH}}$	64.00	16.00
$R_0^{\text{OH}}$	2.75	2.95

Table 6.1: Selected parameters for the dispersion contribution to the SE-D potential calculated with the semi-empirical AM1 method. The parameters  $C_{\text{C}}^{(6)}$ ,  $C_{\text{H}}^{(6)}$ , and  $C_{\text{OC}}^{(6)}$  are given in  $\text{kJ mol}^{-1} \text{Å}^6$ , whereas  $\alpha$  is given in  $\text{Å}^{-1}$  and  $R_0$  in Å.

It is worth mentioning that such an approach that aims at describing intermolecular interactions in large carbonaceous systems on the basis of semi-empirical

calculations shows similarities with methods recently developed to improve the semi-empirical description of other systems for which refined quantum calculations are too costly. For example, electrostatic and dispersion corrections have been brought to the AM1 or PM3 semi-empirical energy to reproduce correctly the long-range behaviour of the interaction potential in hydrogen bonded systems[164, 165, 166]. Similarly, an atom-atom pairwise additive dispersion potential has also been recently added to a semi-empirical description of the intermolecular interactions in biomolecules[167]. Furthermore, in the novel version of Gaussian program package (Gaussian 09) a functional is now available for DFT + dispersion calculations. This functional seems suitable for calculations involving carbon and hydrogen atoms. However, it fails in describing systems containing O atoms[168].

## 6.3 The elements of our new method

### 6.3.1 Kinetic model

The kinetics of the oxidation mechanism presented in Figure 6.1 is governed by rate constants corresponding to the separate elementary reaction steps. The two first steps, schematised as



correspond to the formation of the (possibly excited) PRC, characterised by the rate constant  $k_1$ , and to the decay of the PRC to the reactants, governed by the rate constant  $k_{-1}$ . Then, the formation of the product through the transition state is characterised by the rate constant  $k_2$  as



Finally, it should be taken into account that the PRC can be quenched by collisions with neutral particles as



This quenching step is characterised by the second order rate constant  $k_3$  and M may be any neutral particle that does not experience any chemical transformation during the collision.

Then the global reaction rate for the oxidation process (i.e., the reaction rate for the formation of the product from the reactants) can be written in the following form:

$$r = \frac{d[\text{Product}]}{dt} = k_2[\text{PRC}] = k[\text{OH}][\text{PAH}]. \quad (6.7)$$

If we assume now that the PRC is in a quasi-steady state, one may write

$$\frac{d[\text{PRC}]}{dt} = k_1[\text{OH}][\text{PAH}] - (k_{-1} + k_2 + k_3[\text{M}])[\text{PRC}] = 0. \quad (6.8)$$

This leads to the expression

$$[\text{PRC}] = \frac{k_1}{k_{-1} + k_2 + k_3[\text{M}]}[\text{OH}][\text{PAH}], \quad (6.9)$$

and thus the total rate constant is expressed as

$$k = \frac{k_1 k_2}{k_{-1} + k_2 + k_3[\text{M}]}. \quad (6.10)$$

We can make now two additional assumptions. First, we consider the existence of an equilibrium between the reactants and the PRC, thus the decay of the PRC to reactants is much faster than the formation of the product, i.e.,

$$k_{-1} \gg k_2. \quad (6.11)$$

Moreover, under tropospheric conditions the pressure is low enough so that the collisions with neutral particles are considerably rare events. We can thus assume that

$$k_2 \gg k_3[\text{M}]. \quad (6.12)$$

Finally, for the total rate constant, we obtain

$$k = k_2 \frac{k_1}{k_{-1}} = k_2 K, \quad (6.13)$$

where  $K$  is the equilibrium constant of the formation of the PRC. Note that we arrive at an expression similar to the one proposed by Atkinson and Cvetanović for the characterisation of the addition of O atoms to olefins[169].

### 6.3.2 Statistical model

The canonical equilibrium constant  $K$  for a gas-phase process is given by

$$K = \frac{Q_{PRC}}{Q_{PAH}Q_{OH}} e^{-E_1/k_B T}, \quad (6.14)$$

where  $E_1$  is the energy of the PRC with respect to the reference state (PAH + OH at an infinite distance from each other),  $T$  is the absolute temperature,  $k_B$  is the Boltzmann constant, and  $Q_{PRC}$ ,  $Q_{PAH}$  and  $Q_{OH}$  are the partition functions of the pre-reactive complex, the polycyclic aromatic hydrocarbon and the OH radical, respectively.

The reaction constant for the formation of the product according to the transition state theory (TST) is expressed as

$$k_2 = \frac{k_B T}{h} \frac{Q^\ddagger}{Q_{PRC}} e^{-(E_2 - E_1)/k_B T}, \quad (6.15)$$

where  $h$  is the Planck constant,  $E_2$  is the energy of the transition state with respect to the reference state and  $Q^\ddagger$  is the partition function of the transition state. According to Eq 6.13, the product of Eq 6.14 and 6.15 gives the total rate constant  $k$

$$k = \frac{k_B T}{h} \frac{Q^\ddagger}{Q_{PAH}Q_{OH}} e^{-E_2/k_B T}, \quad (6.16)$$

an expression in which  $E_1$  no longer appears.

Because we are interested here in the modification of the rate constant  $k$  upon physisorption of the PAH on a carbonaceous particle modelling a soot surface, we rather choose to evaluate the ratio of the total rate constant of the oxidation in the adsorbed phase to the one associated with the oxidation in the gas phase, as

$$\frac{k^{ads}}{k^{gas}} = \frac{Q_{PAH}^{gas} Q_{OH}^{gas} Q^{\ddagger,ads}}{Q_{PAH}^{ads} Q_{OH}^{ads} Q^{\ddagger,gas}} e^{\frac{-(E_2^{ads} - E_2^{gas})}{k_B T}}. \quad (6.17)$$

Before calculating the different partition functions in Eq 6.17, we characterised separately the various motions of the benzene molecule and of the TS in the gas phase and on the soot surface.

As an illustration of the corresponding results, we give in Figure 6.2 the energy curves obtained upon rotating the adsorbed benzene molecule around the  $z$  axis, perpendicular to the surface of a  $C_{80}H_{22}$  cluster modelling soot surface (Figure 6.2a)

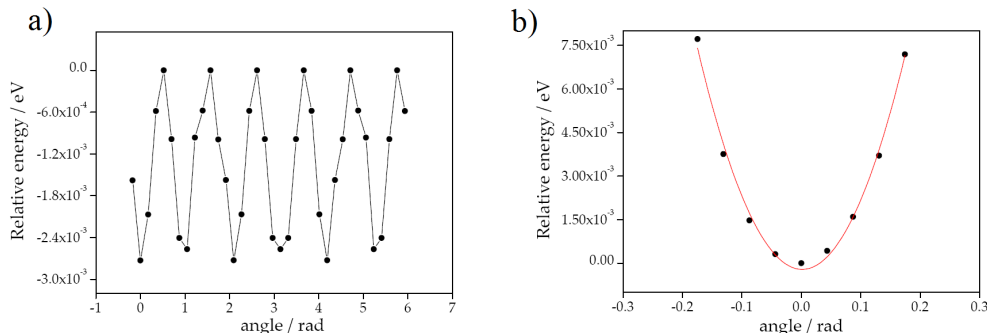


Figure 6.2: Energy curves obtained upon rotating an adsorbed benzene molecule (a) around the  $z$  axis perpendicular to the surface of a  $C_{80}H_{22}$  cluster modelling soot and (b) around an axis parallel to this surface. Note that the relative energy (in eV) is defined with respect to the maximum or the minimum of the energy curve. The angles are given in radian.

and around the  $x$  axis parallel to this surface (Figure 6.2b). The energy barriers for the rotational motion around the  $z$  axis (Figure 6.2a) are three times smaller than the  $k_B T$  value at room temperature, and, as a consequence, this rotational motion can be considered as a free rotation in our calculations. Similarly, the rotation of naphthalene and anthracene around the  $z$  axis can also be regarded as a free rotation.

In a similar way, Figure 6.2b shows that the energy variations upon slightly tilting the admolecule around the  $x$  axis can be easily represented by considering the admolecule as a 1D harmonic oscillator. In fact, this detailed study shows that all the various motions of the adsorbed benzene molecule and TS can be described, in a first approach, either by free motions as in gas phase or by the rigid rotor and harmonic oscillator approximations. This leads to the following assumptions:

- the translational partition functions in the directions which are parallel to the graphene surface (direction  $x$  and  $y$ ) are the same in the adsorbed phase and in the gas phase, due to the very weak interaction potential corrugation of the cluster surface;
- for the same reason, the rotation around the  $z$  axis in the adsorbed phase can be approximated by a free rotor;
- by contrast, the translation in the  $z$  direction (i.e., perpendicular to the surface) as well as the rotations around the  $x$  and  $y$  axes are hindered due to the presence of the cluster surface and have to be treated as vibrational motions.
- the OH radical can be considered as coming from the gas phase even for the reaction taking place in the adsorbed phase (i.e., the OH radical arrives perpen-

dicularly to the cluster surface). Indeed, preliminary calculations showed that the OH radical is captured by the cluster when arriving parallel to its surface, thus the oxidation reaction cannot take place[160].

- the internal vibrational modes and the electronic states are the same in the adsorbed phase and in the gas phase for the benzene molecule and for the TS, because of the weak interaction with the soot surface characterising a physisorption process.

Using these assumptions, it turns out that the partition function ratios become

$$\frac{Q_{PAH}^{gas}}{Q_{PAH}^{ads}} = \frac{Q_{trans,z}^{gas,PAH}}{Q_{tr_z \rightarrow vibr}^{ads,PAH}} \frac{Q_{rot}^{gas,PAH}}{Q_{rot_x \rightarrow vibr}^{ads,PAH} Q_{rot_y \rightarrow vibr}^{ads,PAH} Q_{rot_z}^{ads,PAH}}, \quad (6.18)$$

and

$$\frac{Q_{\ddagger,ads}^{\ddagger}}{Q_{\ddagger,gas}^{\ddagger}} = \frac{Q_{tr_z \rightarrow vibr}^{\ddagger,ads}}{Q_{tr_z \rightarrow vibr}^{\ddagger,gas}} \frac{Q_{rot_x \rightarrow vibr}^{\ddagger,ads}}{Q_{rot_x \rightarrow vibr}^{\ddagger,gas}} \frac{Q_{rot_y \rightarrow vibr}^{\ddagger,ads}}{Q_{rot_y \rightarrow vibr}^{\ddagger,gas}} \frac{Q_{rot_z}^{\ddagger,ads}}{Q_{rot_z}^{\ddagger,gas}}. \quad (6.19)$$

Finally, substituting the above equations into Eq 6.17, we arrive at the following expression of the rate constants ratio:

$$\begin{aligned} \frac{k_{ads}}{k_{gas}} &= \frac{Q_{trans,z}^{gas,PAH}}{Q_{tr_z \rightarrow vibr}^{ads,PAH}} \frac{Q_{rot}^{gas,PAH}}{Q_{rot_x \rightarrow vibr}^{ads,PAH} Q_{rot_y \rightarrow vibr}^{ads,PAH} Q_{rot_z}^{ads,PAH}} \\ &\times \frac{Q_{tr_z \rightarrow vibr}^{\ddagger,ads}}{Q_{tr_z \rightarrow vibr}^{\ddagger,gas}} \frac{Q_{rot_x \rightarrow vibr}^{\ddagger,ads}}{Q_{rot_x \rightarrow vibr}^{\ddagger,gas}} \frac{Q_{rot_y \rightarrow vibr}^{\ddagger,ads}}{Q_{rot_y \rightarrow vibr}^{\ddagger,gas}} \frac{Q_{rot_z}^{\ddagger,ads}}{Q_{rot_z}^{\ddagger,gas}} e^{\frac{-(E_2^{ads} - E_2^{gas})}{k_B T}}, \end{aligned} \quad (6.20)$$

where the following analytical expressions valid for 1D and 3D rotations, 1D translation and 1D harmonic vibration, respectively, can be used for the calculations of the partition functions:

$$Q_{rot}^{1D} = \frac{1}{\sigma} \sqrt{\frac{8\pi k_B T}{\hbar^2}} I, \quad (6.21)$$

$$Q_{rot}^{3D} = \frac{8\pi^2}{\sigma} \left( \frac{k_B T}{2\pi \hbar^2} \right)^{\frac{3}{2}} \sqrt{I_1 I_2 I_3}, \quad (6.22)$$

$$Q_{transl}^{1D} = L \sqrt{\frac{m k_B T}{2\pi \hbar^2}}, \quad (6.23)$$

$$Q_{vibr} = \frac{1}{1 - e^{\frac{-h\nu}{k_B T}}}. \quad (6.24)$$

In the above equations  $\hbar$  is the Planck constant divided by  $2\pi$ ,  $\nu$  is the vibrational frequency,  $\sigma$  is the symmetry number of the rotation,  $L$  is the finite distance (of arbitrarily large extension) along which the molecule of mass  $m$  is permitted to move,  $I$  is a 1D moment of inertia associated with the rotation axis defined in Eq 6.21, and  $I_1, I_2, I_3$  are the three moments of inertia of a 3D rotor.

To obtain the vibrational frequencies of the various hindered rotational motions we tilted the given molecule around its equilibrium position. The tilts are performed by small angles around the  $x$  and  $y$  axes parallel to the soot surface and we simply calculated the energy in the tilted positions (but we did not optimise it). Then, the obtained energy values were fitted by a quadratic function (see Figure 6.2b):

$$E_{pot} = \frac{1}{2}k(x - x_0)^2 + a, \quad (6.25)$$

in which  $x$  denotes the tilt angle. The force constant  $k$  was then used for determining the frequency:

$$\nu = \frac{1}{2\pi} \sqrt{\frac{k}{I}}, \quad (6.26)$$

where  $I$  is the corresponding moment of inertia.

A similar procedure was repeated for the vibrational motion (i.e., hindered translational motion) along the  $z$  axis, but by replacing the moment of inertia by the mass of the admolecule in Eq 6.26.

The moment of inertia in the adsorbed phase was calculated around an axis perpendicular to the surface and passing through the center of mass of the admolecule. Note that this axis was considered as the  $z$  axis in our calculations.

## 6.4 Results

As a first application, we investigated the details of the heterogeneous oxidation reaction of benzene, naphthalene and anthracene adsorbed on a soot particle modelled by either a  $C_{80}H_{22}$  or a  $C_{150}H_{30}$  cluster, depending on the size of the adsorbed PAH molecule. To perform all energy calculations we used the Ampac 8 program package[170] that was modified to include the determination of the dispersion term.

Energies were calculated at the AM1-D level of theory. As an illustration, Figure 6.3 shows the three PAH molecules adsorbed on the graphene surface.

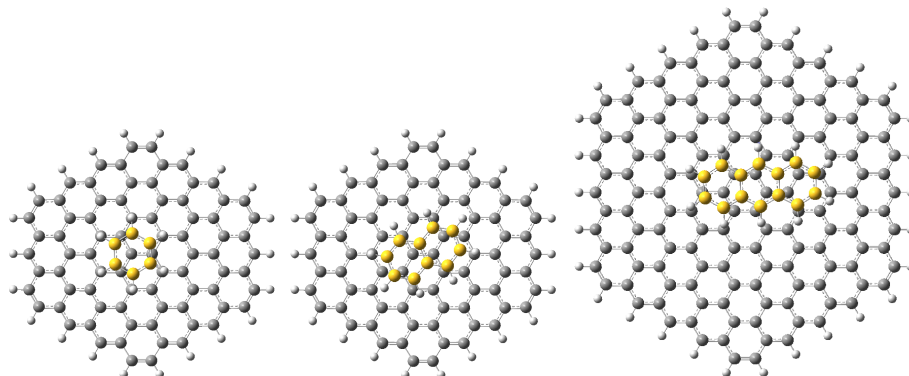


Figure 6.3: Optimised positions of the three PAH molecules studied, such as (from left to right): benzene, naphthalene both on the  $C_{80}H_{22}$  cluster, and anthracene on the  $C_{150}H_{30}$  cluster. The carbon atoms of the PAH molecules are marked by yellow.

Due to the symmetry of the PAH molecules studied, one can distinguish two transition states in the case of naphthalene (denoted as 1 and 2) and three in the case of anthracene (marked by 1, 2 and 9), whereas benzene has only one transition state. The numbering of the possible transition states of naphthalene and anthracene are illustrated in Figure 6.4. The different constants describing the different motions of the PAH molecules and of their transition states are collected in Table 6.2, Table 6.4, and Table 6.6 in the case of benzene, naphthalene, and anthracene, respectively. The resulting partition functions as well as the  $E_2$  energy values corresponding to the different transition states are presented in Table 6.3 (benzene), Table 6.5 (naphthalene) and Table 6.7 (anthracene). All partition functions are evaluated at 298 K.

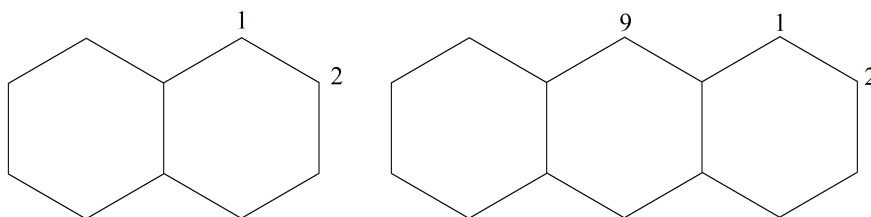


Figure 6.4: The numbering of the possible transition states of naphthalene (left) and anthracene (right).

First of all, by comparing the energy values obtained in the gas phase with those calculated at the graphene surface, we can see that the TSs are stabilised by adsorption, i.e., the  $E_2$  values are lower at the surface than in the gas phase. Then the values given in Tables 6.2–6.7 can be used in Eq 6.20 to obtain the  $\frac{k^{ads}}{k^{gas}}$  ratios,

Benzene		PAH	TS
Gas phase	Translation	$M = 1.29$	$M = 1.58$
	Rotation	$I_1 = 29.5$	$I_1 = 41.2$
		$I_2 = 14.8$	$I_2 = 32.1$
		$I_3 = 14.8$	$I_3 = 20.8$
		$\sigma = 12$	$\sigma = 1$
Adsorbed phase	Transl $\rightarrow$ Vibr	$M = 1.29$	$M = 1.58$
	Rot <sub>x</sub> $\rightarrow$ Vibr	$\nu = 15.7$	$\nu = 15.0$
		$I_x = 14.8$	$I_x = 32.6$
	Rot <sub>y</sub> $\rightarrow$ Vibr	$\nu = 11.6$	$\nu = 9.49$
		$I_y = 14.8$	$I_y = 24.3$
	Rotation <sub>z</sub>	$\nu = 11.7$	$\nu = 9.43$
		$I_z = 29.5$	$I_z = 39.5$
	$\sigma = 6$	$\sigma = 1$	

Table 6.2: Molecular constants corresponding to the different types of motion of benzene. The mass ( $M$ ), moment of inertia ( $I$ ), and frequency ( $\nu$ ) values are given in  $10^{-25}$  kg,  $10^{-46}$  kg m<sup>2</sup>, and  $10^{-11}$  s<sup>-1</sup> respectively.

Benzene		PAH	TS
Gas phase	Translation	$8.73 \times 10^{10}$	$9.63 \times 10^{10}$
	Rotation	$7.53 \times 10^3$	$1.87 \times 10^5$
		$E_2$	
Adsorbed phase	Transl $\rightarrow$ Vibr	4.48	4.65
	Rot <sub>x</sub> $\rightarrow$ Vibr	5.86	7.05
	Rot <sub>y</sub> $\rightarrow$ Vibr	5.81	7.10
	Rotation <sub>z</sub>	27.6	192
	$E_2$		-3.35

Table 6.3: Molecular partition functions corresponding to the different types of motion of the benzene molecule and the energy of the transition state ( $E_2$ ) relative to the separated reactants.  $E_2$  values are given in kJ mol<sup>-1</sup>. The translational partition functions are given in  $L$  m<sup>-1</sup> units  $L$  being a length parameter of an arbitrary value.

Naphthalene		PAH	TS1	TS2
Gas phase	Translation	$M = 2.12$	$M = 2.41$	$M = 2.41$
	Rotation	$I_1 = 94.8$	$I_1 = 114$	$I_1 = 119$
		$I_2 = 67.9$	$I_2 = 84.3$	$I_2 = 98.1$
		$I_3 = 26.9$	$I_3 = 44.4$	$I_3 = 37.5$
		$\sigma = 4$	$\sigma = 1$	$\sigma = 1$
Adsorbed phase	Transl $\rightarrow$ Vibr	$M = 2.12$	$M = 2.41$	$M = 2.41$
	Rot <sub>x</sub> $\rightarrow$ Vibr	$\nu = 15.6$	$\nu = 14.1$	$\nu = 12.3$
		$I_x = 26.9$	$I_x = 49.4$	$I_x = 42.8$
	Rot <sub>y</sub> $\rightarrow$ Vibr	$\nu = 10.8$	$\nu = 8.36$	$\nu = 9.01$
		$I_y = 68.2$	$I_y = 87.5$	$I_y = 101$
	Rotation <sub>z</sub>	$\nu = 16.0$	$\nu = 14.1$	$\nu = 13.4$
		$I_z = 95.1$	$I_z = 113$	$I_z = 119$
		$\sigma = 2$	$\sigma = 1$	$\sigma = 1$

Table 6.4: Molecular constants corresponding to the different types of motion of naphthalene. The mass ( $M$ ), moment of inertia ( $I$ ), and frequency ( $\nu$ ) values are given in  $10^{-25}$  kg,  $10^{-46}$  kg m<sup>2</sup>, and  $10^{-11}$  s<sup>-1</sup> respectively.

Naphthalene		PAH	TS1	TS2
Gas phase	Translation	$1.12 \times 10^{11}$	$1.90 \times 10^{11}$	$1.19 \times 10^{11}$
	Rotation	$1.17 \times 10^5$	$7.36 \times 10^5$	$7.47 \times 10^5$
		$E_2$		-6.32
Adsorbed phase	Transl $\rightarrow$ Vibr	4.50	4.91	5.56
	Rot <sub>x</sub> $\rightarrow$ Vibr	6.24	7.93	7.40
	Rot <sub>y</sub> $\rightarrow$ Vibr	4.39	4.93	5.16
	Rotation <sub>z</sub>	149	324	333
	$E_2$		-8.21	-6.25

Table 6.5: Molecular partition functions corresponding to the different types of motion of the naphthalene molecule and the energy of the transition states ( $E_2$ ) relative to the separated reactants.  $E_2$  values are given in kJ mol<sup>-1</sup>. The translational partition functions are given in  $L$  m<sup>-1</sup> units  $L$  being a length parameter of an arbitrary value.

Anthracene		PAH	TS1	TS2	TS9
Gas phase	Translation	$M = 2.95$	$M = 3.24$	$M = 3.24$	$M = 3.24$
		$I_1 = 225$	$I_1 = 258$	$I_1 = 271$	$I_1 = 241$
	Rotation	$I_2 = 186$	$I_2 = 217$	$I_2 = 238$	$I_2 = 195$
		$I_3 = 39.1$	$I_3 = 58.0$	$I_3 = 51.3$	$I_3 = 63.2$
		$\sigma = 4$	$\sigma = 1$	$\sigma = 1$	$\sigma = 1$
Adsorbed phase	Transl $\rightarrow$ Vibr	$M = 2.95$	$M = 3.24$	$M = 3.24$	$M = 3.24$
		$\nu = 15.8$	$\nu = 15.6$	$\nu = 15.2$	$\nu = 16.3$
	Rot <sub>x</sub> $\rightarrow$ Vibr	$I_x = 39.1$	$I_x = 62.8$	$I_x = 54.2$	$I_x = 63.4$
		$\nu = 11.4$	$\nu = 8.38$	$\nu = 9.56$	$\nu = 8.31$
	Rot <sub>y</sub> $\rightarrow$ Vibr	$I_y = 186$	$I_y = 222$	$I_y = 238$	$I_y = 198$
		$\nu = 20.9$	$\nu = 16.2$	$\nu = 21.4$	$\nu = 21.5$
	Rotation <sub>z</sub>	$I_z = 225$	$I_z = 259$	$I_z = 269$	$I_z = 238$
		$\sigma = 2$	$\sigma = 1$	$\sigma = 1$	$\sigma = 1$

Table 6.6: Molecular constants corresponding to the different types of motion of anthracene. The mass ( $M$ ), moment of inertia ( $I$ ), and frequency ( $\nu$ ) values are given in  $10^{-25}$  kg,  $10^{-46}$  kg m<sup>2</sup>, and  $10^{-11}$  s<sup>-1</sup> respectively.

Anthracene		PAH	TS1	TS2	TS9
Gas phase	Translation	$1.32 \times 10^{11}$	$1.38 \times 10^{11}$	$1.38 \times 10^{11}$	$1.38 \times 10^{11}$
	Rotation	$3.61 \times 10^5$	$2.03 \times 10^6$	$2.05 \times 10^6$	$1.94 \times 10^6$
		$E_2$		-7.70	-5.76
Adsorbed phase	Transl $\rightarrow$ Vibr	4.45	4.50	4.61	4.32
	Rot <sub>x</sub> $\rightarrow$ Vibr	5.98	7.92	7.00	7.98
	Rot <sub>y</sub> $\rightarrow$ Vibr	3.50	4.36	3.43	3.42
	Rotation <sub>z</sub>	229	491	500	470
		$E_2$		-9.16	-7.92

Table 6.7: Molecular partition functions corresponding to the different types of motion of the anthracene molecule and the energy of the transition states ( $E_2$ ) relative to the separated reactants.  $E_2$  values are given in kJ mol<sup>-1</sup>. The translational partition functions are given in  $L$  m<sup>-1</sup> units  $L$  being a length parameter of an arbitrary value.

shown in Table 6.8.

		$k^{ads}/k^{gas}$
Benzene	TS	2.48
Naphthalene	TS1	1.09
	TS2	1.20
Anthracene	TS1	1.09
	TS2	1.05
	TS9	0.91

Table 6.8: Ratios of the rate constants between the gas phase and the adsorbed phase.

As we can see, the obtained ratios are close to one, except for benzene, where  $k^{ads}/k^{gas}$  is somewhat higher than unity. The error and the reliability of this method is difficult to estimate because there are many factors to be taken into account. However, we may assume that the uncertainty (coming mainly from the inaccuracy of the energy calculations) stays within the same order as, or is smaller than the result itself. In other words, the efficiency of the method is better than qualitative. We can thus conclude that the physisorption of the PAH molecules at a purely carbonaceous surface does not result in a significant change in the reaction rate of their oxidation by OH, at least within the approximations of this method.

Considering the obtained partition functions and energy differences we can establish that the primary inhibiting effect of the soot surface coming simply from the fact that one side of the PAH molecule is hidden from the attack of OH is compensated by the energy gain of the transition states due to the stabilisation by the graphene surface. This enhanced stability in the adsorbed phase results in higher preference for the oxidation reaction, which however, takes place only at one side.

## 6.5 Conclusions

In this chapter a new method and its first applications for the characterisation of the PAH oxidation on soot have been presented. The development was motivated by the lack of a theoretical method which is able to reliably characterise the reactivity of large systems, such as PAHs on soot. Indeed, the methods available in the literature that can handle this kind of large systems are poorly suited due to the insufficient representation of the dispersion interactions that cannot be neglected in the adsorption processes and oxidation reactions studied.

To calculate the interaction energies, the SE-D method was thus used because it was proved to properly describe the interactions between large aromatic systems, and therefore it can be used to study systems for which full ab initio calculations are prohibited because of their large size.

In our calculations the soot particle was modelled by a large, flat, defect-free, graphene-like surface. Our results have shown that the physisorption of the PAH molecules at the soot surface does not change dramatically the reaction rate of the oxidation of PAHs by OH as compared to that occurring in the gas phase. It should be noted that a real surface may contain chemical defects that can lead to the modification of these results to an unknown extent. It should also be noted that the rate constants in the adsorbed phase may depend on the coverage of the soot surface. Moreover, the aforementioned capture of the OH radical by the surface can also lead to different conclusions because this should decrease the efficiency of the oxidation reaction at the surface. Finally, the aggregation or possible multilayer adsorption of the PAH molecules makes also more difficult the comparison of the experimental results with those obtained from the theory.

Nevertheless, the SE-D method represents a real improvement with respect to other quantum chemical methods because it can be used for characterising very large systems with relatively low computational costs. Furthermore, it can easily be used to take into account finite coverages, and it can also be reparametrised to include surface defects. Finally, it should be mentioned that the application of this method can be extended to other carbonaceous systems, such as nanotubes and fullerenes.

## Chapter 7

# Conclusions and perspectives

In this thesis, I have presented a series of theoretical studies aiming at characterising, at a molecular level, the adsorption of various compounds on the surface of solid particles present in the Earth's atmosphere. The corresponding numerical studies were devoted to ice and soot particles which are abundant in the atmosphere and which represent a major source of uncertainties in the current climate models.

The results presented here clearly show that atmospheric science may profit by the use of theoretical methods. As a matter of fact, experimental research will never be able to produce such an insight into the investigated phenomena that simulation techniques and other theoretical methods do. Making models and predictions will always be indispensable to obtain a complete picture of the examined processes. By contrast, theoretical work is worth nothing without experiences, and it must always be carried out and interpreted in light of the knowledge based on experimental data. Doubtlessly, these two aspects fruitfully supporting and complementing each other must be combined to achieve a more fundamental understanding of the phenomena of our world.

My thesis has been based on three main subjects. The first has been devoted to the study of the adsorption of acetone, formic acid and benzaldehyde on the surface of ice. When carrying out adsorption measurements, owing to technical limitations one has to face several restrictions which result in limited accuracy and range of examination. The use of the GCMC method has not only provided adsorption isotherms in the whole pressure range but also revealed the mechanism of the adsorption processes by identifying the preferred orientations of the ad molecules and the corresponding interaction energies. Moreover, the fundamental role of hydrogen bonding between the adsorbed molecules and the ice surface has been evidenced,

as well as the increasing importance of the lateral interactions when increasing the pressure. Above a certain pressure, these lateral interactions become finally the main driving force of the adsorption which cannot be neglected in the interpretation of the experimental data. The comparison of the results of these studies with the experimental data has been excellent, which, on one hand, confirms the suitability of the used potential models to describe the systems investigated, and, on the other hand, stresses again the importance of simulation techniques in the study of hardly observable processes. Further research should be directed toward the competitive adsorption of different volatile organic compounds as they are present jointly in the atmosphere, and to the role of defects (such as ions) in the adsorption processes at the ice surface.

My second subject is concerned with the role of the characteristics of soot particles that might affect ice nucleation at their surface. For this purpose, water adsorption on various particles containing, on one hand, cavities of different shape and, on the other hand, carbon atoms of different numbers have been investigated. The results have shown that the size and the shape of pores are of special interest: The more spherical the cavity is, the more effective the adsorption can be. The presence of oxidised functional groups inside the cavity does not change the maximum number of water molecules that may be trapped in it, but it enhances the affinity of water molecules for the soot at low pressure. This results in the appearance of the adsorbates in the cavity at significantly lower pressure as compared to the bare carbonaceous particle. In the future, the adsorption of water on a non-rigid soot particle, i.e., that can be deformed during the adsorption process should be studied. Understanding the formation of soot particles at high temperatures could also be of great interest.

The last topic of this thesis is related to the reactivity of soot particles in the atmosphere. A new model has been presented to compare the oxidation reaction of PAH molecules by the OH radical in the gas phase with that taking place when the PAH molecules are adsorbed on a perfect carbonaceous surface. The soot-PAH interaction as well as the PAH-OH interaction have been described by the SE-D method, which provides an appropriate energetic characterisation of large carbonaceous systems. The detailed analysis of the reactions taking place in the different phases has revealed that the primary inhibiting effect of the soot surface (namely that it hides one side of the PAH molecule from the OH attack) is compensated by the energy gain of the transition state of the oxidation reaction. The joint quenching of these two effects results in a similar reaction rate of oxidation of PAHs by OH in the gas phase and in the adsorbed phase at a perfect carbonaceous surface. This research

might be extended to the study of structurally and chemically defected surfaces, and to the impact of varying surface coverage of PAH molecules on the reaction rate of the oxidation. It should be mentioned that the accuracy of the theoretical results obtained here (i.e., the accuracy of the parameters of the SE-D method) could only be checked by comparison with experimental results on well-defined carbonaceous systems which are unfortunately largely missing up to now. Finally, it is also worth noting that the SE-D method could be extended to reactions taking place at other carbonaceous surfaces such as graphene, fullerene, or nanotubes.

# Appendices

## Appendix A

### Biased grand canonical MC techniques

#### Cavity bias of Mezei

As it was mentioned in Section 3.1.1.1, entirely random insertion and deletion attempts in dense systems are quite inefficient thus getting such a system equilibrated in the grand canonical ensemble would almost be impossible.

To overcome this shortcoming Mezei suggested[46, 47] a modification of the insertion/deletion process which allows for insertion only at points where a cavity of suitable radius  $R^C$  exists. In this case the acceptance probabilities defined in Eq 3.19 and Eq 3.20 will be modified:  $V$  will be replaced by the volume of the subspace that is formed by the union of all points that are centres of a cavity of radius greater than or equal to  $R^C$ . Accordingly, the insertion and deletion attempts will be accepted with the respective probabilities

$$P_{acc,CB}^{ins} = \min \left\{ 1, \exp \left[ \ln \left( P_N^C \frac{V}{\Lambda^3} \right) - \ln(N+1) - \beta(\Delta U - \mu) \right] \right\}, \quad (\text{A-1})$$

and

$$P_{acc,CB}^{del} = \min \left\{ 1, \exp \left[ -\ln \left( P_{N-1}^C \frac{V}{\Lambda^3} \right) + \ln(N) - \beta(\Delta U + \mu) \right] \right\}, \quad (\text{A-2})$$

where  $P_N^C$  is the probability of finding a cavity of radius  $R^C$  or larger, provided the system consists of  $N$  particles. In the above equations  $N$  denotes the current number of particles,  $\Lambda$  is the thermal de Broglie wavelength defined in Eq 3.13,  $\beta$  is the Boltzmann factor,  $U$  is the total potential energy of the system, while  $\mu$  is the chemical potential.

The realisation of the proposed sampling thus requires the computation of  $P_N^C$  and the finding of a point that is the centre of a cavity of radius  $R^C$  or larger. By generating a number of uniformly distributed test points, and finding the fraction of them that are in a suitable cavity, one obtains both a Monte Carlo estimate for  $P_N^C$  and also a definite point where a new particle can be inserted. As the simulation proceeds, the estimate of  $P_N^C$  will necessarily improve.

There is a possibility, however, that none of the generated points are found to be inside suitable cavities. When this happens, the insertion is attempted randomly

and the acceptance is according to Eq 3.19. In order to maintain the microscopic reversibility, however, random deletion should be attempted as frequently as random insertion. The frequency of this event is  $(1 - P_N^C)^{N_t}$  where  $N_t$  is the number of test points generated. In practice, this means that when deletion is going to be done it has to be decided whether an unbiased or a biased deletion will be attempted.

The adequate values of the two parameters,  $R^C$  and  $N_t$  controlling the efficiency of the simulation can be determined by short trial runs.

### Rotational insertion bias of Cracknell and Nicholson

According to the basic concept of this methodology the biased insertion is based solely on orientation and is independent of position[171]. The method defines an insertion function  $f(\mathbf{r}, \omega)$  (analogous to  $P_N^C$  in the previous section) whose value is proportional to the probability of an insertion being made at a particular position ( $\mathbf{r}$ ) and orientation ( $\omega$ ). For an unbiased insertion attempt this function represents uniform distribution. To normalise the insertion function in a particular volume  $V$  at any possible orientations one gets

$$\int d\mathbf{r}d\omega f(\mathbf{r}, \omega) = 8\pi^2 V. \quad (\text{A-3})$$

The modified acceptance criteria can be written as

$$P_{acc, RIB}^{ins} = \min \left\{ 1, \exp \left[ \ln \left( \frac{V}{f(\mathbf{r}, \omega)\Lambda^3} \right) - \ln(N + 1) - \beta(\Delta U - \mu) \right] \right\}, \quad (\text{A-4})$$

$$P_{acc, RIB}^{del} = \min \left\{ 1, \exp \left[ -\ln \left( \frac{V}{f(\mathbf{r}, \omega)\Lambda^3} \right) + \ln(N) - \beta(\Delta U + \mu) \right] \right\}. \quad (\text{A-5})$$

It is possible to demonstrate that the procedure can be carried out according to the microscopic reversibility.

Now, one has to define the insertion function. Its definition may be arbitrary, but the Markov chain of states will still converge to the same limiting value. A judicious choice of  $f(\mathbf{r}, \omega)$  based on the geometry of the molecule will, however, greatly speed convergence. Cracknell and Nicholson[171] used the following procedure for water: The two axes were fixed to the position of the oxygen atom, the first axis was along the dipole vector of the molecule pointing outward from the oxygen ( $a$ ), whereas the second one was parallel to H-H vector ( $b$ ).

For a trial insertion, the position of the oxygen atom is chosen randomly in the simulation box. It is possible to choose the orientation of axis  $b$  randomly and then that of axis  $a$  in a biased way. The insertion function  $f(\mathbf{r}, \omega)$  may thus be written as  $f(\psi)$ , where  $\psi$  is the angle of rotation around  $b$ . The configurational energy of an insertion is then calculated at  $n$  equally spaced orientations  $\psi_p$  on a circle setting  $a$  to each of the  $n$  trial orientations in turn. To maintain microscopic reversibility, the position of the first point ( $\psi_p = 0$ ) must be chosen in a systematic, non-random fashion. At each of the  $n$  test points  $f(\psi_p)$  is proportional to the Boltzmann weighting of the configurational energy.  $f(\psi)$  must also be calculated for a trial deletion. When attempting a deletion, the configurational energies of  $n$  test orientations of  $a$  are calculated as before, and  $f(\psi)$  is normalised. Then  $f(\psi)$  is evaluated at the actual orientation of the molecule.

## Appendix B

### Long-range corrections used in computer simulations

#### LRC for the Lennard-Jones potential

As explained in Section 3.1.4, computer simulations frequently use a pair potential with a spherical cutoff at a distance  $R_{\text{cut}}$ . It becomes useful to correct the results of simulations to compensate for the missing long-range part of the potential. Contributions to the energy, pressure etc. for  $r > R_{\text{cut}}$  are frequently estimated by assuming that the pair correlation function ( $g(r)$ ) is equal to 1 in this region, and using that the ensemble averages of any pair function may be expressed with  $g(r)$  one gets

$$E_{\text{full}} = E_{\text{cut}} + E_{\text{LRC}} = E_{\text{cut}} + 2\pi N\rho \int_{R_{\text{cut}}}^{\infty} dr u_2(r) r^2, \quad (\text{B-1})$$

$$(pV)_{\text{full}} = (pV)_{\text{cut}} + (pV)_{\text{LRC}} = (pV)_{\text{cut}} - \frac{2}{3}\pi N\rho \int_{R_{\text{cut}}}^{\infty} dr w(r) r^2, \quad (\text{B-2})$$

where  $E_{\text{full}}$  and  $(pV)_{\text{full}}$  are the desired values for a liquid with the full potential, and  $E_{\text{cut}}$  and  $(pV)_{\text{cut}}$  are the values actually determined from a simulation using a potential with a cutoff. In the above equations  $r$  denotes the distance of two particles,  $\rho$  is the number density,  $u_2(r)$  is the pair potential, whereas  $w(r)$  is the pair virial function. For the Lennard-Jones potential these equations become

$$E_{LRC}^* = \frac{8}{9}\pi N\rho^* R_{\text{cut}}^{*-9} - \frac{8}{3}\pi N\rho^* R_{\text{cut}}^{*-3}, \quad (\text{B-3})$$

$$p_{LRC}^* = \frac{32}{9}\pi\rho^{*2} R_{\text{cut}}^{*-9} - \frac{16}{3}\pi\rho^{*2} R_{\text{cut}}^{*-3}, \quad (\text{B-4})$$

where the asterisk refers to Lennard-Jones reduced units ( $E^* = E/\epsilon$ ,  $p^* = p\sigma^3/\epsilon$  and  $\rho^* = \rho\sigma^3$ ,  $\epsilon$  and  $\sigma$  being the parameters of the Lennard-Jones potential). In the case of the  $(N, V, E)$  and  $(N, V, T)$  ensembles, these corrections can be applied to the results after a simulation has run. However, if the volume or the number of particles is allowed to fluctuate, it is important to apply the corrections to the calculated instantaneous energies, pressures etc. during the course of a simulation, since they will change as the density fluctuates.

## LRC for the electrostatic potential

The appropriate treatment of the electrostatic potential in molecular simulations is quite a delicate task due to the slow convergence of the potential to zero, which causes that the effect of a point charge is non-negligible even at long distances. This may cause troubles as one is always restricted to simulate finite systems, thus lacking interactions beyond the boundaries of the system may distort the results. However, there have been some possible ways trying to handle these difficulties.

### No long-range correction

Despite the inaccuracy of the complete neglect of the interaction potential beyond the cutoff radius, this method can be used in certain cases, i.e. for isolated systems (e.g. isolated soot particles in the atmosphere) or for systems being described by potential models that were developed without long-range correction (e.g. TIP5P water model).

In the very basic case, the Coulomb potential energy is cut by a straight spherical cutoff truncation at a distance  $R_{\text{cut}}$ , so the potential function reads

$$U_{SC}^C(r) = \frac{1}{2} \sum_i^{N_{at}} \sum_{j \neq i}^{N_{at}} \frac{q_i q_j}{4\pi\epsilon_0 r_{ij}} H(r_{ij}; R_{\text{cut}}), \quad (\text{B-5})$$

where  $i$  and  $j$  go over all the  $N_{at}$  atoms in the system,  $q$  denotes atomic point charges,  $\epsilon_0$  is the dielectric permittivity of vacuum,  $r_{ij}$  is the interatomic distance,

while  $H(r_{ij}; R_{\text{cut}})$  is the Heaviside step function whose value equals 1 if  $r_{ij} < R_{\text{cut}}$  and 0 otherwise. (Note that the form of the above equation assumes that the relative permittivity of the medium between the charges is equal to unity.) This coarse cutoff of the potential has two main drawbacks. First, the conservation of the total energy will not be satisfied. Second, due to the discontinuity of the potential, at the boundary of this region an artificial force emerges, which operates on an infinitesimally narrow range of distance that cannot be incorporated while simulating the dynamics of a system, thus it is often simply omitted. This causes the truncated force to correspond to a different interaction function  $U_{SC,off}^C(r)$

$$U_{SC,off}^C(r) = \frac{1}{2} \sum_i^{N_{at}} \sum_{j \neq i}^{N_{at}} \frac{q_i q_j}{4\pi\epsilon_0} \left( \frac{1}{r_{ij}} - \frac{1}{R_{\text{cut}}} \right) H(r_{ij}; R_{\text{cut}}) = U_{SC}^C(r) + U_{off}^C(r). \quad (\text{B-6})$$

If this interaction function is considered, energy conservation will be satisfied. However, this equation will only give the correct Coulomb energy of the system (the work required to assemble the charges) in the limit of a very large cutoff radius. In addition, the force does not vanish at  $R_{\text{cut}}$ , which is known to cause artefacts in simulations. An alternative is to replace the step function by a smoother switching function, which ensures not only the energy conservation but also that the force vanishes at  $R_{\text{cut}}$ . The drawback is that the interaction energy and forces are modified in the smoothing range, and atomic charges optimal for one switching scheme may be inadequate for another one.

## Reaction field correction

This methodology was first described by Onsager[172] and is widely used in other fields of physics too. In this method, it is supposed that the rest of the system beyond  $R_{\text{cut}}$  can be characterised by one relative dielectric constant  $\epsilon_{RF}$ . All charges interact with this constant dielectric medium, which manifests in the formation of an induced point dipole ('reaction field'). The correction to the total energy emerges then from the interaction between the point dipoles and the dielectric field, and between the point dipoles themselves. It can be demonstrated that the effect of the reaction field can be written as a correction to the Coulomb potential:

$$U_{RFC}^C(r) = \sum_i^{N_{at}} \sum_{j \neq i}^{N_{at}} \frac{1}{4\pi\epsilon_0} \frac{q_i q_j}{r} \left[ 1 + \frac{\epsilon_{RF} - 1}{2\epsilon_{RF} + 1} \left( \frac{r}{R_{\text{cut}}} \right)^3 \right]. \quad (\text{B-7})$$

Note that this equation is only correct if charge groups (molecules) are never cut even if some of their atoms are farther than  $R_{\text{cut}}$  from the center. The main advantages of the reaction field correction method are that it is quick and easy to program. The disadvantage is that a priori knowledge of  $\epsilon_{RF}$  is needed which is not always straightforward to determine in heterogeneous systems.

### Ewald summation technique

This technique[60] makes it possible to take into account the interaction between a charged particle and its periodic mirror images. The summation of the electrostatic potential on the infinite lattice is conditionally convergent, i.e. the result depends on the order in which we add up the terms. In this methodology, the periodic images are taken into account sequentially by increasing the distance from the central cell. As we add further terms (boxes) to the sum, we are building up our infinite system in roughly spherical layers. When adopting this approach, we must specify the nature (i.e. the relative permittivity) of the medium surrounding the sphere.

The principle of this method is that point charges are artificially screened down by a charge (usually Gaussian type) distribution of opposite sign placed on the point charges to make them short-ranged. Now the summation can be done easily in the real space. In the second step a cancelling charge distribution of the same sign as the original charge, and the same shape as the screening distribution is also added. The cancelling potential distribution is then summed in reciprocal space. In other words, the Fourier transform of the cancelling distributions (one for each original charge) are added, and the total transformed back into real space. There is, however, an important correction: the recipe includes the interaction of the cancelling distribution located in the center with itself, and this self term must be subtracted from the total. Thus, the final potential energy will contain a real space sum plus reciprocal space sum minus a self-term plus a surface term (depending on the nature of the surrounding medium). The final form in a cubic cell can be written as

$$\begin{aligned}
 U_{Ew}^C(r) = & \frac{1}{2} \sum_{i=1}^{N_{at}} \sum_{j \neq i}^{N_{at}} \left( \sum_{n_x, n_y, n_z}^{\infty} q_i q_j \frac{\text{erfc}(\kappa \|\mathbf{r}_{ij} + L \cdot (n_x, n_y, n_z)\|)}{\|\mathbf{r}_{ij} + L \cdot (n_x, n_y, n_z)\|} + \right. \\
 & \left. + \frac{1}{\pi L^3} \sum_{\mathbf{k} \neq 0}^{\infty} q_i q_j \frac{4\pi^2}{k^2} \exp\left(\frac{-k^2}{4\kappa^2}\right) \cos(\mathbf{k} \cdot \mathbf{r}_{ij}) \right) - \\
 & - \frac{\kappa}{\sqrt{\pi}} \sum_{i=1}^{N_{at}} q_i^2 + \frac{2\pi}{3L^3} \left\| \sum_{i=1}^{N_{at}} q_i \mathbf{r}_i \right\|^2, \tag{B-8}
 \end{aligned}$$

where  $\text{erfc}$  denotes the complementary error function,  $\mathbf{n} = (n_x, n_y, n_z)$  accounts for the periodic images ((0,0,0) represents the central cell) in the real space,  $\kappa$  determines the width of the Gaussian type screening charge distribution and  $L$  is the box length parameter. If  $\kappa$  is chosen to be large enough, the only term which contributes to the sum in real space is that with  $\mathbf{n} = 0$ , and so the first term reduces to the normal minimum image convention. The second term is a sum over reciprocal vectors  $\mathbf{k} = 2\pi\mathbf{n}/L^2$ . The last term applies if the surrounding medium is vacuum and vanishes if the surrounding is perfect conductor.

A very important variant of the Ewald summation technique is the particle-particle and particle-mesh (PPPM) technique that changes the way the long-range part is calculated. This modification results in much less time need as compared to the Ewald method.

## Appendix C

### Equations of state in describing phase coexistence

When performing a simulation in the grand canonical ensemble, it may be sometimes necessary to relate the chemical potential value of the simulated systems to state points on the phase diagram. In case the pressure in the system is low enough the ideal gas law can be used. At higher pressures, however, the behaviour of the studied system deviates from the ideal situation. In those cases, appropriate equations of states can yield the relation between chemical potential and pressure. The Peng-Robinson equation of state[173] proved to be very pertinent in examining the equilibrium of coexisting phases. The corresponding equations read

$$p = \frac{RT}{v-b} + \frac{a\alpha(T)}{v(v+b) + b(v-b)}, \quad (\text{C-1})$$

where  $p$  denotes the pressure,  $T$  is the temperature,  $R$  is the ideal gas constant,  $v$  is the molar volume,  $\alpha(T)$  is a temperature-dependent factor, whereas  $a$  and  $b$  are specific to the studied species:

$$a = 0.45724 \frac{R^2 T_c^2}{p_c}, \quad (\text{C-2})$$

$$b = 0.0778 \frac{RT_c}{p_c}, \quad (\text{C-3})$$

$$\alpha(T) = \left[ 1 + \left( 0.37464 + 1.54226\omega - 0.26992\omega^2 \right) \left( 1 - \sqrt{\frac{T}{T_c}} \right) \right]^2, \quad (\text{C-4})$$

where  $T_c$  and  $p_c$  are the critical temperature and pressure, respectively, whereas  $\omega$  is the acentric factor and describes the non-sphericity of molecules of the given species (e.g.  $\omega$  of noble gases equals 1). These parameters for water are  $T_c = 647.3$  K,  $p_c = 22.048$  MPa and  $\omega = 0.344$ . The above equations can be used to determine factor  $Z$  (compressibility),  $A$  and  $B$ :

$$Z = \frac{pv}{RT}, \quad A = \frac{ap}{R^2T^2}, \quad B = \frac{bV}{RT}, \quad (\text{C-5})$$

and then to obtain the fugacity coefficient in a neat phase:

$$\gamma = \exp \left[ Z - 1 - \ln(Z - B) - \frac{A}{2\sqrt{2}B} \ln \left( \frac{Z + (1 + \sqrt{2})B}{Z + (1 - \sqrt{2})B} \right) \right]. \quad (\text{C-6})$$

If multicomponent phases are studied the following mixing rules have to be applied:

$$a = \sum_i \sum_j x_i x_j a_{ij}, \quad a_{ij} = (1 - \delta_{ij}) \sqrt{a_i a_j}, \quad b = \sum_i x_i b_i, \quad (\text{C-7})$$

where  $x_i$  is the mole fraction of species  $i$ , whereas  $\delta_{ij}$  is the Kronecker delta. The fugacity coefficient of component  $k$  reads

$$\gamma = \exp \left[ \frac{b_k}{b} (Z - 1) - \ln(Z - B) - \frac{A}{2\sqrt{2}B} \left( \frac{2 \sum_i y_i a_{ik}}{a} - \frac{b_k}{b} \right) \ln \left( \frac{Z + (1 + \sqrt{2})B}{Z + (1 - \sqrt{2})B} \right) \right]. \quad (\text{C-8})$$

The relation between the fugacity and the chemical potential is established by the statistical mechanical equation:

$$\mu = k_B T \ln \left( \frac{f \Lambda^3}{k_B T} \right). \quad (\text{C-9})$$

# Bibliography

- [1] R.P. Wayne. *Chemistry of Atmospheres*. (3rd Edition, OUP, 2000)
- [2] D.J. Jacob. *Introduction to Atmospheric Chemistry*. (Princeton University Press, 1999)
- [3] G.P. Brasseur, J.J. Orlando and G.S. Tyndall. *Atmospheric Chemistry and Global Change*. (OUP, 1999)
- [4] J.H. Seinfeld and S.N. Pandis. *Atmospheric Chemistry and Physics : From Air Pollution to Climate Change*. (Wiley, 1998)
- [5] S.M. Saunders, M.E. Jenkin, R.G. Derwent, and M. J. Pilling. *Atmos. Chem. Phys.*, **3** (2003) 161.
- [6] M.E. Jenkin, S.M. Saunders, V. Wagner, and M. J. Pilling. *Atmos. Chem. Phys.*, **3** (2003) 181.
- [7] R.G. Derwent, M.E. Jenkin, and S.M. Saunders. *Atmos. Environ.*, **30** (1996) 181.
- [8] <http://mcm.leeds.ac.uk/MCM/>
- [9] R.C. Pierce and M. Katz. *Environ. Sci. Technol.*, **9** (1975) 347.
- [10] U. Pöschl, T. Letzel, C. Schauer, and R. Niessner. *J. Phys. Chem. A*, **105** (2001) 4029.
- [11] D.G. Aubin, J.P.D. Abbatt. *Environ. Sci. Technol.*, **40** (2006) 179.
- [12] R. Kotzick, U. Panne, and R. Niessner. *J. Aerosol. Sci.*, **28** (1997) 725.
- [13] C.N. Cruz and S.N. Pandis. *Atmos. Environ.*, **31** (1997) 2205.
- [14] G.T. Wolf and R.L. Klimisch, Eds. *Particulate Carbon, atmospheric life cycle*. (Plenum Press: New York, 1982.)

- [15] D.K. Lynch, K. Sassen, D.O. Starr, G. Stephens. *Cirrus*. (OUP, New York, 2002).
- [16] S. Solomon, S. Borrmann, R.R. Garcia et al. *J. Geophys. Res.*, **102** (1997) 21411.
- [17] P. Konopka and W. Vogelsberger. *J. Geophys. Res.*, **102** (1997) 16057.
- [18] U. Schumann, J. Ström, R. Busen, R. Baumann, K. Gierens, M. Krautstrunk, F.P. Schröder, J. Stingl. *J. Geophys. Res.*, **101** (1996) 6853.
- [19] V. Williams et R.B. Noland. *Transport. Res. Part D*, **10** (2005) 269.
- [20] J. Penner, D. Lister, D. Griggs, D. Dokken, and M. McFarland. *IPCC Special Report, Aviation and the global atmosphere*. (Cambridge University Press, 1999).
- [21] P. Forster, V. Ramaswamy, P. Artaxo, T. Berntsen, R. Betts, D. Fahey, J. Haywood, J. Lean, D. Lowe, G. Myhre, et al., *Fourth Assessment Report of the Intergovernmental Panel on Climate Change, Climate Change 2007 : The Physical Science Basis*. (Cambridge University Press, Cambridge, United Kingdom and New York, NY, USA., 2007).
- [22] C.S. Zerefos, K. Eleftheratos, D.S. Balis, P. Zanis, G. Tselioudis. *Atmos. Chem. Phys.*, **3** (2003) 1633.
- [23] O. Boucher. *Nature*. **397** (1999) 30.
- [24] B. Karcher. *Atmospheric Research*, **46** (1998) 293.
- [25] G. Gleitsmann and R. Zellner. *Atm. Envir.*, **32** (1998) 3079.
- [26] C. Sergides, J. Jassim, A. Chughtai, and D. Smith. *Appl. Spectr.*, **41** (1987) 482.
- [27] D. Smith, W. Welch, J. Jassim, A. Chughtai, and D. Stedman. *Appl. Spectr.*, **42** (1988) 1473.
- [28] B. Karcher, M. Hirschberg, and P. Fabian. *Journal of Geophysical Research D: Atmospheres*, **101** 15169 (1996) 15169 .
- [29] P. DeMott, Y. Chen, S. Kreidenweis, D. Rogers, and D. Sherman. *Geophys. Res. Lett.*, **26** (1999) 2429.

- [30] C. Alcalá-Jornod, H. van den Bergh, and M. Rossi. *Geophys. Res. Lett.*, **29** (2002) 1.
- [31] D. Ferry, J. Suzanne, S. Nitsche, O.B. Popovcheva, N.K. Shonija. *J. Geophys. Res.*, **107** (2002) 4734.
- [32] G. J. Young, J. J. Chessick, F. H. Healey, and A. C. Zettlemoyer. *J. Chem. Phys.*, **58** (1954) 313.
- [33] M. M. Dubinin. *Carbon*, **18** (1980) 355.
- [34] O. Popovicheva and A. Starik. *Izvestiya - Atmospheric and Ocean Physics*, **43** (2007) 125.
- [35] H. Richter and J.B. Howard. *Progress in Energy Combustion Science*, **26** (2000) 565.
- [36] I.M. Kennedy. *Progr. Energy Combust. Sci.*, **23** (1997) 95.
- [37] O. Popovicheva, A. Starik, and O. Favorskii. *Izv. Akad. Nauk, Fiz. Atmos. Okeana*, **36** (2000) 163.
- [38] R. Dhaubhadel, F. Pierce, A. Chakrabarti, C.M. Sorensen. *Phys. Rev. E*, **73** (2006) 011404.
- [39] O. Popovicheva, N. Persiantseva, B. Kuznetsov, T. Rakhmanova, N. Shonija, J. Suzanne, and D. Ferry. *J. Phys. Chem. A*, **107** (2003) 10046.
- [40] B. Demirdjian, D. Ferry, J. Suzanne, O. B. Popovicheva, N. M. Persiantseva, and N. K. Shonija. *J. Atm. Chem.*, **56** (2007) 83.
- [41] M.P. Allen, D.J. Tildesley. *Computer Simulation of Liquids*. (OUP, Oxford, 1987)
- [42] N. Metropolis, A.W. Rosenbluth, M.N. Rosenbluth, A.H. Teller, and E. Teller. *J. Chem. Phys.*, **21** (1953) 1087.
- [43] G.E. Norman, V.S. Filinov. *High Temp USSR*, **7**, 216 (1969) 216.
- [44] D. J. Adams. *Mol. Phys.*, **28** (1974) 1241.
- [45] D. J. Adams. *Mol. Phys.*, **29** (1975) 307.
- [46] M. Mezei. *Mol. Phys.*, **40** (1980) 901.
- [47] M. Mezei. *Mol. Phys.*, **61** (1987) 565. Erratum: *Mol. Phys.*, **67** (1989) 1207.

- [48] L. Verlet. Phys. Rev., **159** (1967) 98.
- [49] A.J. Stone. *The theory of intermolecular forces*. (Oxford University Press, 1997)
- [50] A. Warshel, R.M. Weiss. J. Am. Chem. Soc., **102** (1980) 6218.
- [51] D.W.M. Hofmann, L. N. Kuleshova, B. D'Aguanno. Chem. Phys. Lett., **448** (2007) 138.
- [52] van Duin, Dasgupta, Lorant, Goddard. J. Phys. Chem. A, **105** (2001) 9396.
- [53] D.W. Brenner. Phys. Rev. B, **42** (1990) 9458.
- [54] G.C. Abell. Phys. Rev. B, **31** (1985) 6184.
- [55] J. Tersoff. Phys. Rev. Lett., **56** (1986) 632.
- [56] S.J. Stuart, A.B. Tutein, J.A. Harrison. J. Chem. Phys., **112** (2000) 6472.
- [57] J.A. Barker, R.O. Watts. Mol. Phys., **26** (1973) 789.
- [58] M. Neumann. J. Chem. Phys., **82** (1985) 563.
- [59] S. Nosé and M.L. Klein. Mol. Phys., **50**, (1983) 1055.
- [60] P.P. Ewald. Ann. Phys., **21** (1921) 1087.
- [61] M.J.S. Dewar, E.G. Zoebisch, E.F. Healy and J.J.P. Stewart. J. Am. Chem. Soc., **107** (1985) 3902.
- [62] M.J.S. Dewar and W. Thiel. J. Am. Chem. Soc., **99** (1977) 4899.
- [63] J.J.P. Stewart. J. Comput. Chem., **10** (1989) 209.
- [64] F. Domine and L. Rey-Hanot. Geophys. Res. Lett., **29** (2002) 1873.
- [65] C. Guimbaud, A. Grannas, P. Shepson, J. Fuentes, H. Boudries, J. Bottenheim, F. Domine, S. Houdier, S. Perrier, T. Biesenthal and B. Splawn. Atmos. Environ., **36** (2002) 2743.
- [66] T. Bartels-Rausch, C. Guimbaud, H. W. Gäggeler and M. Ammann. Geophys. Res. Lett., **31** (2004) L16110.
- [67] P. K. Hudson, M. A. Zondlo and M.A. Tolbert. J. Phys. Chem. A, **106** (2002) 2882.

- [68] N. Peybernès, C. Marchand, S. Le Calvé and P. Mirabel. *Phys. Chem. Chem. Phys.*, **6** (2004) 1277.
- [69] P. Behr, A. Terziyski and R. Zellner. *J. Phys. Chem. A*, **110** (2006) 8098.
- [70] D.J. Donaldson and D. Anderson. *J. Phys. Chem. A*, **103** (1999) 871.
- [71] A.K. Winkler, N.S. Holmes and J.N. Crowley. *Phys. Chem. Chem. Phys.*, **4** (2002) 5270.
- [72] O. Sokolov and J.P.D. Abbatt. *J. Phys. Chem. A*, **106** (2002) 775.
- [73] P. von Hessberg, N. Pouvesle, A.K. Winkler, G. Schuster and J.N. Crowley. *Phys. Chem. Chem. Phys.*, **10** (2008) 2345.
- [74] P. Jedlovsky, G. Hantal, K. Neuróhr, S. Picaud, P.N.M. Hoang, P. von Hessberg and J.N. Crowley. *J. Phys. Chem. C*, **112** (2008) 8976.
- [75] P. Jedlovsky, L. Pártay, P.N.M. Hoang, S. Picaud, P. von Hessberg and J.N. Crowley. *J. Am. Chem. Soc.*, **128** (2006) 15300.
- [76] F. Marinelli, A. Allouche. *Chem. Phys.*, **272** (2001) 137.
- [77] A. Allouche. *J. Chem. Phys.*, **112** (2005) 234703.
- [78] S. Bahr, A. Borodin, O. Hofft, V. Kempter, A. Allouche. *J. Chem. Phys.*, **112** (2005) 234704.
- [79] S. Picaud, P.N.M. Hoang, N. Peybernès, S. Le Calvé, P. Mirabel. *J. Chem. Phys.*, **122** (2005) 194707.
- [80] S. Picaud, P.N.M. Hoang. *J. Chem. Phys.*, **112** (2000) 9898.
- [81] M. Compoint, C. Toubin, S. Picaud, P.N.M. Hoang, C. Girardet, *Chem. Phys. Lett.*, **365** (2002) 1.
- [82] B. Collignon, S. Picaud. *Chem. Phys. Lett.*, **393** (2004) 457.
- [83] N. Peybernès, S. Le Calvé, P. Mirabel, S. Picaud, P.N.M. Hoang. *J. Phys. Chem. B*, **108** (2004) 17425.
- [84] L.B. Pártay, P. Jedlovsky, P.N.M. Hoang, S. Picaud, M. Mezei. *J. Phys. Chem. C*, **111** (2007) 9407.
- [85] G. Hantal, P. Jedlovsky, P.N.M. Hoang, S. Picaud. *J. Phys. Chem. C*, **111** (2007) 14170.

- [86] L. Turi. *J. Phys. Chem.*, **100** (1996) 11285.
- [87] (a) P. Jedlovszky, L. Turi. *J. Phys. Chem. B*, **101** (1997) 5429. (b) Erratum: P. Jedlovszky, L. Turi. *J. Phys. Chem. B*, **103** (1999) 3510.
- [88] M. Mezei, *MMC: Monte Carlo program for simulation of molecular assemblies*, URL: <http://inka.mssm.edu/~mezei/mmc>.
- [89] C.D. Daub, G.N. Patey, D.B. Jack and A.K. Sallabi. *J. Chem. Phys.*, **124** (2006) 114706.
- [90] S. Brunauer, P.H. Emmett and E. Teller. *J. Am. Chem. Soc.*, **60** (1938) 309.
- [91] P. Jedlovszky, Á. Vincze and G. Horvai. *J. Chem. Phys.*, **117** (2002) 2271.
- [92] P. Jedlovszky, Á. Vincze and G. Horvai. *Phys. Chem. Chem. Phys.*, **6** (2004) 1874.
- [93] M. Ferrario, M. Haughney, I.R. McDonald and M.L. Klein. *J. Chem. Phys.*, **93** (1990) 5156.
- [94] W.L. Jorgensen, J.M. Briggs and M.L. Contreras. *J. Phys. Chem.*, **94** (1990) 1683.
- [95] P. Jedlovszky and G. Pálinkás. *Mol. Phys.*, **84** (1995) 217.
- [96] J.M. Hermida-Ramón and M.A. Ríos. *J. Phys. Chem. A*, **102**(1998) 2594.
- [97] S. Weerasinghe and P.E. Smith. *J. Chem. Phys.*, **118** (2003) 10663.
- [98] A. Perera and F. Sokolic. *J. Chem. Phys.*, **121** (2004) 11272.
- [99] A. Perera, F. Sokolic, L. Almásy, P. Westh and Y. Koga. *J. Chem. Phys.*, **123** (2005) 024503.
- [100] H.J.C. Berendsen, J.R. Grigera and T.P. Straatsma. *J. Phys. Chem.*, **91** (1987) 6269.
- [101] J.E. Schaff and J.T. Roberts. *J. Phys. Chem.*, **100** (1996) 14151.
- [102] J.E. Schaff and J.T. Roberts. *Langmuir*, **14** (1998) 1478.
- [103] P. Behr, U. Scharfenort, A. Terziyski, K. Demiral and R. Zellner. in *Combustion and Atmospheric Pollution, International Symposium on Atmospheric Pollution*, ed. G. D. Ray, S. M. Forlov and A. M. Starik, Torus Press, Moscow, 2003, pp. 575–578.

- [104] L. Pártay, P. Jedlovszky and G. Horvai, *J. Phys. Chem. B*, **109** (2005) 12014.
- [105] S. Mitlin and K. T. Leung. *Surf. Sci.*, **505** (2002) L227.
- [106] F. Marinelli and A. Allouche. *Chem. Phys.*, **272** (2001) 137.
- [107] (a) P. Jedlovszky, L. Turi. *J. Phys. Chem. A*, **101** (1997) 2662. (b) Erratum: P. Jedlovszky, L. Turi. *J. Phys. Chem. A*, **103** (1999) 3796.
- [108] M. Mahoney, W.L. Jorgensen. *J. Chem. Phys.*, **112** (2000) 8910.
- [109] P. Jedlovszky, G. Hantal, K. Neuróhr, S. Picaud, P.N.M. Hoang, P. von Hessberg, J.N. Crowley. *J. Phys. Chem. C*, **112**, (2008) 8976.
- [110] NIST Standard Reference Database Number 69, NIST Chemistry Webbook Edition, <http://webbook.nist.gov/chemistry/>. (2005).
- [111] S. Bahr, V. Kempter. *J. Phys. Chem. C* **111** (2007) 11302.
- [112] D. Wei, J.F. Truchon, S. Sirois, D. Salahub. *J. Chem. Phys.* **116** (2002) 6028.
- [113] W.L. Jorgensen, D.S. Maxwell, J.J. Tirado-Rives. *J. Am. Chem. Soc.*, **118** (1996) 11225.
- [114] S. Canneaux, J.C. Soetens, E. Henon, F. Bohr. *Chem. Phys.*, **237** (2006) 212.
- [115] M. Petitjean, G. Hantal, C. Chauvin, Ph. Mirabel, S. Le Calvé, P.N.M. Hoang, S. Picaud, P. Jedlovszky *Langmuir*, **26** (2010) 9596.
- [116] R.K. Sinnott. *Chemical Engineering Design, 4th ed. Coulson and Richardson's Chemical Engineering Series, Vol. 6*; (Elsevier Butterworth-Heinemann: Oxford, UK, 2005.)
- [117] S. Bahr, V. Kempter. *J. Chem. Phys.*, **127** (2007) 074707.
- [118] O.B. Popovicheva, M.E. Trukhin, N.M. Persiantseva, and N.K. Shonija, *Atmosph. Environ.*, **35** (2001) 1673.
- [119] E.A. Müller, L.F. Rull, L.F. Vega, and K.E. Gubbins. *J. Phys. Chem.*, **100** (1996) 1189.
- [120] E.A. Müller and K.E. Gubbins. *Carbon*, **36** (1998) 1433.
- [121] C.L. McCallum, T.J. Bandosz, S.C. McGrother, E.A. Müller, and K.E. Gubbins. *Langmuir*, **15** (1999) 533.

- [122] J.K. Brennan, T.J. Bandosz, K.T. Thomson, and K.E. Gubbins. *Colloids Surf.*, **187-188** (2001) 539.
- [123] M. Jorge, C. Schumacher, and N.A. Seaton. *Langmuir*, **18** (2002) 9296.
- [124] A. Striolo, A.A. Chialvo, K.E. Gubbins, and P.T. Cummings. *J. Chem. Phys.*, **122** (2005) 234712.
- [125] S. Hamad, J.A. Mejias, S. Lago, S. Picaud, and P.N.M. Hoang. *J. Phys. Chem. B*, **108** (2004) 5405.
- [126] B. Collignon, P.N.M. Hoang, S. Picaud, and J.C. Rayez. *Chem. Phys. Lett.*, **406** (2005) 430.
- [127] B. Collignon, P.N.M. Hoang, S. Picaud, and J.C. Rayez. *Comp. Lett.*, **1** (2005) 277.
- [128] M. Oubal, S.Picaud, M.T. Rayez, and J.C. Rayez. *Carbon*, **48** (2010) 1570.
- [129] S. Picaud, P.N.M. Hoang, S. Hamad, J.A. Mejias, and S. Lago. *J. Phys. Chem. B*, **108** (2004) 5410.
- [130] S. Picaud, B. Collignon, P.N.M. Hoang, and J.C. Rayez. *J. Phys. Chem.*, **110** (2006) 8398.
- [131] S. Picaud, B. Collignon, P.N.M. Hoang, and J.C. Rayez. *Phys. Chem. Chem. Phys.*, **10** (2008) 6998.
- [132] F. Moulin, S. Picaud, P.N.M. Hoang, L. Pártay, and P. Jedlovsky. *Mol. Simul.*, **32** (2006) 487.
- [133] F. Moulin, S. Picaud, P.N.M. Hoang, and P. Jedlovsky. *J. Chem. Phys.*, **127** (2007) 164719.
- [134] A.V. Shevade, S. Jiang, and K.E. Gubbins. *Mol. Phys.*, **97** (1999) 1139.
- [135] W.L. Jorgensen, J. Chandrasekhar, J.F. Madura, R.W. Impey, and M.L. Klein, *J. Chem. Phys.*, **79** (1983) 926.
- [136] N.N. Medvedev, *in Voronoi's Impact on Modern Science, Vol. 1-2*, edited by P. Engel and H. Syta (Institute of Mathematics, Kiev, 1998), pp. 164-175.
- [137] H. Edelsbrunner, M.A. Facello, and J.Liang. *Discrete Appl. Math.*, **88** (1998) 83.

- [138] M.G. Alinchenko, A.V. Anikeenko, N.N. Medvedev, V.P. Voloshin, M. Mezei, and P. Jedlovsky. *J. Phys. Chem. B*, **108** (2004) 19056.
- [139] M.G. Alinchenko, V.P. Voloshin, N.N. Medvedev, M. Mezei, L. Pártay, and P. Jedlovsky. *J. Phys. Chem. B*, **109** (2005) 16490.
- [140] G. Malavasi, M.C. Menziani, A. Pedone, and U. Segre. *J. Non-Cryst. Solids*, **352** (2006) 285.
- [141] G.F. Voronoi. *J. Reine Angew. Math.*, **134** (1908) 198.
- [142] B.N. Delaunay. *Proc. Math. Congress in Toronto Aug.11-16 1924*, 695 (1928).
- [143] A. Okabe, B. Boots, K. Sugihara, and S.N. Chiu. *Spatial Tessellations: Concepts, and Applications of Voronoi Diagrams* (Wiley, Chichester, 2000).
- [144] N.N. Medvedev, *The Voronoi-Delaunay Method in the Structural Investigation of Non-crystalline Systems* (SB RAS: Novosibirsk, 2000), in Russian.
- [145] See, for example, a geometric library at <http://www.cgal.org/>.
- [146] N.N. Medvedev, V.P. Voloshin, V.A. Luchnikov and M.L.Gavrilova. *J. Comp. Chem.*, **27** (2006) 1676.
- [147] J. Dachs and S.J. Eisenreich. *Environ. Sci. Technol.*, **34** (2000) 3690.
- [148] R.L. Vander Wal, A.J. Tomasek. *Combustion and Flame*, **136** (2004) 129.
- [149] J.M.E Storey and J.F. Pankow. *Atmos. Environ. A*, **26** (1992) 435.
- [150] K.U. Goss and S.J. Eisenreich. *Atmos. Environ.*, **31** (1997) 2827.
- [151] B.T. Mader and J.F. Pankow. *Environ. Sci. Technol.*, **36** (2002) 5218.
- [152] B. Ngabé and L. Poissant. *Environ. Sci. Technol.*, **37** (2003) 2094.
- [153] W. Esteve, H. Budzinski, and E. Villenave. *Atmos. Environ.*, **38** (2004) 6063.
- [154] N.K. Lee, S. Park, and S.L. Kim. *J. Chem. Phys.*, **116** (2002) 7902.
- [155] M.O. Sinnokrot, E.F. Valeev, and C.D. Sherrill. *J. Am. Chem. Soc.*, **124** (2002) 10887.
- [156] C. Gonzales, T.C. Allison, and E.C. Lim. *J. Phys. Chem. A*, **105** (2001) 10583.
- [157] C. Gonzales and E.C. Lim. *J. Phys. Chem. A*, **107** (2003) 10105.

- [158] J. Hepburn, G. Scoles, and R. Penco. *Chem. Phys. Lett.*, **36** (1975) 451.
- [159] B. Collignon, P.N.M. Hoang, S. Picaud, D. Liotard, M.T. Rayez, and J.C. Rayez. *J. Mol. Struct. Theochem*, **772** (2006) 1.
- [160] B. Collignon, PhD Thesis, Besançon, France (2006).
- [161] G.C. Maitland, M. Rigby, E.R. Smith, W.A. Wakeham. *Intermolecular forces, their origin and determination*. (Oxford Science Publications, Oxford, 1987)
- [162] S. Picaud, P.N.M. Hoang, S. Hamad, J.A. Mejias, and S. Lago. *J. Phys. Chem. B*, **108** (2004) 5410.
- [163] S. Raoult, PhD Thesis, Université Bordeaux 1, France (2003).
- [164] M.I. Bernal-Uruchurtu, M.T.C. Martins-Costa, C. Millot, and M.F. Ruiz-López. *J. Comp. Chem.*, **21** (2000) 572.
- [165] M.I. Bernal-Uruchurtu and M.F. Ruiz-López. *Chem. Phys. Lett.*, **330** (2000) 118.
- [166] W. Harb, M.I. Bernal-Uruchurtu, and M.F. Ruiz-López. *Theor. Chem. Acc.*, **112** (2004) 204.
- [167] J.P. McNamara and I.H. Hillier. *Phys. Chem. Chem. Phys.* **9** (2007) 2362.
- [168] Personal communication with M. Oubal.
- [169] R. Atkinson and R.J. Cvetanović. *J. Chem. Phys.*, **56** (1972) 432.
- [170] AMPAC 8, © 1992-2004 Semichem, Inc. PO Box 1649, Shawnee, KS 66222.
- [171] R.F. Cracknell, D. Nicholson, N.G. Parsonage, H. Evans. *Mol. Phys.*, **71** (1990) 931.
- [172] L. Onsager. *J. Am. Chem. Soc.*, **58** (1936) 1486.
- [173] D.-Y. Peng, D.B. Robinson. *Ind. Eng. Chem. Fundam.*, **15** (1976) 59.



# Summary

of the thesis prepared

by György Hantal

with the co-direction of **Dr Sylvain Picaud** (Louis Pasteur Doctoral School,  
University of Franche-Comté, Besançon, France)  
and **Dr Pál Jedlovszky** (Chemical Doctoral School, Eötvös Loránd University,  
Budapest, Hungary)

## Modelling of adsorption on atmospheric solid particles

During the last decades growing attention has been paid to the atmospheric solid particles. The most abundant atmospheric solid particles are ice and soot. Their influence on the atmosphere might certainly be very complex: On one hand, these particles may modify the composition of the gas phase by adsorbing various species; on the other hand, they might induce heterogeneous reactions different from those taking place in the gas phase. Since atmospheric processes are difficult to observe, theoretical methods may contribute to better understanding and characterising these processes.

My Ph.D. research has three main subjects. The first one concerns the adsorption of volatile organic compounds, which has been studied by the Grand Canonical Monte Carlo method. This simulation technique allows us to obtain directly the adsorption isotherm of different compounds by varying their chemical potential. I have used this method to simulate the adsorption of acetone, formic acid and benzaldehyde on the surface of ice. The results agree excellently with the measured data, which shows clearly the relevance of the used theoretical method. Moreover, the molecular details have also been determined such as the interaction energy distributions of the adsorbates as well as their preferred positions and orientations at the surface. The obtained results allow us also to interpret the different adsorption

mechanisms.

My second research topic deals with the adsorption of water on soot. The soot particles have been modelled by fullerene molecules of different size packed into each other containing also holes modelling thus surface defects. The structure of the soot particles has been optimised by the reactive AIREBO potential. Further, I have determined the adsorption isotherm of water on these particles by the GCMC method. My results show that morphological properties (the shape and the size) of the cavity inside the soot particle have an important role in the adsorption processes: The more the cavity is spherical the more the adsorption is effective. The presence of oxidised functional groups inside the cavity does not change the maximum number of water molecules that could be trapped in the cavity, but it enhances the affinity of water molecules for the soot. This results in the appearance of the adsorbates in the cavity at lower pressure.

The third topic is dedicated to the reactivity of soot particles in the atmosphere. The influence of soot particles on the oxidation reaction of polycyclic aromatic hydrocarbons (PAHs) by the OH radical has been studied by comparing it to the oxidation taking place in the gas phase. To study systems containing a lot of carbon atoms such as soot and PAHs, a novel (kinetic and statistical) model has been developed and applied to the oxidation of benzene, naphthalene and anthracene. Interaction energies have been calculated by the SE-D method, which allows for a reasonably precise and computationally non-intensive description of the soot-PAH and PAH-OH interaction. The results show that on a perfect carbonaceous surface, the reactivity of the PAHs against the OH radical does not change significantly in the adsorbed phase as compared to the gas phase.

# Résumé

de la thèse préparée dans le cadre des études de thèse en co-tutelle sous la direction de

**Dr Sylvain Picaud** (École doctorale Louis Pasteur, Université de Franche-Comté, Besançon, France) et

**Dr Pál Jedlovszky** (École doctorale de chimie, Université Eötvös Loránd, Budapest, Hongrie) :

## Modélisation de l'adsorption sur des particules solides dans l'atmosphère

par György Hantal

Depuis une dizaine d'années, une attention croissante a été prêté à l'influence des particules solides dans l'atmosphère. Les particules solides les plus abondantes dans l'atmosphère sont celles de glace et de suie. Leurs impacts sur l'atmosphère sont très probablement assez complexes : D'une part, ces particules peuvent modifier la composition de la phase gaz par l'adsorption de différentes espèces ; et d'autre part, elle peuvent également induire une réactivité hétérogène différente de la réactivité observée en phase gaz. Étant donné que les processus atmosphériques sont très difficilement observables, les méthodes théoriques peuvent servir à mieux les caractériser.

La recherche effectuée dans le cadre de ma thèse s'est concentrée autour de trois sujets principaux. Le premier concerne l'adsorption des composants organiques volatiles sur la glace qui a été modélisée par la méthode Monte Carlo Grand Canonique (GCMC). Cette méthode de simulation permet d'obtenir directement l'isotherme d'adsorption d'espèces gazeuses sur la glace en variant leur potentiel chimique. J'ai utilisé cette méthode pour simuler l'adsorption de l'acétone, l'acide formique et le benzaldéhyde sur la surface de glace. L'excellent accord obtenu entre nos résultats et ceux des expériences montre toute la pertinence de l'approche théorique utilisée. De plus, les détails moléculaires de l'adsorption de ces trois composants ont

été déterminés tels que les distributions d'énergie d'interaction des adsorbats ainsi que leurs positions et orientations préférentielles sur la surface de glace. Les résultats nous permettent donc d'interpréter complètement les différents mécanismes des processus d'adsorption sur la glace.

La deuxième partie de mon travail est l'étude de l'adsorption de l'eau sur les particules de suie. Les particules de suie ont été modélisées par les molécules de fullerène empilées les unes sur les autres et contenant des trous modélisant les défauts de la surface. La structure de ces particules de suie a été optimisée en condition réactive par le potentiel AIREBO. Puis, j'ai déterminé les isothermes d'adsorption de l'eau sur ces particules par la méthode GCMC. Mes résultats montrent que les propriétés morphologiques (la taille et la forme) de la cavité présente dans des particules jouent un rôle important dans les processus d'adsorption : Plus la cavité est sphérique plus l'adsorption est efficace. La présence des groupements chimiques oxygénés dans la cavité ne change pas la quantité totale des molécules d'eau qui peuvent être piégées dans les cavités, mais elle peut induire une affinité plus élevée des molécules d'eau pour la suie à très basse pression.

Le troisième sujet est dédié à la réactivité des particules de suie dans l'atmosphère. Leur influence sur la réaction d'oxydation des hydrocarbures aromatiques polycycliques (HAPs) par le radical OH a été étudiée en la comparant avec l'oxydation ayant lieu en phase gaz. Pour étudier des systèmes contenant un grand nombre d'atomes de carbone comme la suie et les HAP un nouveau modèle (cinétique et statistique) a été développée et appliquée pour l'oxydation du benzène, naphthalène et anthracène. Les énergies d'interaction ont été calculées par la méthode SE-D qui permet une description non-couteuse et raisonnablement précise des interactions suie-HAP et HAP-OH. Les résultats montrent que sur une surface parfaite carbonée la réactivité des HAP vis-à-vis du radical OH ne change pas significativement en phase adsorbée par rapport à la phase gaz.

# Összefoglalás

Hantal György

## Légköri szilárd szemcsék felületén lejátszódó adszorpció modellezése

című doktori dolgozatához,

mely magyar részről **Dr Jedlovszky Pál** (Kémiai Doktori Iskola,  
Eötvös Loránd Tudományegyetem, Budapest),  
míg francia részről **Dr Sylvain Picaud** (Louis Pasteur Doktori Iskola,  
Franche-Comté Egyetem, Besançon) közös irányításával készült.

Az elmúlt években fokozódó figyelem irányult a légkörben található szilárd szemcsékre, azon belül is a két legnagyobb mennyiségben előforduló jég- és koromszemcsékre. Hatásuk a légkör kémiájára felételezhetően meglehetősen összetett. Egyrészt módosíthatják a légkör összetételét különböző gázok adszorpciója révén, másrészt szerepük lehet a gázfázisútól eltérő, heterogén folyamatok kiváltásában. Légkörkémiailag folyamatok megfigyelése azonban meglehetősen nehezen kivitelezhető, ugyanakkor elméleti módszerek alkalmazásával mégis lehetőség nyílt tanulmányozásukra.

A doktori tanulmányaim során végzett kutatás három fő témára osztható. Az első kutatási terület illékony szerves molekulák jégfelületen történő adszorpcióját foglalja magában, amit nagykanonikus Monte Carlo módszerrel végeztem. E szimulációs módszer az adszorpció izoterma közvetlen meghatározását teszi lehetővé a jég felületén a vizsgált anyag kémiai potenciáljának szisztematikus változtatása révén. Ezt a módszert használtam az acetone, a hangyasav és benzaldehid jégfelületű adszorpciójának tanulmányozására. A kísérleti és szimulációs eredmények kitűnő egyezése alátámasztja az alkalmazott módszer relevanciáját. Ezen felül a három

vizsgált molekula adszorpciójának molekuláris részleteit is felderítettük, úgy mint az adszorbeált molekulák kölcsönhatási energiájának eloszlását valamint leggyakoribb felületi orientációit. A kapott eredmények fényében értelmezhetjük a különböző jégfelületi adszorpciók folyamatok mechanizmusát.

Második kutatási témát a vízmolekulák koromszemcse felületén történő adszorpciójának vizsgálata képezte. A koromszemcséket egymásba helyezett koncentrikus fullerén molekulák együtteseként modelleztük. A különböző rétegekben lyukakat hoztunk létre, majd az így kapott szerkezeteket a reaktív AIREBO potenciál segítségével optimáltuk. Ezután a víz adszorpciók izotermáját határoztam meg a szemcsék felületén nagykanonikus Monte Carlo módszerrel. Eredményeim azt mutatták, hogy az adszorpciók folyamatokban fontos szerepet játszanak a szemcse belsejében található üreg morfológiai tulajdonságai (alakja és mérete): minél inkább gömbszerű az üreg, az adszorpció annál hatékonyabbnak bizonyul. Az üregben belüli oxigéntartalmú funkcionális csoportok jelenléte nem befolyásolja az üreget kitöltő vízmolekulák maximális mennyiségét, de fokozza affinitásukat kis nyomáson a koromszemcse iránt.

A harmadik kutatási területet a koromszemcsék légköri reaktivitásának tanulmányozására fókuszáltuk. A koromnak a policiklusos aromás szénhidrogének (PAH molekulák) hidroxil gyök által történő oxidációs reakciójára gyakorolt hatását vizsgáltuk a gázfázisú reakcióval való összehasonlítás keretében. Az ilyen, nagy mennyiségű szénatomot tartalmazó rendszerek, mint a korom és a PAH molekulák tanulmányozásához egy új, kinetikai-statisztikus modellt fejlesztettünk ki, és alkalmaztuk a benzol, a naftalin és az antracén oxidációjának vizsgálatára. A kölcsönhatási energiák számítására az SE-D módszert használtuk, ami a korom és a PAH molekula valamint a PAH molekula és az OH gyök közötti kölcsönhatás – számítási igényét tekintve nem drága, ugyanakkor mégis elfogadható pontosságú – leírását teszi lehetővé. Az eredmények azt mutatták, hogy a PAH molekulák OH gyökkel szembeni reaktivitása a gázfázishoz képest nem változik számottevően egy hibátlan, szénatomokból álló felületen történő adszorpció hatására.